APPENDIX 1

EXPERIMENTAL EVALUATION OF RELATIVE DEFECT CRITICALITY

1 INTRODUCTION

Application of fiber-reinforced composites to strengthen and repair deficient civil structures relies on a comprehensive understanding of the strengthening mechanism. When the CFRP composite material is bonded to surfaces of structural concrete components, the adhesive material must provide sufficient strength and stiffness to transfer stresses between the concrete and composite reinforcement such that the strengthening scheme remains effective throughout its design lifetime.
Defects, situated at the concrete/composite interface or within the composite material are potential initiators for disbonding of the composite from the underlying concrete substrate, eventually causing peel-off of the composite overlay [1].
In this study, an approach based on fracture mechanics is developed to evaluate disbond fracture energy of adhesion between concrete and CFRP overlays, investigating a previously selected number of artificially induced material defects [2]. The present report establishes defect criticality based on relative reduction of fracture toughness, measured during peel-off between CFRP overlays and concrete. As such, field inspectors are given an effective method to assess criticality of defects found in the field, including those detected through non-destructive testing [3]. Ultimately, given the specific size and location of defects within the concrete/composite hybrid system, a ranking scheme is established.

Although a wide range of test methods exists, the mechanisms utilized by each individual method are distinctively different. Hence, to utilize a method suitable for assessing the effect of defects on adhesive properties between CFRP and concrete, mechanisms employed by such systems must first be discussed. Accordingly, general background information on mechanics of the strengthening methods is provided, considering some of the most common rehabilitation schemes used today.

Given the possible variations in service life, dimension, frequency and level of traffic, and thus deficiency of concrete structures, each rehabilitation scheme must be viewed differently, i.e. the locations and amounts of CFRP used for each project vary distinctively. In addition, due to the relatively short history of structural rehabilitation using FRP composites, no comprehensive standardization code has yet been agreed on. Hence, while the load-carrying capacity may vary widely among different rehabilitation designs, the current report establishes a methodology for quantifying defect criticality on a relative basis. As such, a presumably defect-free scheme will serve as a baseline for maximum achievable bond strength.

To provide the reader with the general methodology followed in the current report, extensive theoretical background addressing the mathematical model as well as the test setup utilized in the present study is given. While the experimental approach in this study was derived from findings of earlier investigations, several modifications were introduced. Also, prior to conducting the actual study, a preliminary validation program was conducted. As such, the proposed mathematical model was confirmed from experiments using materials largely identical to those applied in the actual tests.

Finally, a criticality matrix, depicting relative criticality of defects based on the results obtained from this study, will be given. Results from this investigation will serve to identify a selected number of defects that will be subject to further study.

2 STRENGTHENING MECHANISMS IN CFRP REHABILITATION

In general terms, concrete can be referred to as a material with excellent structural properties, presupposing it is solely subjected to compressive loading conditions. Given its significantly lower tensile strength, steel reinforcement is required to account for any tensile stresses eventually developing during loading in shear, flexure and particularly pure tension of structural concrete elements. Due to the degradation of constituent materials over service time, mainly due to overloading, environmental attack, earthquakes or accidental damage along with a continuously increasing traffic demand, structural insufficiency tends to develop. Ultimately, due to a significant loss in performance, structural rehabilitation measures utilizing CFRP materials are used to retain full or partial capacity of the structure.

As may be expected, the design approach for obtaining an efficient CFRP rehabilitation scheme is similar to methodologies used in designing reinforced concrete members. As such, tensile stresses are supposed to be accounted for by the externally placed CFRP material. However, bond mechanisms between concrete and CFRP are significantly different from those employed in conventional reinforced concrete members. As such, the single most critical aspect in strengthening of concrete structures through externally bonded materials is the bond between substrate and reinforcing material [4].
In this context, a number of general design implications have been derived from previous research investigations [4]. Firstly, surface preparation of the concrete significantly influences the ultimate bond strength. Hence, to achieve the best possible bond, the concrete surface should be mechanically abraded or sandblasted. In addition, application of a primer is advisable as to quench absorption of resin from the subsequently wet-placed composite. Secondly, most off-the-shelf resin systems can be effectively used to bond composite materials to concrete, provided they display excellent workability and are compatible with the fiber type of the individual project. It has further been shown that use of ductile resins leads to a less effective bond. Thirdly, concrete strength plays an integral part in determining the ultimate bond strength of the concrete/composite system. It can be assumed that if the failure mode of the joint is governed by shearing of the concrete directly beneath the bond, ultimate bond strength will be proportional to $\sqrt{f_c'}$. This indicates the dependence of bond strength on mechanical properties of the concrete substrate. Furthermore, it has been shown that there exists a bond development length for a joint beyond which no further increase in failure load can be achieved. Finally, experiments have shown that failure occurs almost exclusively through loss of bond between the concrete and composite, indicating that, while the joint is fully developed, the capacity of the composite material is almost never fully utilized.

To date, proper design of CFRP rehabilitation schemes remains subject to research and has not yet been fully investigated. Consequently, installation methodologies vary, and do not adhere to a single comprehensive design principle. Nonetheless, a variety of general design implications have been identified and are introduced in the following [5]. They will serve in providing an overview of strengthening mechanisms on which most of the subsequent discussion is based. In current design, three predominant strengthening methods are addressed, namely strengthening for bending, shear, and to some extent,

torsion. In the following, elementary mechanical behavior of these design codes will be given.

For FRP strengthening in bending, the material is applied to the tension side of the structure to account for any deficiency of the internal steel reinforcement. While such deficiency may originate from a variety of factors, it is mostly conditioned by corrosion and yielding due to steadily increasing traffic loads. Considering the beam shown in Figure 2-1, it may be seen that a variety of different flexural failure modes exist. As shown, tensile failure of the CFRP overlay may be expected only near the center of the beam, as the shear forces at the center are zero, while the tensile force in the composite reaches its maximum value. As CFRP materials typically fail in a brittle manner, this mode is highly unfavorable. However, due to the significant differences between ultimate strain of CFRP and yield strain of steel reinforcement, failure in location 2 is generally preceded by considerable deformation of the structure [5].

When moving the assumed failure location towards either end of the beam, shear stresses begin to develop at the concrete/composite bondline region. Near the end region, shear stresses are highest and accompanied by peeling stresses that may eventually result in peeling fracture and delamination. Favored by the inclination of concrete shear cracking in these locations, end peeling of CFRP laminates has often been observed in laboratory experiments [6], [7]. For these reasons, recent studies have focused on investigating efficacy of different anchoring mechanisms to reduce the likeliness of plate-end delamination [8]. Nonetheless, while end anchorage can effectively increase the flexural capacity of a structure while minimizing the likeliness of peel failure, a second rationale of CFRP strengthening, namely restriction of crack opening, must be considered. Herein, efficacy of bond strength between the middle and outer sections of the beam are most critical as flexural cracks typically develop at these locations. Hence, to minimize crack opening, a continuous bond throughout the entire bonded distance must be ensured.

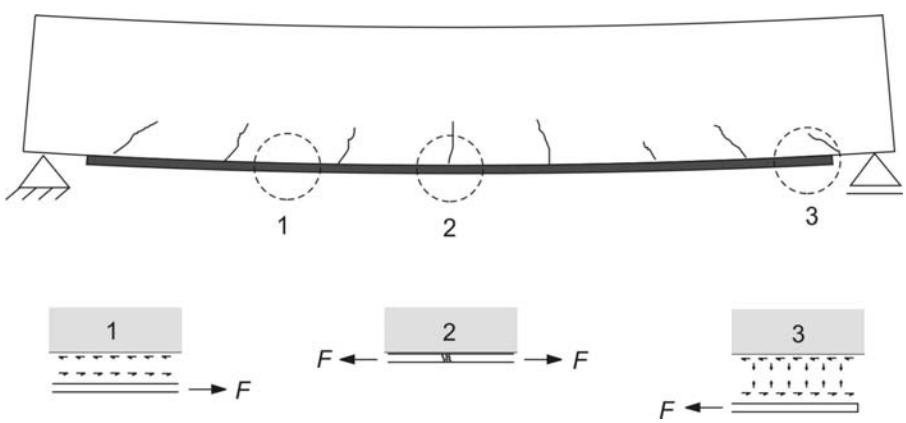

Figure 2-1: Failure Modes in Flexural Rehabilitation of Beams

Although calculation of shear- and normal stresses for structures loaded in bending is relatively complicated, FE analyses have shown that variation in stresses along a strengthened beam subjected to a single, symmetrical point load, are as depicted in Figure 2-2 [5]. It may be seen that shear stress is highest at the plate ends, indicating a natural

tendency of such systems towards peel failure at the termination points. Similarly, peel stress is highest at the ends but experiences a change in sign not far from the end, indicating that the composite laminate is actually pressed against the host material, thus substantially reducing the likeliness of disbonding in these regions. At locations other than the extreme ends, peeling stresses rapidly reduce to a level at which they may be considered negligible.

Given the fact that stress transfer in regions 1 and 3 of Figure 2-1 is mainly provided by the shear transfer capabilities of the resin system, thickness of the bondline region becomes a critical factor. As such, it has been shown analytically that for flexurally loaded systems, bondline thickness should be kept as thin as possible [9].

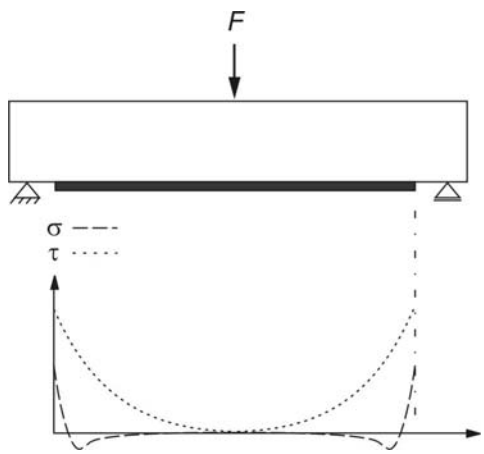

Figure 2-2: Shear- and Peel Stresses from FE Analysis of Point-loaded Beams

For shear rehabilitation, the strengthening material can be applied in the form of sheets over the entire beam or as strips, covering only distinct locations at which shear cracking may be expected. In addition, orientation of the CFRP reinforcement may be vertical or inclined, depending on the individual cracking found in the structure (Figure 2-3). Similar to flexural rehabilitation, the material is applied such that shear forces at the concrete/composite interface are the main contributors to stress transfer. Given the generally shorter lengths of composite material needed for shear rehabilitation, sufficient development length becomes a further concern. Here, end anchorages have proven particularly useful [8].

In the state of California, current FRP rehabilitation efforts typically entail use of two different strengthening systems. The first system is applied by in-situ infiltration of dry carbon fabric using a compatible epoxy system, which serves both infiltration and adhesion of the reinforcing material. The second system utilizes prefabricated carbon epoxy strips of typically 3-in (76.2-mm) width that are bonded to deficient pats of the structure using high-viscosity gel bonders. Thickness of these systems normally ranges between 0.04 and 0.05-in (1.20 mm and 1.27-mm).

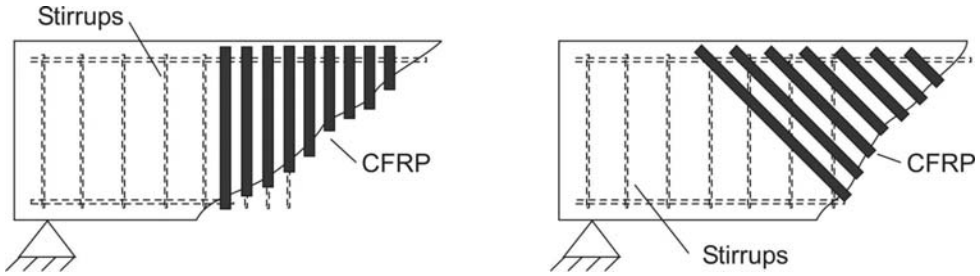

Figure 2-3: Shear Strengthening of Reinforced Concrete Beams

3 FRACTURE TESTING AND FAILURE ANALYSIS

3.1 INTRODUCTION

When composite reinforcement is bonded to the tensile surfaces of concrete members, the adhesive material must provide sufficient toughness to dissipate energy from cracking and sufficient strength and stiffness to transfer stresses between the two adherents. Given the relatively short history of application, bond transfer mechanisms between CFRP and concrete have been studied extensively during the past several years [10], [11], [12], [13]. Herein, primary focus has been on investigating the effects of choice of materials, surface preparation and environmental exposure on fracture toughness, using a wide variety of test arrangements.

Peeling of the polymer composite sheet is usually produced by the relative vertical displacement across shear- and/or flexural cracks in the concrete, as well as a potentially high level of stress concentration existing at the end of the bonded plates [12]. Because the bondline of adhesively bonded joints may contain stress concentrations, manufacturing flaws, and defects, fracture mechanics is commonly applied to the failure analysis of adhesively bonded joints. At joints, cracks can develop in the adhesive or substrate material (cohesive failure) or along the interface between the adhesive and an adherent (adhesive failure) [14]. Further, a crack at an interface can experience three different loading types, namely opening of the crack in tension, sliding by means of in-plane shear, and sliding by means of out-of-plane shear. Differences among the various loading types as well as stress cases imparting each loading type are discussed in the following.

To aid in uniquely discriminating between the three mentioned loading types, they are commonly referred to as separate modes. As such, a tensile (or tearing) stress applied to the crack tip is referred to as mode I, as depicted in Figure 3-1. In this mode, the adherent is subjected to pure tensile loading without presence of shear stress in the material. The most common test method to evaluate the mode I fracture toughness and interfacial fracture energy is by means of the double cantilever beam (DCB) specimen, shown in Figure 3-2. When the load is applied perpendicular to the crack plane, the DCB can be used for mode I fracture toughness, provided that the adherents are made of the same material and have identical thickness [14]. A pre-crack is typically utilized to control the crack the initial development of the crack path. Apart from a straightforward analytical approach, DCB specimens are relatively simple to manufacture and test. Furthermore, crack propagation normally occurs in a stable fashion, meaning that the crack grows without “jumping” over large distances. Aspects of stability will be further discussed in Section 3.3.

In situations where cracks propagate in-plane and perpendicular to the crack plane, it is referred to as mode II (compare Figure 3-1). Common specimen configurations include the DCB specimen with adherents of different bending stiffnesses and end-notched flexure (ENF) specimens, in which a three-point bending load is applied instead of an end load.

If instead the load is applied parallel to the crack plane, mode III cracking can be obtained. For testing purposes, the DCB specimen is rotated 90° such that the adhesive is

subjected to pure out-of-plane torsion. It should be noted that in reference to Chapter 2, disbonding due to peeling is best represented by mode I while shearing at the concrete/composite interface near the center regions of the beam may be assumed similar to a mode II failure.

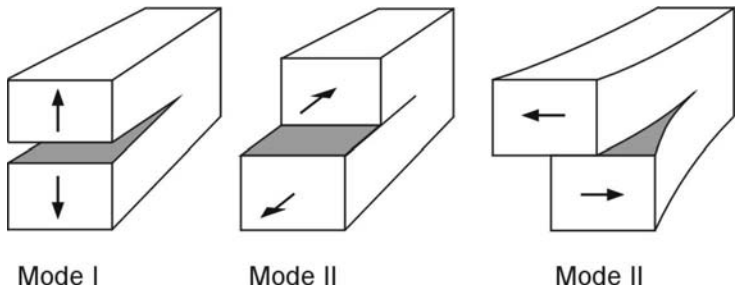

Figure 3-1: Three Modes of Possible Crack Loading

To develop a test suitable for evaluating the toughness, i.e. durability, of the concrete/composite interface, the type of loading that this interface is likely to undergo during in-service operation must be considered. From a strength viewpoint, the most important loading modes are typically those of modes I and II since traffic and certain environmental loads (wind, etc.) impart both modes at the interface. In contrast, processes such as exposure to freeze-thaw cycling or impact loading mainly challenge durability of the system, representing a mode I loading condition [15].

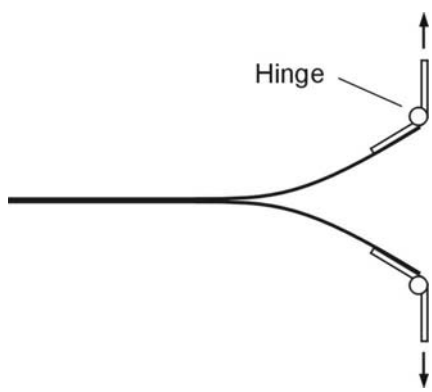

Figure 3-2: DCB Specimen for Mode I Testing

3.2 Fracture Energy Release Rate

The Griffith energy balance for an incremental increase in crack area, *dA*, under equilibrium conditions can be expressed in the following way [5]:

$$\frac{dE}{dA} = \frac{d\Pi}{dA} + \frac{dW_s}{dA} = 0 \tag{3.1}$$

or

$$-\frac{d\Pi}{dA} = \frac{dW_s}{dA} \tag{3.2}$$

where E is the total energy, Π is the potential energy supplied by the internal strain energy and external forces, and W_s is the work required to create new surfaces. Later, Irwin [16] proposed an energy approach to define the energy release rate, G. It is essentially equivalent to the Griffith model though in a form that is more convenient for solving engineering problems. Defined as the measure of energy available for an increment of crack extension, energy release rate is given as:

$$G = -\frac{d\Pi}{dA} \tag{3.3}$$

where the negative sign signifies the fact that strain energy is being released. For a planar component of constant width B, Equation (3.1) can be rewritten as

$$G = -\frac{d\Pi}{B \cdot da} \tag{3.4}$$

Herein, the potential energy of an elastic body, Π , is defined as follows:

$$\Pi = U_s - P \tag{3.5}$$

where U_s is the strain energy stored in the body and P is the work done by external forces. Since G is obtained from the derivative of a potential, it is also called *the crack extension force* or the *crack driving force* [5]. The simple expression given by Equation (3.4) provides the basis for several data reduction methods, as discussed in subsequent parts of Section 3.5.

3.3 R-CURVE AND INSTABILITY

As defined by Equation (3.4), crack growth may be characterized in terms of the energy per unit area necessary to create new surface area. Herein, the crack resistance, R, governs the energy necessary to create new surface area. Hence, at fracture:

$$G = R\,. \tag{3.6}$$

Although R is material dependent, it does not necessarily have to be constant. Instead, the shape of a plot of G versus crack extension, commonly referred to as *R-curve*, depends on material behavior and, to a lesser extent, on the configuration of the cracked structure [5].

Upon crack extension, crack growth may be stable or unstable, depending on how energy release rate and resistance to crack extension vary with crack size. Thus, crack growth is stable provided that:

$$\frac{dG}{dA} \le \frac{dR}{dA} \tag{3.7}$$

Similarly, unstable crack growth occurs when

$$\frac{dG}{dA} \geq \frac{dR}{dA} \tag{3.8}$$

In this context, it is important to differentiate between the two possible forms of load introduction, namely *load control* and *displacement control*. According to Equations (3.7) and (3.8), stability of crack growth depends on the rate of change in *G*, representing the second derivative of potential energy. Although the driving force, *G*, is identical for both loading cases, the rate of change of the driving force curve depends on how the structure is loaded [5].

Since successful fracture testing demands crack growth to occur in a stable manner, it is preferable to employ a test configuration in which the driving force decreases with crack growth. While this can be obtained in certain test configurations employing displacement control, load control typically results in an increasing driving force. Consequently, displacement control tends to be more stable than load control.

A graphical illustration of stable and unstable behavior during fracture testing is depicted in Figure 3-3. As may be noted, the *R*-curve of this test is assumed to continuously increase with crack length, indicating a behavior representative of ductile materials, such as metals, where a plastic zone at the tip of the crack increases in size as the crack grows. If the structure is load controlled, a load equal to P_3 represents a point of instability, as the driving force curve is tangent to the *R*-curve. Instead, displacement control yields stable behavior since the driving force decreases with crack growth. Thus, to cause further crack growth, displacement must be increased.

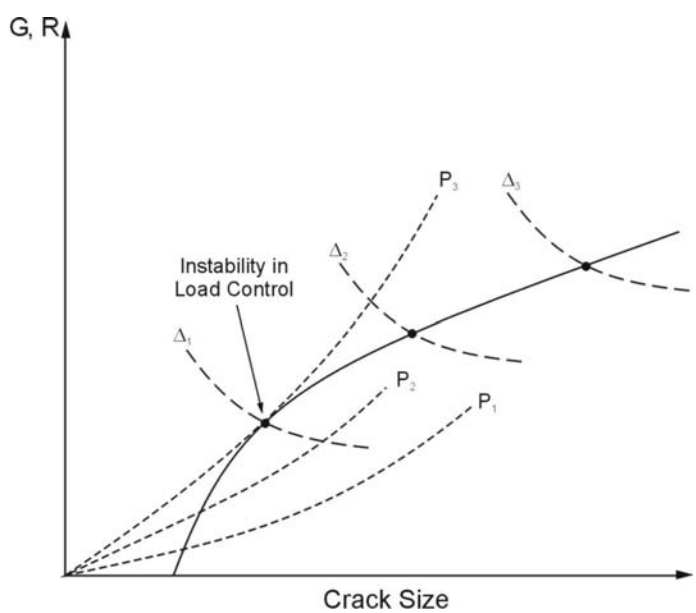

Figure 3-3: Diagram Comparing the Effects of Load- and Displacement Control

3.4 EXISTING TEST METHODS TO EVALUATE BOND STRENGTH

There are several commonly used test methods for evaluation of interfacial fracture energy at a flexible joint, including peel tests, pure shear tests and simple extension tests [12], as shown in Figure 3-4. These tests arrangements are primarily chosen to provide a simple means of characterizing bond strength, development length or crack propagation paths in CFRP-strengthened concrete specimens. Herein, an external load is exerted onto the concrete specimen causing eventual failure at the concrete/composite interface. Depending on the individual test configuration, ultimate bond strength may be calculated. As may be noted from Figure 3-4 a) and b), a majority of test methods utilize pure mode II fracture, which is why they are most commonly used to evaluate bond strength, given the fact that these test arrangements mostly do not allow for a simple way of measuring crack propagation length. Likewise, pull-off tests illustrated in Figure 3-4 d) may be used to evaluate ultimate strength at bond failure but are rather unsuitable for more sophisticated fracture analysis. In contrast, test arrangements depicted in Figure 3-4 c) and e) have been successfully applied to assess critical energy release rates during debonding [12], [11], [17]. Compared to previously discussed test arrangements, these configurations benefit from a mixed-mode failure in which both opening (mode I) and sliding (mode II) may be investigated. As a result, propagation of the crack front can be observed more easily. Also, latter test methods are supposed to represent a failure mode often encountered under service conditions [12].

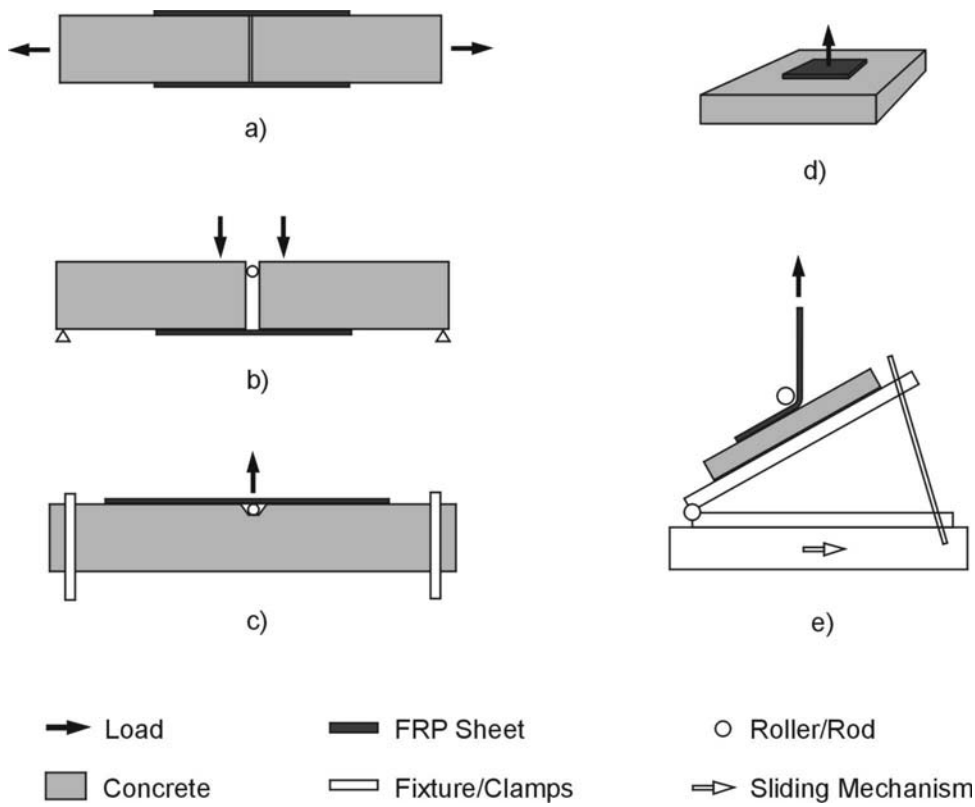

Figure 3-4: Various Fracture Test Methods

3.5 EXISTING DATA REDUCTION METHODS

To interpret the data recorded during fracture testing, several so-called data reduction methods may be used. These can be grouped in two categories, compliance methods and direct energy methods. In the following, the most popular methods will be introduced.

3.5.1 COMPLIANCE METHOD

On of the simplest and most common ways to determine the energy release rate of a tested specimen is to consider the change in component compliance as the crack propagates through the material. As given by Equation (3.5), the potential energy of a tested component is equal to the difference between the internal strain energy and the work done by any external forces. Considering a linear elastic material behavior, as shown in Figure 3-5, the internal strain energy stored in the component at any time is represented by:

$$U = \int F d\Delta = \frac{1}{2} F\Delta \tag{3.9}$$

Using Equations (4) and (5), this yields:

$$G = \frac{F}{2B}\left(\frac{d\Delta}{da}\right)_P \tag{3.10}$$

Since the compliance is defined as the inverse of the stiffness of a material, it can thus be written as $C = \Delta / F$, allowing rewriting Equation (3.10) in the following form:

$$G = \frac{F^2}{2B}\frac{dC}{da} \tag{3.11}$$

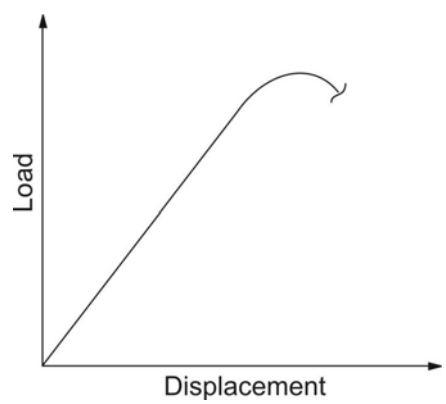

Figure 3-5: Linear-elastic Material Behavior of CFRP

Consequently, to evaluate fracture energy release rate of a test specimen simply requires calculating the derivative of component compliance with respect to crack length, *a*. However, it should be noted that use of Equation (3.9) demands linearity of the load-

deflection behavior of the specimen. Thus, this is an important limitation of the compliance method that restricts its use for test configurations experiencing a nonlinear load-deflection behavior.

3.5.2 COMPLIANCE CALIBRATION METHOD

Compliance calibration represents an alternative way to reduce data obtained form a fracture toughness test. In this approach, component compliance is measured for several crack lengths and graphed in a plot similar to that depicted in Figure 3-6. Subsequently, the data points are fitted by a polynomial expression (left graph) that may be differentiated with respect to the crack length to yield dC/da [10]. In situations where a straight line of slope *m* may correlate the data points, as is the right graph, fracture energy release rate can be calculated from:

$$G = \frac{F^2}{2B} m \tag{3.12}$$

While this method has the advantage that it does not require an analytical expression for the compliance, many tests must generally be conducted to generate representative compliance versus crack length data [10].

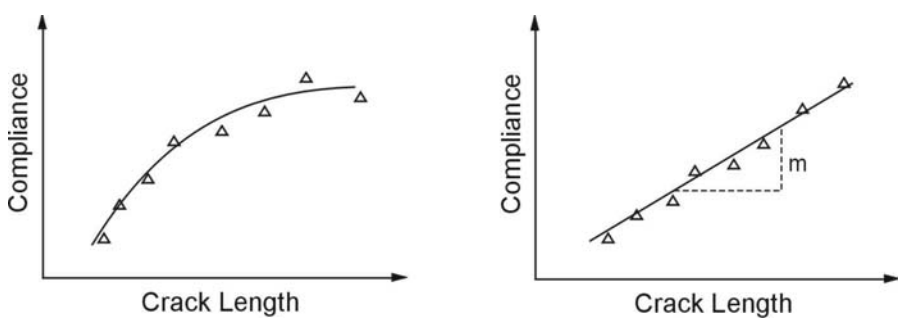

Figure 3-6: Graphical Methods used in Compliance Calibration

3.5.3 AREA METHOD

As an alternative to the compliance methods discussed previously, fracture toughness can be evaluated using a direct energy measurement, such as the area method. This method is based on the fact that energy release rate may be obtained from the area encircled by the load-deflection curve during a single loading cycle, i.e. dissipated energy, ΔA, divided by the area of crack propagation, $B \cdot \Delta a$, thus:

$$G = \frac{\Delta A}{B \cdot \Delta a} \tag{3.13}$$

A graphical representation of the method is given in Figure 3-7. In contrast to the compliance methods, for which only linear elastic response can be treated, this method is still valid if nonlinear load-displacement response is observed [10]. However, since this method is energy-based, it is only applicable to stable crack propagation, as kinetic

energy terms become significant for unstable crack jumps and must thus be included in the calculation. Lastly, successful application of the area method requires successive loading and unloading, making this approach much more time intensive.

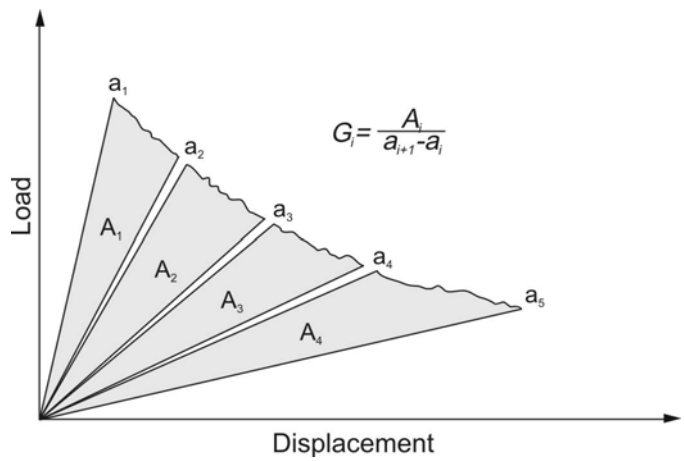

Figure 3-7: Graphical Representation of the Area Method

3.5.4 CONTINUOUS PEEL METHOD

Recently, a modification of the compliance method has been proposed to evaluate energy release rate for systems experiencing nonlinear load-deflection behavior [17]. The development of the following theory was mainly driven by the restrictive nature of the compliance approach to linear systems.

First, assuming an arbitrary system as in Figure 3-4 c), equilibrium of forces between the stressed material and external loading mechanism is used to derive an analytical expression for the loading force, *F*. Subsequently, strain energy, *U*, stored in the material can be calculated as follows:

$$U_s = \int_{a=const} F(\Delta) d\Delta \tag{3.14}$$

Herein, integration is performed with respect to Δ under the condition that debonding length, *a*, remains constant. Finally, differentiation of the strain energy with respect to *a* under the condition that Δ remains constant gives:

$$G = -\frac{d\Pi}{B \cdot da} = -\frac{dU_s}{B \cdot da} \tag{3.15}$$

From Equation (3.15), it is noteworthy that the potential energy of deformation, Π, is derived only from strain energy stored in the material, given the fact that no external work is performed on the system. Hence, above methodology allows evaluating fracture toughness of nonlinear systems without the need for successive loading and unloading as is required when utilizing the area method.

It should finally be noted that no effect of different crack propagation paths is taken into account in the above equations, which only provide means to calculate the global fracture energy [13].

4 REVIEW OF PREVIOUS RESEARCH

Conditioned by the continuously increasing use of CFRP materials for external rehabilitation of structural components, evaluation of fracture toughness has recently been the focus of numerous research studies. Herein, particular attention has been given to assess the efficacy of surface treatment techniques, as well as selection of primers, adhesives, and saturating resins [12], [13], [15], [17].

There exist many established test methods for determining mode I fracture toughness between adhesives and metallic substrates. For example, ASTM standard D 3433-93 [18] defines a test procedure suitable for testing mode I fracture toughness of bonds between symmetric metallic plates using DCB specimens. ASTM standard D 5528-94a [19] extends this method to composite materials. However, no standardized test method is currently present in the literature that specifically addresses testing of bond fracture toughness of composite overlays applied to concrete substrates [15].

To experimentally evaluate fracture toughness, concrete specimens are typically of small dimension and are cast in a separate mold and allowed to cure until they attain adequate strength. Subsequently, surface treatment is performed by either bead blasting, sandblasting or a similar abrasion technique to increase the "bondable" surface area and further enhance mechanical interlock between the substrate and composite materials. A thin composite strip is then bonded to the concrete surface and allowed to cure until the resin/adhesive has attained sufficient strength and stiffness. As mentioned earlier, a thin film of non-adhering material is typically included at the concrete/composite interface to serve as an initial pre-crack. Ultimately, the composite material is loaded and crack propagation is monitored either sequentially or continuously throughout the test. In the following, several successfully utilized test methods will be introduced and discussed. It is noteworthy that all of the subsequently discussed test programs have evaluated fracture toughness based on analytical methods described in Chapter 3.

Using a test configuration similar to that shown in Figure 3-4 c), Ye et al. studied the effect of different abrasive procedures and selection of primer, using both an epoxy resin and vinyl ester resin as possible adhesives. They further included examinations of the fracture surfaces to identify different fracture mechanisms.

Test parameters of this study included differences in the initial surface condition of the concrete specimens, methods of pre-treatment as well as use of adhesives. More specifically, two types of concrete surfaces were used. The first was the original surface after releasing specimens from the mold, while the second was obtained after removing a surface layer of about ¼-in (6.4-mm) from the concrete panels by the use of a diamond saw. Whereas the former surface contained a low aggregate content due to buoyancy effects, the latter showed a high aggregate content (HAC).

On several specimens, abrasion was performed using two different kinds of abrasive papers, one showing a fine particle size (GP size#400) and one with significantly coarser particles (GP size#80). Further, a different set of specimens was treated using a regular metal brush in either manual (random direction) or automated (0° and 90° directions) operation while yet another set was sandblasted at angles between 70° and 90° to the surface normal.

The composite used in this study was made from 10 layers of unidirectional carbon fiber epoxy prepreg laminates, processed in an autoclave. After cure, plates were cut into strips of 20 x 250 x 1.45-mm. Prior to bonding, the composite surface was treated using aforementioned sandpaper, followed by acetone cleaning and subsequent drying. At the center location, a film of 12.5-μm thickness was placed between the concrete and composite strip to produce a pre-crack of 1.57-in (40-mm).
Testing of the CFRP/concrete specimens was performed using a cross-head speed of 0.008-in/min (0.2-mm/min) with continuous recording of the load-deflection curve. Further, a stereo microscope was used to observe crack growth at about every 0.2-in (5-mm). For data reduction, the compliance calibration method was used, allowing correlation between the compliance and crack length by a straight line. A minimum of three specimens was tested for each condition.
Results of this study indicated a strong dependency of fracture toughness on the methods of concrete surface treatment. As such, highest values of fracture load were obtained for sandblasted specimens showing an HAC surface. Also, compared to perfectly smooth surfaces, specimens formerly treated with GP size#400 sandpaper showed a significant increase in fracture energy. From these findings, it can be stated that mechanical surface treatment improves bond strength to a significant degree. Findings further indicated a substantial difference in fracture energy between systems employing vinyl ester and epoxy resin systems. More specifically, adhesion fracture energy of vinyl ester-bonded specimens was only about 20% of that for specimens using the epoxy resin system.

Giurgiutiu et al. [15] tested fracture strength of composite overlays using principles and practices of existing ASTM standards with an extension to cover the case of elastic composites bonded to rigid concrete/masonry substrates. Their test setup, schematically depicted in Figure 4-1, led to an analytical approach using the compliance-based formulation as discussed in Section 3.5.1. However, to correct for possible specimen rotation at the crack front, they applied a modified beam theory in which the specimen is treated as if it contained a slightly longer disbond, *a'*.

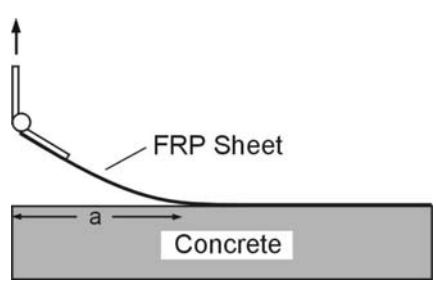

Figure 4-1: Schematic Representation of Mode I Fracture Test

Concrete test specimens used in this study were fabricated from commercially available constituents and measured 2 x 2 x 7-in (51 x 51 x 178-mm). Fabrication encompassed four different stages, including casting, cure, wire brushing and vacuuming. The cleaned surface was primed followed by wet layup of the composite material using a polyester resin and peroxide initiator (MEKP type). A quad axial glass fiber mat was used as the

reinforcing material. After a three-layer sequence, the material measured 0.125-in (3.5-mm) in thickness. Upon completion of cure, which was taken after a minimum of 24 hours, a razor blade was tapped into the specimen to induce the pre-crack. White fluid was applied to the interface between the composite overlay and substrate to facilitate observation of crack growth.

Interestingly, this study was aimed primarily at investigating the effect of fabrication knowledge and operator experience. During the experimental program, a first set of specimens was fabricated, tested, followed by subsequent analysis of the results. A second set was then fabricated, thus benefiting from knowledge gained during manufacturing and testing of the first set of specimens. Also, the second set was fabricated by an operator with more experience in composite fabrication. This allowed simulating the influence of human-factor variability.

Testing was performed monotonically under displacement control, using a vertical cross-head velocity of 0.31-in/min (7.8-mm/min). When a drop in load or new crack growth could be observed, testing was paused. The crack was then allowed to propagate until no further propagation could be noticed. Finally, crack length was recorded and loading resumed until the next noticeable occurrence.

An examination of the test results revealed several important aspects. Firstly, specimens fabricated by an inexperienced operator presented extensive data scatter and lower fracture toughness compared to the ones manufactured by experienced personnel. Also, the second set of specimens showed only little data scatter. This underscores the importance of training, experience, and quality control when applying composite overlays to structural components in the field. Moreover, results indicated a trend between fracture toughness and the percentage of fracture surface retaining cement paste. As such, visual examination revealed that the amount of cement paste retained on the fracture surface is typically higher for specimens with high fracture toughness. This indicates that good bond is associated with a fracture path propagation through the concrete substrate. However, since the cement paste in the upper layers of the concrete is weaker than the bulk material, crack propagation will at always tend to propagate along the paste-rich upper region.

An alternative approach to investigate fracture toughness between CFRP and concrete was proposed by Xie and Karbhari [12]. Their test setup, similar to that shown in Figure 3-4 e), utilized a concrete specimen fixed on a rotating platform that allowed investigating fracture toughness under various peel angles. Herein, a roller, situated above the composite material, was used to facilitate control of the crack front. The test further examined the effect of various peel rates by varying cross-head velocity.

In the course of test preparation, the concrete material was subjected to mechanical abrasion by means of bead blasting, resulting in a nonplanar surface that would increase surface area and promote mechanical interlock. The carbon fiber material used in this study consisted of dry unidirectional two sheets attached to a glass scrim fabric containing a layer of resin adhesive. After epoxy was applied to the pretreated concrete surface, a single layer of the tow sheet was placed in intimate contact with the substrate to ensure good and even contact between both adherents. After insertion of a 1 inch-long (25.4-mm) pre-crack, the peel test specimens were allowed to cure for a minimum of one week. Average thickness of the cured composite was determined as 0.016-in (0.4-mm).

As indicated, testing of the specimens encompassed two different study parameters, namely peel angle and cross-head velocity. More specifically, peel angles of 30°, 45° and 60° and four velocities of 0.05-in/min (1.27-mm/min), 0.1-in/min (2.54-mm/min), 0.2-in/min (5.08-mm/min) and 0.5-in/min (12.7-mm/min) were investigated.
Considering data analysis, the present test setup allowed a more simplified approach in that it did not require sequential measurement of the crack front, given the fact that fracture always occurred near the location of the roller. Hence, simple equilibrium equations could be utilized to obtain a measure for fracture toughness. Nonetheless, it should be noted that, given the high curvatures near the roller, this test configuration is only applicable for extremely thin composite materials.
Results of this test indicated that when the peel angle increased, or peel rate decreased, fracture toughness was increased. It was further found that crack propagation along the interface between CFRP and concrete yielded the lowest fracture energy and is thus the most likely failure path.

Finally, Kimpara et al. [17] and Yamaguchi et al. [11] proposed an alternative peel test to characterize fracture toughness using a so-called *membrane peel method*. Schematically, their test configuration is similar to that shown in Figure 3-4 c). In their study, they confirmed applicability of the proposed methodology by comparing results from two analytical approaches, the area method analysis and membrane peel analysis. Moreover, the effect of different surface treatments was investigated. The promising characteristic of this test arrangement is that it assesses mixed-mode fracture at peel angles similar to those often encountered in structural applications.
To evaluate bond strength, this test utilized a long, prismatic concrete specimen with a center notch used to accommodate the peeling mechanism. After placement of an FRP sheet and induction of an adequate pre-crack, the concrete prism is placed into a specially designed steel fixture and clamped at the far ends of the specimen. Then, a steel rod, which is connected to the vertical loading mechanism of a testing frame, is inserted into the notch. Upon vertical displacement of the steel rod, the initially debonded material is forced to strain. Ultimately, once the driving force overcomes the material resistance, peel is initiated. It can be shown that, if operated in displacement control, peeling occurs in a stable manner. While the analytical background for this test configuration was given in Section 3.5.4, detailed analysis for the possible case of asymmetric peel has not yet been discussed. In this context the reader is referred to Chapter 7. It should finally be noted that previous tests have indicated limited applicability of this test method with respect to excessive membrane thicknesses. As such, composite membranes of aspect ratio less than 200 appeared unsuitable for investigation. Herein, aspect ratio was defined as length of pre-crack divided by material thickness.
A further unique characteristic of this study was the continuous measurement of crack propagation using two linear variable differential transformers (LVDT) located on either side of the loading head, as shown in Figure 4-2. During peeling, LVDT's were used to measure the relative vertical displacement of the composite membrane. From simple trigonometric relations, the approximate location of the crack could be calculated.
As mentioned, the proposed data reduction method was applied to investigate effects of different surface treatments and primer on bond strength. Herein, energy release rates were comparatively evaluated based on the area method and membrane peel method [17].

CFRP sheets used in this study measured 2.95-in (75-mm) in width, 0.03-in (0.75-mm) in thickness and 19.7-in (500-mm) in length. The initial debonding length, a_0, was 1.18-in (30-mm). Three different kinds of surface treatment were evaluated: the first was no treatment whatsoever, the second was treatment with a disk sander of GP size#20 and the third with that of GP size#100. Among these, one was treated with a primer while a second one remained unprimed. Thus, a total of six specimens were prepared.

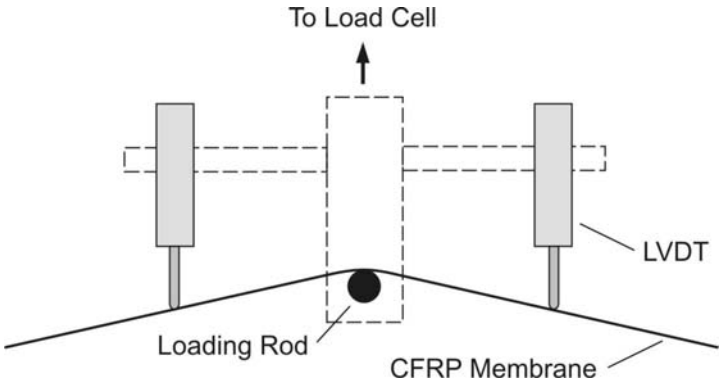

Figure 4-2: Measurement of Crack Extension using Linear Variable Differential Transformers

The cross-head velocity was set to 0.02-in/min (0.5-mm/min) with continuous recording of the load-deflection curve. While data from the LVDT's was used to obtain fracture energy for the membrane peel analysis, an optical magnifier was used to observe crack growth for evaluation using the area method.

Results showed that while fracture energy tended to increase with an increase in surface roughness, the effect of priming was minimal. In general, it was shown that the proposed analytical method provided reasonable results when compared to results obtained from the area method.

5 RATIONALE OF STUDY

Considering the predominant mechanisms utilized in structural rehabilitation, adequate bond strength between CFRP and concrete must be viewed as an essential precondition. As outlined in the previous Chapter, minimal variation in surface preparation techniques as well as differences in choice of constituent materials can adversely affect bond and hence yield any rehabilitation effort ineffective. Although past research efforts have provided insight to preferable surface treatments as well as the most suitable material systems, a large number of parameters yet remain uninvestigated. Herein, defects possibly represent the most important parameter to be considered [1], [2]. Thus, their criticality must be established to provide a classification scheme that allows engineers to assess severity, depending on defect type, location, size or shape. In the following, a rationale for such classification will be introduced.

As previous discussions have shown, there exist several test methods to evaluate fracture energy of CFRP-rehabilitated concrete specimens. Further, a direct relationship between bond strength and fracture energy release rate appears to exits in that adequate bond strength reflects high fracture energy while lower fracture energy is often representative of poor or lower-quality bond. Hence, it appears reasonable to establish bond quality based on findings of a suitable fracture energy test.

While a variety of test methods exist, not all may be suitable in representing mechanisms of structural elements. As outlined in Chapter 2, CFRP overlays are mostly loaded and possibly peeled from the underlying base in a sliding mode (mode II). Nonetheless, relative out-of-plane movement of the two separating substrates may also partially induce an opening stress, i.e. mode I fracture. While end-plate failure was given as a first incidence of mixed-mode fracture, a second is represented by crack opening in combination with relative out-of-plane movement at the bottom of a flexurally reinforced beam. As shown in Figure 5-1, excessive yielding of internal stirrups may results in a substantial relative displacement of the two crack faces, hence inducing mixed-mode fracture. Hence, because disbonding in a CFRP-rehabilitated structural component is unlikely to experience pure mode I or mode II loading, it appears preferable to utilize a test method that investigates a mixed-mode failure while testing predominantly in mode II.

Given the need to quantify and interpret findings of an experimental fracture analysis, criticality must be expressed in relative terms, i.e. a baseline for adequate bond strength derived from an essentially defect-free specimen must be established. To provide such baseline, a set of control specimens with ideally no internal defects must be provided. Values of fracture energy obtained for these control specimens can then serve as a baseline for further testing. Accordingly, criticality is based on a relative reduction in fracture toughness between control specimens and the remaining specimens containing individual defects.

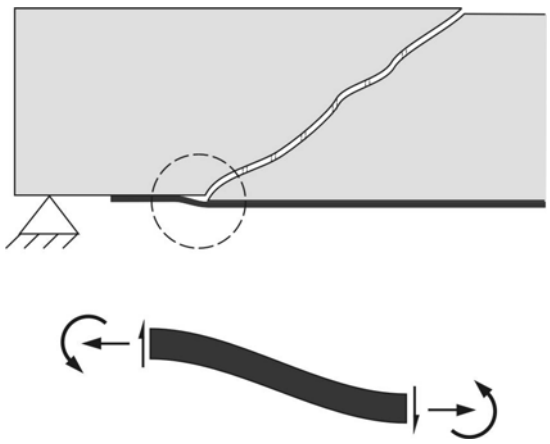

Figure 5-1: Possible Mixed-mode failure in CFRP-rehabilitated Beams

6 SETUP AND RATIONALE OF TEST ARRANGEMENT

6.1 INTRODUCTION

To assess bond strength of CFRP-rehabilitated specimens containing artificially induced defects, an approach similar to that proposed by Yamaguchi [11], [20] was used. This specific configuration appeared favorable mostly due to the fact that a mixed-mode fracture phenomenon could be examined combined with the effect that two crack fronts could be studied simultaneously. In addition, it had been shown that an analytical model could be obtained that allows testing in a continuous manner instead of using successive loading and unloading as required by the area method. Since continuous peel testing is substantially less time intensive, this approach seemed preferable.

Although the test configuration used in the present study widely adhered to implications given in [11] and [20], the test configuration was modified to accommodate materials currently utilized in field-rehabilitation. Herein, specimen dimensions were increased since a slightly thicker composite membrane was utilized. Also, instead of measuring via use of LVDT's, crack propagation was monitored using an alternative system that allowed a more exact determination of crack front propagation. Details are given below.

6.2 CONCRETE SPECIMENS

Concrete specimens used in this study measured 56-in (1422.4-mm) in length, 3-in (76.2-mm) in height and 3.5-in (88.9-mm) in width. These dimensions were primarily chosen due to the following reasons. Firstly, findings of Yamaguchi et al. [20] have shown that there exists a minimum length in pre-crack depending on the thickness of the membrane material used in the test. Herein, it was found that their analytical model would only be applicable to aspect ratios greater than 200. Given the typical thickness range of 0.04 to 0.06-in (1.02 to 1.52-mm) for currently utilized CFRP materials, a pre-crack length of 14.75-in (374.7-mm) was thus chosen. To further provide a sufficient distance of bonded material including space to clamp the specimen to the test fixture, overall length was taken to be 56-in (1422.4-mm). Secondly, to allow testing of relatively large defects, herein defined as diameters up to 1-in (25.4-mm), a composite width of 3-in (76.2-m) appeared most suitable. This selection was further supported by the fact that most previous studies have employed materials of similar width [15], [20]. Conditioned by the fact that an alternative approach to monitor crack growth would be employed in the present study (see Section 6.5 for further details), the concrete specimen had to be of slightly greater width compared to the composite overlay. Consequently, a width of 3.5-in (88.9-mm) was chosen. Finally, due to the requirement for mobility during specimen preparation, including casting, storage, surface treatment and layup of the CFRP composite, specimen weight was limited such that a single person could easily move them. In their current geometry, a specimen weight of approximately 50-lb. (23-kg) was predicted. Also, to accommodate the pulling mechanism of the cross-head, a notch of approximately ½-in (12.7-mm) was included at the center of each specimen.

A schematic illustration of the test specimen, showing the three predominant zones, is depicted in Figure 6-1.

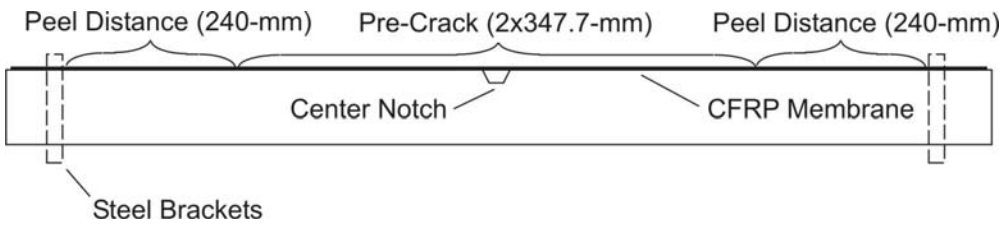

Figure 6-1: Layout of Concrete Test Specimens

6.3 TEST FIXTURE

The steel fixture used in the present investigation was specially designed to accommodate the concrete specimens and further allow testing of in an Instron 5583 test frame. To minimize testing errors, a high flexural stiffness was required, as specimens would later be clamped at either end of the fixture. Assuming test loads of approximately 450 to 674-lbf (2 to 3-kN) the maximum vertical deflection at both ends of the test fixture was limited to 0.004-in (0.1-mm). To obtain such high flexural stiffness, a square steel tube section, measuring 6 x 6 x 0.25-in (152.4 x 152.4 x 6.35-mm) was used. The fixture was attached to the loading base of the Instron test frame by means of a steel plate that was welded to the W-section. Connection to the Instron occurred using four M-10 steel bolts. To minimize corrosion, the fixture was wiped with acetone and sprayed using a rust inhibitor.

Upon complete drying of the rust inhibitor, a sheet of self-adhering mastic tape was placed onto the top surface of the steel fixture. The 0.08-in (2-mm) thick material served as padding and would later reduce stress concentrations due to irregularities in the bottom surface of concrete specimens. To keep a fixed position during testing, the concrete specimens were clamped to the steel structure using two brackets that could be inserted through the tube section and bolted down at the opposite side.

Finally, as discussed in Section 6.5, four video cameras were attached to the test fixture to continuously monitor crack propagation during testing. To allow variable vertical positioning while keeping a constant distance from the concrete specimen, two rows of ¼-in (6.35-mm) threaded holes were included along the sides of the steel fixture. As such, the extension arms holding the video cameras could be arrested at various positions. An exploded illustration of the steel fixture and its individual components, including camera designation, is shown in Figure 6-2.

6.4 LOADING MECHANISM

For all tests, an Instron 5833 load frame was used. To accommodate the 56-in long concrete specimens, the steel fixture was positioned perpendicular to the base of the frame. The loading rod, which would later serve to peel the composite membrane off the concrete substrate, could be inserted through a steel bracket that was directly attached to a 10-kN load cell (see Figure 6-3). The complete assembly is depicted in Figure 6-4.

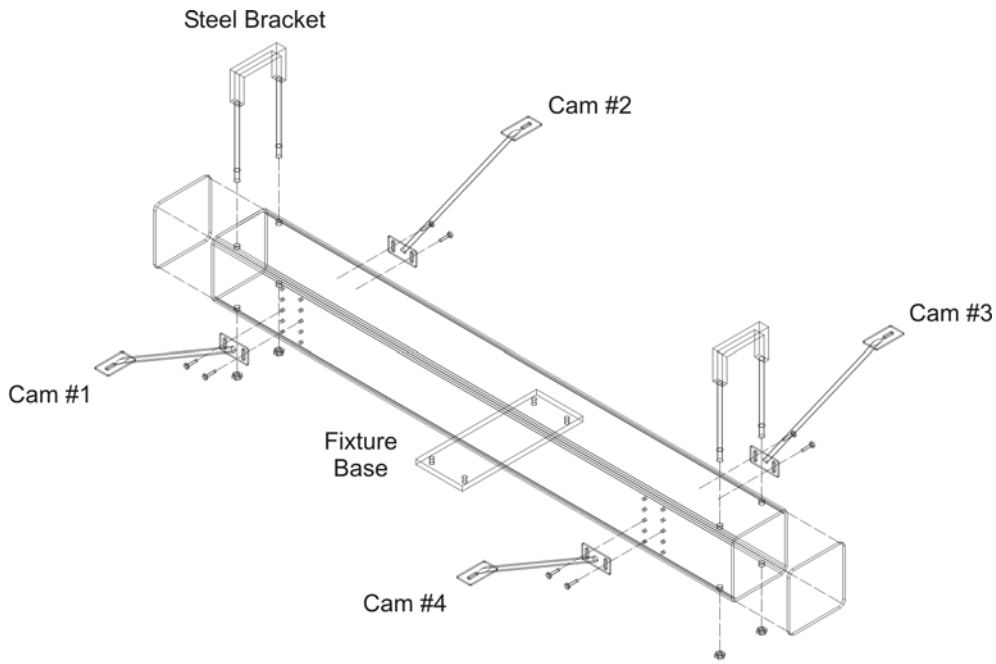

Figure 6-2: Exploded View of Test Fixture

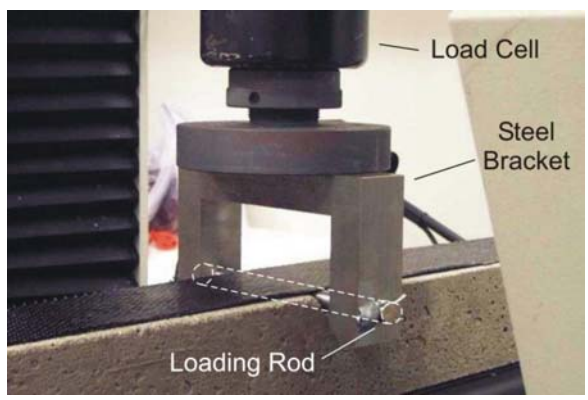

Figure 6-3: Loading Rod Assembly

6.5 VIDEO MONITORING SYSTEM

6.5.1 RATIONALE AND GENERAL LAYOUT

During their test, Yamaguchi et al. [11], [20] have evaluated crack propagation using two LVDT's located at either side of the loading cross-head. While this is a permissible approach to identify location of the crack front, certain drawbacks of the method should be addressed.

Foremost, given the fact that only a single LVDT is utilized per side, location of the crack front is obtained from only a single measurement without exact knowledge of the crack length at either side of the composite membrane. Naturally, due to the relatively large width of 3-in (76.2-mm) of the composite strip and the typically inhomogeneous nature

of the concrete surface, large variations in crack front propagation may be expected. Further, at large cross-head deflections, the position the LVDT-tip may be significantly moved out of the projected vertical position, as shown in Figure 6-5, resulting in erroneous calculation of the crack location. Finally, even thin composite membranes develop small curvature near points of inflection, i.e. at the pulling rod as well as directly adjacent to the growing crack. Hence, the trigonometric relationship would tend to predict a larger crack extension than actually encountered, as illustrated in Figure 6-6.

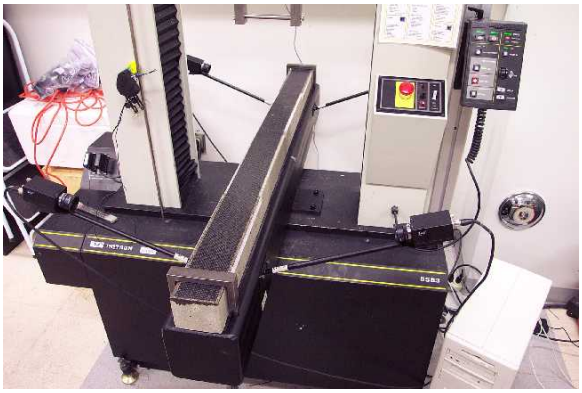

Figure 6-4: Completed Test Assembly

From the above, it appears feasible to employ an alternative crack monitoring system that is not affected by aforementioned factors. Consequently, the present investigation utilizes a system that allows direct visual monitoring of each of the four crack fronts. As such, differences in crack propagation can be identified.

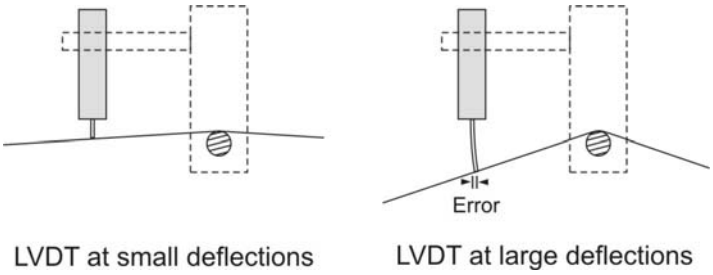

Figure 6-5: Horizontal Deflection of LVDT-tip due to Large Deflections

The general layout of the monitoring system is depicted in Figure 6-7. As may be observed, a single CCD camera located at a fixed distance from the concrete specimen monitors each crack front. Each camera is positioned on a steel arm and slightly tilted downward to enhance clarity of the recorded images. Peel distance is correlated by means of a paper ruler located just below the crack line. To enhance contrast of the recorded image, edges of the cured CFRP overlay are primed using a brittle, white fluid.

During peeling, images are transferred to a nearby computer system and recorded for subsequent evaluation. By directly monitoring each crack front, the disbonded area is calculated as the average of the individual measurements.

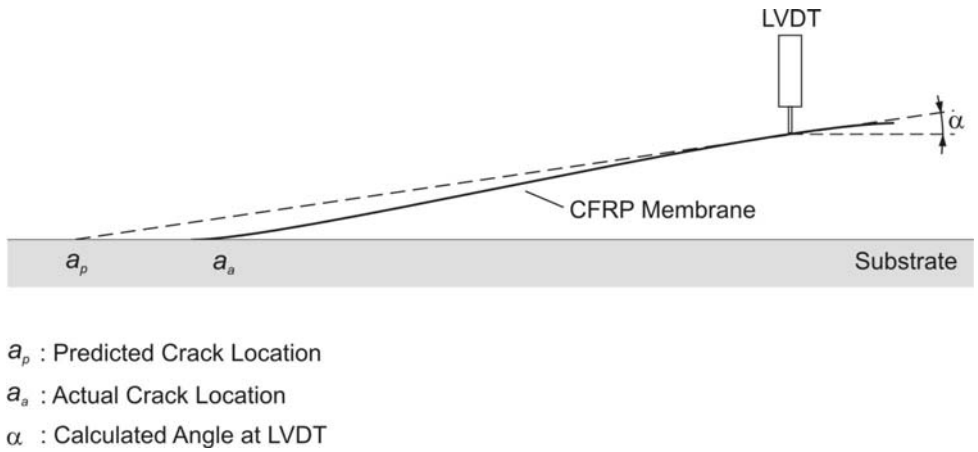

Figure 6-6: Erroneous Prediction of Crack Extension due to Flexure of Membrane

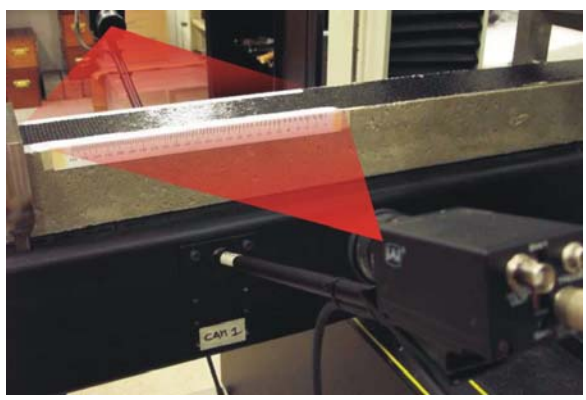

Figure 6-7: Camera Layout for Crack Monitoring

6.5.2 HARDWARE

The recording hardware consisted of four CCD cameras connected to a PC that housed a video recording card, commonly referred to as *framegrabber*, which was capable of simultaneously recording images from four different cameras. During testing, images of all four crack fronts could be displayed on a computer screen and were recorded for later evaluation. A discussion on the functionality of individual components is given in the following Sections.

6.5.2.1 CCD Cameras

Four JAI CV-M50 RS-170 monochrome analog cameras were used for crack monitoring. The cameras display a black and white image and are capable of recording a maximum of 30 fps. Each camera was equipped with a Cosmicar C814 8.0mm f1.4 manual iris lens, which, when placed 16.1-in (408.9-mm) from the object to be viewed, results in a camera

field of view of 10-in (254-mm). Maximum dimensions of each camera image are 640x480 pixels. Considering the aforementioned field of view, this results in a representative pixel size of less than 0.016-in (0.4-mm). An image of the camera is shown in Figure 6-8.

6.5.2.2 Four Channel Framegrabber

A single slot, PCI bus Viper-Quad video acquisition card from Coreco imaging was used to simultaneously record images to the hard drive of the computer system. It features four independent acquisition channels, each comprised of an 8-bit analog to digital converter. Cameras are connected to the card via four cables with 12-pin Hirose connectors that also supply camera power. Hence, no additional power source is required. The Viper-Quad card is pictured in Figure 6-9.

Figure 6-8: CCD Camera

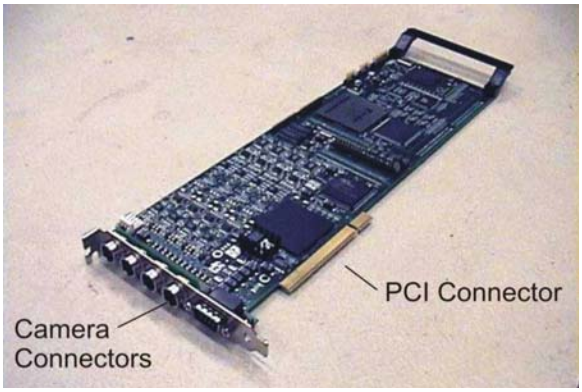

Figure 6-9: Viper Quad Video Framegrabber

6.5.3 SOFTWARE

Apart from the driver software required to operate the video acquisition card, the digital video recording software Video Savant by IO Industries was used to display and analyze the recorded images. The software allows simultaneous live image viewing and recording to hard drive. Using a special device driver, image size of each video camera

was changed from 640 x 480 pixels to 640 x 150 pixels to allow simultaneous displaying of all four camera images, as shown in Figure 6-10. The software further enables the user to alter the picture sampling frequency, i.e. frame rate. This refers to how many pictures are recorded by each of the cameras over a period of time. Due to limitations set forth by the system memory, a maximum of 351 images per test could be recorded. Further, given the need to synchronize data acquired by the Instron test frame and that recorded by the video recording software, special stream filters were utilized that allow each image to receive a "time stamp". As such, load-displacement data and crack propagation could later be correlated.

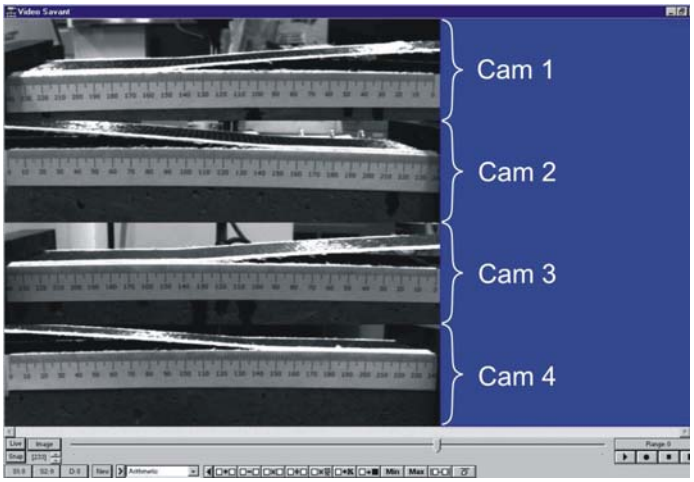

Figure 6-10: Image of Crack Propagation using Video Savant Software

7 THEORY OF ANALYTICAL MODEL

In the following, an analytical model for calculating fracture energy release rate (FERR) for a test arrangement as described in the previous Chapter is given. Herein, it is assumed that the composite material can be treated as a thin, linear elastic membrane, i.e. the strain energy stored in the material is predominantly due to pure elongation. Initially, only the case of equal left and right disbonding length will be considered. In the following model, the load is introduced to the CFRP membrane by means of a round loading rod. It is further assumed that the brittle nature of the resin inhibits significant losses in energy dissipation at the crack fronts. Finally, given the extremely low velocity of testing, kinetic energy terms are further neglected.
Considering the equilibrium of forces between the loading rod and CFRP membrane, as depicted in Figure 7-1, the relationship between external force, *F*, and internal membrane force, *S*, can be expressed by:

$$F = 2S \sin\theta \tag{7.1}$$

where θ represents the angle enclosed by the horizontal axis and the CFRP membrane.

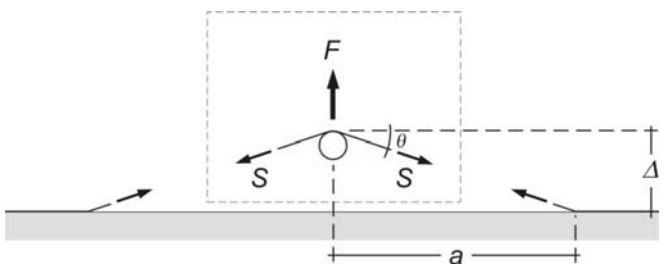

Figure 7-1: Force Equilibrium at Point of Load Introduction

From trigonometric relations, θ can then be written as:

$$\sin\theta = \frac{\Delta}{\sqrt{\Delta^2 + a^2}} \tag{7.2}$$

with Δ and a representing vertical cross-head displacement and crack length, respectively. The membrane force can then be written as

$$S = \sigma \cdot A_C = \varepsilon \cdot E_{11} \cdot A_c \tag{7.3}$$

where A_c is equal to the area of the composite membrane, and $A_c = B \cdot t$, i.e. membrane width multiplied by membrane thickness. Finally, the strain, ε, in the membrane is given by:

$$\varepsilon = \frac{\sqrt{\Delta^2 + a^2} - a}{a} = \frac{\sqrt{\Delta^2 + a^2}}{a} - 1 \tag{7.4}$$

Substituting Equation (7.4) into Equation (7.1) results in:

$$F = 2E_{11}Bt\frac{\Delta}{\sqrt{\Delta^2 + a^2}} \cdot \left(\frac{\sqrt{\Delta^2 + a^2}}{a} - 1 \right) \tag{7.5}$$

Upon defining a new ratio $x = \Delta / a$, Equation (7.5) may be rearranged to result in the following expression:

$$F = 2E_{11}Btx\left(1 - \frac{1}{\sqrt{x^2 + 1}} \right) \tag{7.6}$$

Equation (7.6) thus provides a simple expression to correlate between vertical cross-head displacement and external load acting on the loading rod. To obtain the elastic strain energy, U_s, stored in the composite membrane, Equation (7.6) must be integrated with respect to Δ under the condition that disbonding length, a, remains constant and the initial condition of $U_s(x = 0) = 0$ be satisfied. Upon integration, the strain energy may be given as:

$$U_s = 2E_{11}Bt\left(\frac{\Delta^2}{2a} - a\sqrt{\frac{a^2 + \Delta^2}{a^2}} + a \right) \tag{7.7}$$

Given Equations (3.4) and (3.5), fracture energy release rate of the system is now defined through:

$$G = E_{11}t\left(\frac{x^2}{2} + \frac{1}{\sqrt{x^2 + 1}} - 1 \right) \tag{7.8}$$

It should be noted that Equation (7.8) has been evaluated assuming a constant cross-head deflection as well as the simultaneous formation of two crack fronts. As a result, FERR of the system can be calculated by measuring vertical deflection and crack propagation throughout progression of the test, presupposing that the material properties, i.e. width, B, thickness, t, and tensile modulus, E_{11}, are known.

While Equation (7.8) is valid for systems that experience symmetric peeling, i.e. identical propagation of the crack fronts on both sides of the loading head, it must be assumed that such condition cannot generally be obtained during an actual experiment. Consequently, FERR must be established for situations where disbonding length is not equal on both sides. A general configuration for this situation is depicted in Figure 7-2. It can be noted that the two peel lengths can be found by assuming an average peel length, a, while introducing a term for the difference between both, herein denoted s. As such, the larger

disbonding distance is given as $a+s$ while the shorter one may be expressed as a-s [17]. From this, the relationship between external force, F, and vertical displacement can be expressed by:

$$F = \frac{1}{2} E_{11} Btx \left[2 + \frac{\sqrt{(1+\alpha)^2 + x^2}}{\sqrt{(1-\alpha)^2 + x^2}} + \frac{\sqrt{(1-\alpha)^2 + x^2}}{\sqrt{(1+\alpha)^2 + x^2}} - 2\left(\frac{1}{\sqrt{(1-\alpha)^2 + x^2}} + \frac{1}{\sqrt{(1+\alpha)^2 + x^2}} \right) \right] \tag{7.9}$$

where $\alpha = s/a$. It is noteworthy that the expression in Equation (7.9) is obtained by assuming equal internal membrane forces, S, i.e. equal strain on both sides of the pulling rod. This assumption will be further discussed in Chapter 8.

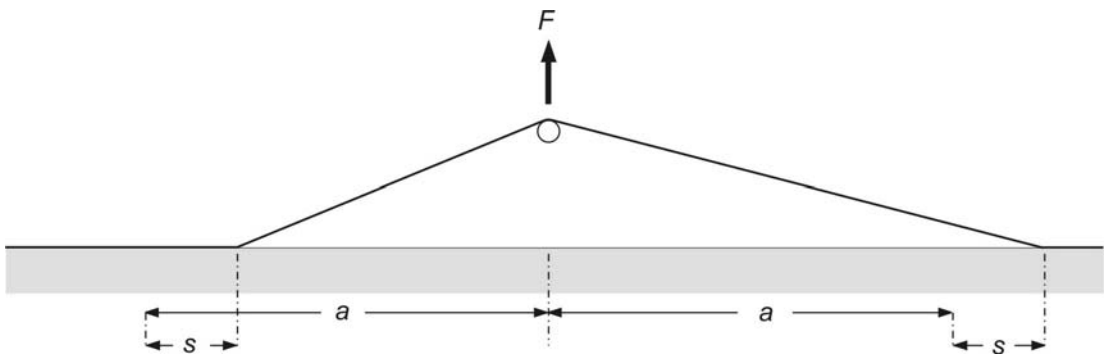

Figure 7-2: Geometric Relationship in Situations of Nonsymmetrical Peeling

Following a similar rationale as for Equations (7.7) and (7.8), elastic strain energy and FERR of the nonsymmetrical situation may now be expressed as:

$$U_s = E_{11} Bt \left[\frac{\Delta^2 + s^2 + 3a^2}{2a} - \sqrt{(a-s)^2 + \Delta^2} - \sqrt{(a+s)^2 + \Delta^2} + \frac{\sqrt{((a+s)^2 + \Delta^2)((a-s)^2 + \Delta^2)}}{2a} \right] \tag{7.10}$$

and

$$G = \frac{1}{4} E_{11} t \left[x^2 + \alpha^2 - 3 + \sqrt{(1+\alpha)^2 + x^2}\sqrt{(1-\alpha)^2 + x^2} + \frac{(1+\alpha)(2 - \sqrt{(1-\alpha)^2 + x^2})}{\sqrt{(1+\alpha)^2 + x^2}} \right.$$

$$+\frac{(1-\alpha)(2-\sqrt{(1+\alpha)^2+x^2})}{\sqrt{(1-\alpha)^2+x^2}}\Bigg] \tag{7.11}$$

It can be noted that for $\alpha = 0$, i.e. an equal left and right peel distance, the expression in Equation (7.11) reduces to that of Equation (7.8).

In conclusion, Equation (7.11) describes a data reduction method that allows calculation of FERR of the above system simply based on measurement of vertical cross-head deflection and crack propagation. Stability calculations for this system are presented in Appendix B.

8 VERIFICATION OF ANALYTICAL MODEL

8.1 INTRODUCTION

To assess feasibility of the analytical model presented in Chapter 7, an experimental validation program was established. Rationale of such program was to confirm the two elementary assumptions of the model, namely that:

- the composite material can be treated as a thin membrane, i.e. elastic strain energy stored in the material originates predominantly due to elongation, and
- the membrane encounters equal strain on both sides of the loading rod during unsymmetrical peeling, i.e. the composite material is capable of slipping over the point of load introduction (resulting in equal forces on either side).

To validate these preliminary assumptions, a total of six test specimens were fabricated and reinforced using two layers of carbon fabric infiltrated with an epoxy resin system. Three specimens (numbered *V-1* to *V-3*) were tested in a cyclic manner, using the well-known area method approach for subsequent data analysis. The remaining three specimens (*V-4 to V-6*) were tested in a continuous fashion and data analysis was performed according to the theoretical model given in Chapter 7. Additionally, due to the possible differences in surface conditions among the six specimens, an alternative analytical approach was applied to specimens *V-4* to *V-6*. This methodology allowed a direct comparison of results obtained from different analytical approaches, while using identical test specimens.

8.2 CONSTITUENT MATERIALS

8.2.1 CONCRETE SPECIMENS

The concrete mix used for fabrication of specimens contained Type I Portland cement and a maximum aggregate size of ½-in (12.7-mm). The 28-day design strength was given as 5000-psi (34.5-MPa). The mix was poured into a wooden mold of 280 x 57 x 3.5-in (7112 x 1447.8 x 88.9-mm) that contained intermediate dividers and allowed simultaneous casting of 70 specimens. Wedges were included at the bottom of the mold to form aforementioned center-notch. Also, by casting specimens upside down, a smooth test surface could be obtained. To facilitate easy demolding, all inner surfaces of the form mold were oil-sprayed.

Upon pouring, the concrete was internally vibrated and the top was steel-troweled. In addition to the concrete blocks, a total of 19 concrete cylinders were poured for later compression and split-ring tests (ASTM C 39 and ASTM C 496-96, respectively). To evaluate the 21-day (date of demolding) and 28-day compressive strength, a set of three cylinders was cast prior to pouring, after placement of specimen #35, as well as after completion of pouring. In-between each set of seven specimens, one cylinder was cast to evaluate long-term curing effects. These included cylinders prior to set #1-7 and following #64-70. Due to a logistic error, no cylinder was poured following set #8-14. A graphical representation of the specimen- and test cylinder layout is presented in Appendix C.

The freshly poured concrete was immediately covered with an impervious polypropylene sheet for a period of 21-days. After that period, the specimens were demolded, arranged in sequential order and stored at room temperature until needed. Images of the casting process are provided in Figure 8-1 and Figure 8-2.

Figure 8-1: Casting of Concrete Specimens

Figure 8-2: Specimens Prior to Storage

8.2.2 CFRP MATERIALS

8.2.2.1 Dry Fabric

The carbon fiber material chosen for the present study is a unidirectional Toray fiber provided on rolls of approximately 24 inches (610 mm) width. It employs point-glued transverse stitching, which results in a geometrically stable fabric that is generally difficult to distort (Figure 8-3), i.e. the possibility of shearing and wrinkling of the fabric are extremely limited. Physical properties of the material are listed in Table 9-3. To date

the material and has been utilized extensively in actual rehabilitation projects throughout the state of California.

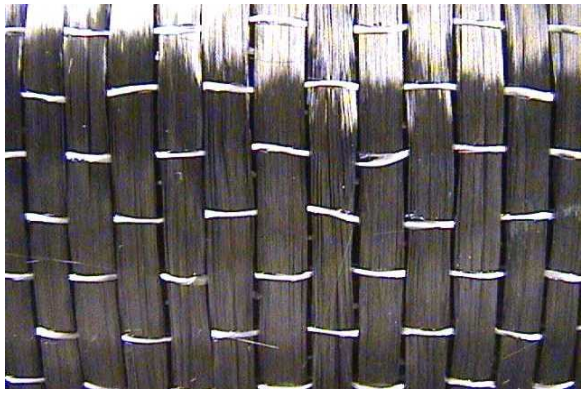

Figure 8-3: Close-up Image of T-700 Carbon Fabric

8.2.2.2 Epoxy Resin System

The resin system utilized in the validation study was a conventional off-the-shelf resin comprised of a 1314A resin and 3109B hardener manufactured by Jeffco products. Both resin and hardener show a honey-like consistency and are to be mixed using a 4:1 resin to hardener ratio. Pot life of the mixed system is approximately 45 minutes at 77°F (25°C). Thus, separate batches were needed for both priming of the concrete surface and layup of the composite material.

8.3 SPECIMEN PREPARATION

Subsequent description of specimen preparation was followed for all specimens, including those of the validation program as well as specimens tested under the actual experimental program outlined in Chapter 9. To obtain a reproducible surface treatment procedure that would yield near-identical results for all further test specimens, a surface treatment schedule was established. For specimens *V-1* to *V-6*, the composite layup was applied defect-free, i.e. layup parameters were identical to those utilized on control specimens used in the subsequent study.

8.3.1 CONCRETE SPECIMENS

Concrete specimens were removed from their storage environment and prepared for subsequent surface abrasion. To obtain a surface condition representative of that found in the field, surface treatment was performed using a portable sandblasting unit, as shown in Figure 8-4. Given the need to provide a similar surface texture for all specimens, sandblasting was performed in a systematic and reproducible fashion. This included keeping a constant distance to the concrete surface of approximately 10-in (254-mm) as well as a constant duration of roughly 2 minutes per specimen. To allow for a smooth composite surface over the length of the pre-crack, only the outer parts of the specimen were treated. As such, a flatter and more uniform composite layup could be ensured. Finally, to remove any dirt or sand particles, the concrete surface was cleaned by

pressurized air. Specimens were stored in a laboratory environment to await layup of the CFRP overlay.

Despite the fact that treatment of all specimens adhered to identical procedural steps, distinct differences in surface morphology could be noted. As shown in Figure 8-5, some specimens retained significant amounts of concrete paste on the surface, while others could easily be treated to a degree such that exposure of the underlying aggregate was attained.

Figure 8-4: Surface Treatment of Concrete Specimens

8.3.2 COMPOSITE OVERLAY

The CFRP material employed in the validation study was a two-layer unidirectional laminate manufactured by hand layup. Application of the composite overlay was performed following five procedural steps, including:

- Preparation of the dry fabric
- Preparation of the concrete specimens
- Volumetric determination and mixing of the FM-1 resin system
- Surface priming
- Manual layup of fabric
- Cure

Since the dry composite fabric was supplied on rolls of 24-in (609.6-mm) width, the material had to be cut longitudinally to accommodate the width requirement of 3-in (76.2-mm). To obtain a clean edge without loss of integrity along the edges, the composite fabric was split by carefully cutting the transverse stitching, as illustrated in Figure 8-6. Due to the point-glued nature of the material, few separations of the outer fiber tows were noted. Subsequently, the composite fabric was stored in a closed container to prevent contamination from moisture and foreign material.

As the test configuration required induction of and initial pre-crack, a 0.002-in (0.05-mm) thin, 29-in (736.6-mm) long polyester film was placed at the center of each specimen, extending a distance of 14.75-in (374.7-mm) to either side of the center notch. To facilitate uniform infiltration of the composite overlay, the notch was temporarily filled using a small wood block. The film material was covered with a thin film of mold

release wax and taped to the specimen using strips of masking tape. Appearance of specimens prior to layup of the CFRP material is depicted in Figure 8-7.

Figure 8-5: Differences in Surface Appearance Following Surface Treatment

Figure 8-6: Cutting of Carbon Fabric

Figure 8-7: Polyester Film and Notch Filler

Mixing of the epoxy resin system was performed according the manufacturer's specifications. As such, the system constituents were measured using a resin-to-hardener ratio of 4 to 1, followed by mixing for at least three minutes.
Prior to layup, the concrete surface was primed using a separate batch of the Jeffco epoxy resin system. Using mohair rollers of 3-in (76.2-mm) width, as shown in Figure 8-7, resin was applied until each section of the bond area was saturated to a satisfactory degree (Figure 8-9). Particular care was taken not to form overly saturated areas, as this would compromise consistency and reproducibility of the priming process. To attain sufficient tackiness, the resin was allowed to partially set for about 10 to 15 minutes. However, it should be noted that the rationale of partial primer cure is predominantly due to the otherwise excessive sagging of wet fabric in overhead regions.

In preparation of the layup process, a total of 12 layers of dry fabric were removed from the storage box and placed in close vicinity of the primed concrete specimens. Also, due to the limited pot-life of the resin system, a second batch was mixed to allow at least 45 minutes of adequate workability. To provide good infiltration of the first layer, the primed surface was again saturated with one coat of resin, after which the first fabric layer was placed. A second coat of resin was applied on top of the fabric and a steel roller was used to further facilitate infiltration. This process was repeated for the second layer of fabric. Rolling the two-layer composite laminate in opposite directions, beginning from the center of the specimens, completed the layup sequence. As such, straightness of the laminate could be ensured. The finalized layup sequence is shown in Figure 8-10. Prior to testing, specimens were allowed to cure for one week.
Upon complete cure of the resin system, two 20-mm electric resistance strain gauges (ERSG's) were attached to the center of the composite strip, equidistant from the loading rod. Given the previous assumption of equal strain on both sides of the composite membrane, even under conditions of unsymmetrical peeling, these gauges were used to monitor the actual strain distribution during testing. To provide perfect bond between the gauges and host material, the composite surface was slightly abraded using gp size#80 sandpaper. Subsequently, the surface was wiped with MEK to remove any residue. Gauges were attached using the two-component cement glue X-60 provided by HBM Wägetechnik GmbH. The finished specimens, including properly attached ERSG's, are shown in Figure 8-11.

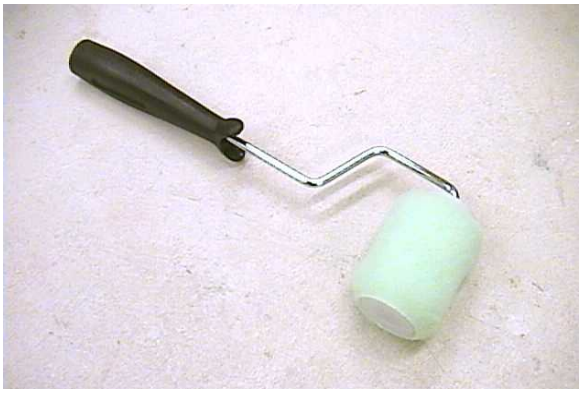

Figure 8-8: Mohair Roller used for Priming and Fabric Infiltration

Figure 8-9: Adequately Primed Concrete Surface

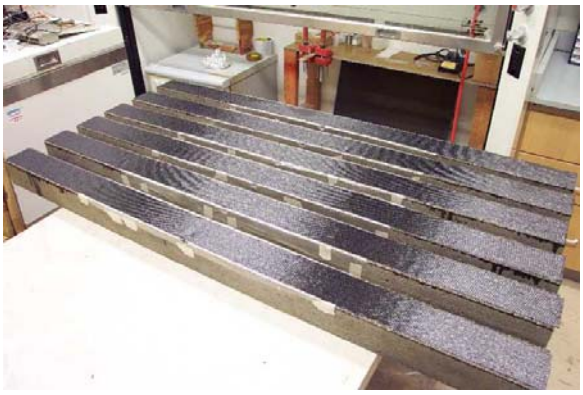

Figure 8-10: Finalized Layup Sequence

Figure 8-11: Placement of Electrical Resistance Strain Gauges

8.4 TESTING PROCEDURE

To ensure exact measurement of crack propagation using the video monitoring system, paper rulers were attached to all four sides of the specimens. Having a total length of 240-mm, these rulers extended from the end of the polyester pre-crack (zero-mark) to the inner edge of the steel clamps (240-mm mark). Also, to enhance visibility of the crack

front, the composite/concrete interface was painted using a brittle, white fluid (compare Figure 8-11). Hence, during peeling, a clearer video image could be obtained.
Specimens were placed in the test fixture and clamped down at either end, using the two steel brackets. Herein, the prisms were located such that both ends of the 240-mm marks would align with the inner edges of the two steel clamps. Zero cross-head displacement, i.e. the location where no loading force was induced into the composite membrane, was found by fine-tuning of vertical cross-head displacement until the bar would move freely in the center notch, while barely touching the composite membrane.

For all subsequent testing, including the pre-cracking and cracking stage, vertical cross-head velocity was set to 0.04-in/min (1.0-mm/min). This test velocity was chosen based on findings of reference [21]. In addition, initial calibration tests had shown that, using above cross-head velocity, complete peeling of the CFRP sheet required a total vertical displacement of the loading rod of approximately 1.2 to 1.9-in (30 to 50-mm). Hence, to utilize the full storage capacity of the video acquisition system, frame rate was set to 0.25 fps, i.e. one image was recorded every 4 seconds. Also, due to stability requirements (Section 3.3), loading was performed in displacement control.

During cyclic testing, the loading rod was first moved from its neutral position to a displacement level at which cracking initiated. To acquire data from at least four successive cycles, loading was continued until approximately one-fourth of the total bonded distance was peeled off. Then, loading was terminated, followed by immediate reversal of cross-head movement, again at a rate of 1-mm/min. The unloading process continued until the loading rod had returned to its original position, followed by manual recording of crack propagation length at all four crack fronts. This procedure was repeated for all subsequent cycles.

For continuously tested specimens, loading was initiated at zero displacement of the loading rod and commenced until cracking had occurred over the full length of the specimen. Upon first signs of crack initiation, video acquisition was activated and continued until the entire composite membrane has separated from the substrate. Then, recording was terminated followed by unloading of the CFRP strip.
Since evaluation of fracture toughness based on Equation (7.11) demands knowledge of thickness, width, as well as tensile modulus of the composite, the CFRP membranes were subject to further tests. Herein, the remaining regions of bonded material were peeled off manually and average peel width, B, was determined by measuring the peeled portion at three equally spaced locations. To evaluate the remaining parameters, tensile test coupons were cut from material of the initially unbonded region, as illustrated in Figure 8-12. Following ASTM D3039, a minimum of three coupons per specimen was tested. Detailed results of this analysis are provided in Appendix C.
As was expected, none of the six specimens experienced peel-off in a perfectly symmetrical manner. In most instances, the peeling process was initiated by one-sided cracking and continued ion such manner until a significantly higher load level was reached. Also, opposite sides of a crack front did not experience equal peel lengths, i.e. the crack front was not perpendicular to the direction of propagation, as illustrated in Figure 8-13.

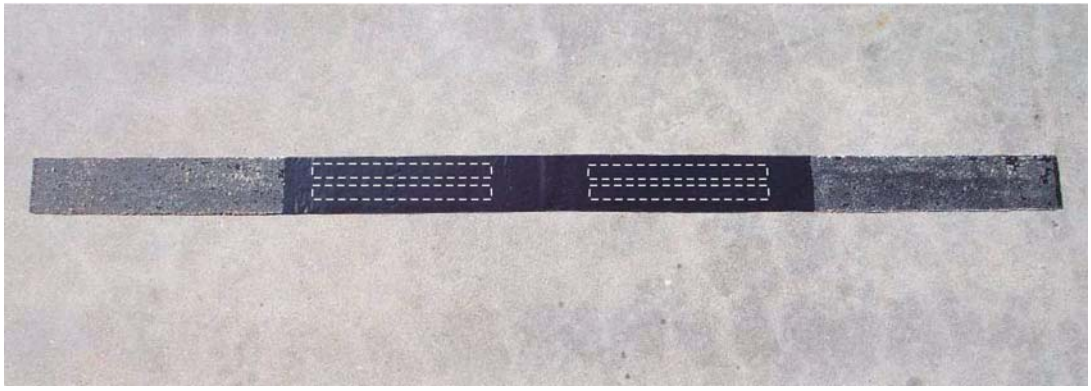

Figure 8-12: Material Origin for Tensile Test Coupons

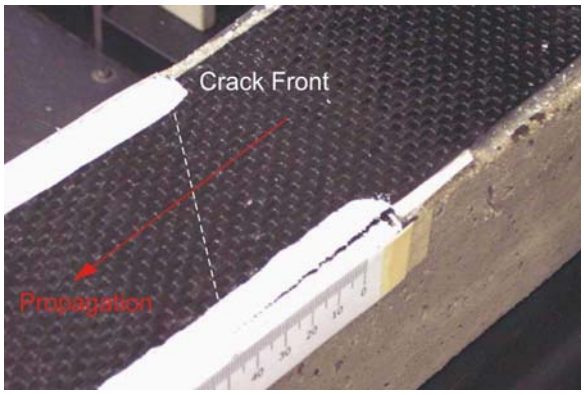

Figure 8-13: Angled Crack Propagation

8.5 TEST RESULTS

8.5.1 LOAD-DISPLACEMENT GRAPHS

Load-displacement graphs of specimens *V-1* to *V-3* are shown in Figure 8-14 to 8.15. As may be seen, loading and unloading curves of specimens *V-2* and *V-3* follow nearly identical paths, indicating a maximum strain level at which no inelastic behavior is noted. The notable differences between loading and unloading paths for specimen *V-1* may be attributed to the fact that certain parts of the test were not recorded; hence only three cycles are shown. Also, recalibration of the load cell was erroneously performed during the first test, which explains the higher load levels during the loading phase of the third cycle.

Also, during the final test cycle of specimens *V-2* and *V-3*, the load-displacement graph shows a peak load during which little or no further peeling could be observed. These peaks are indicative of the fact that one side of the specimen had peeled off completely while peeling commenced on the opposite side.

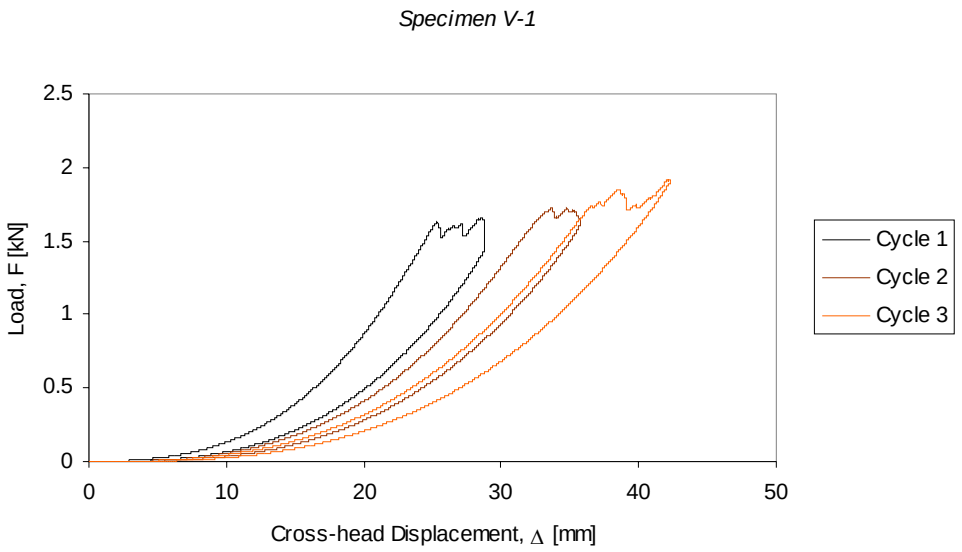

Figure 8-14: Load-Displacement Graph for Specimen V-1

Figure 8-15: Load-Displacement Graph for Specimen V-2

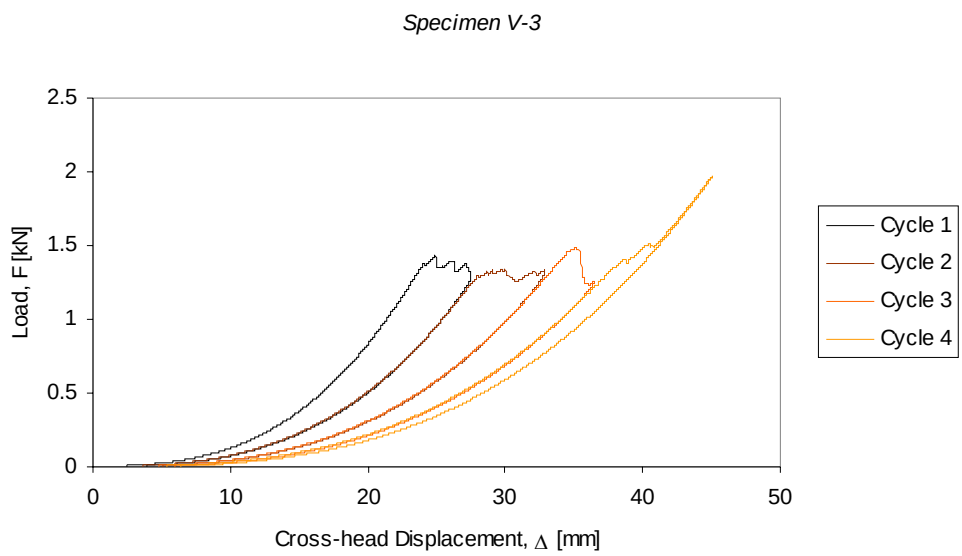

Figure 8-16: Load-Displacement Graph for Specimen V-3

For comparison, load-displacement graphs for specimens *V-4* to *V-6* are depicted in Figure 8-17. As may be noted, a relatively large variation in peel load exists, i.e. resistance of the material to fracture varies along the specimen surface. This may be attributed to the significant variation in surface morphology and inhomogeneous nature of the concrete in general.

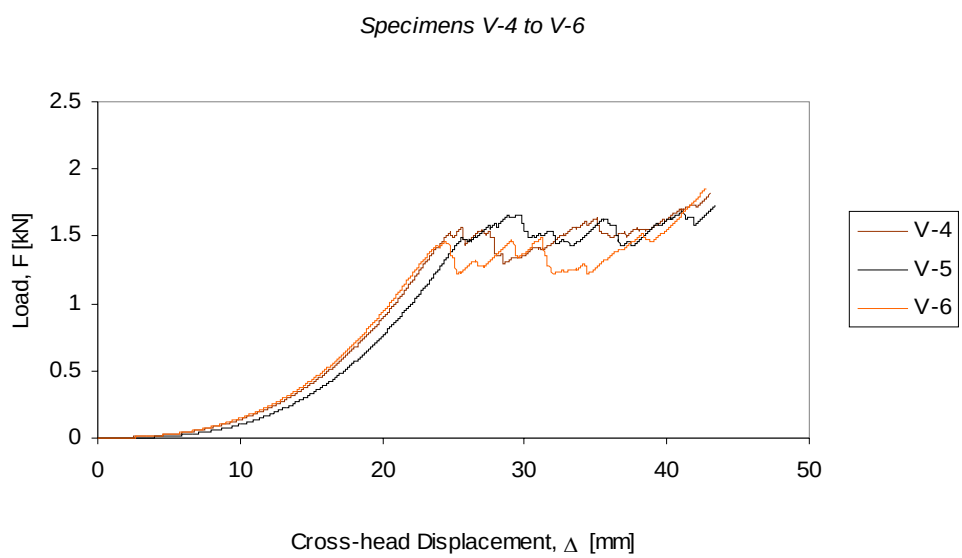

Figure 8-17: Load-Displacement Graph for Specimens V-4 to V-6

8.5.2 Strain Variation Model

The strain variation model proposes that even under unsymmetrical peel lengths on both sides of the loading rod, strain along the CFRP membrane may be considered uniform. Hence, the strip is assumed to slide over the pulling rod to adjust for variation of strain

that would naturally occur due to differences in crack length on two opposite sides. To graphically confirm the previous assumption, two different strain variations are hereby defined as follows:

$$\Delta\varepsilon = \varepsilon_2 - \varepsilon_1 \tag{8.1}$$

and

$$\Delta\delta = \delta_2 - \delta_1 \tag{8.2}$$

where $\Delta\varepsilon$ is the experimental strain variation and ε_2 and ε_1 represent the experimentally measured strain on opposite sides of the loading rod. More specifically, ε_1 is the strain measured at camera locations 1 and 2, while ε_2 represents the strain measured at camera locations 3 and 4 (compare Figure 6-2). Similarly, $\Delta\delta$ represents the theoretical strain variation, caused by a CFRP membrane that is restricted from slipping over the point of load introduction, while δ_2 and δ_1 are the theoretical strains calculated from vertical displacement and peel distance on both sides of the specimen and are defined as:

$$\delta_2 = \frac{\sqrt{\Delta^2 + a_{34}{}^2}}{a_{34}} - 1 \tag{8.3}$$

and

$$\delta_1 = \frac{\sqrt{\Delta^2 + a_{12}{}^2}}{a_{12}} - 1\,. \tag{8.4}$$

Herein, a_{34} and a_{12} are the average peel distance at camera locations 3 and 4 and camera locations 1 and 2, respectively.

Results of experimental and theoretical membrane strain are shown in Figure 8-18 to 8-20. As may be noted, experimental strain variation, $\Delta\varepsilon$, remains nearly constant for all three specimens, while the theoretical variation, $\Delta\delta$, undergoes significant fluctuation, depending on differences in peel length between the two opposing sides of the each specimen. Hence, it may be concluded that strain remains nearly constant even in situations of unsymmetrical peeling, thus confirming applicability of Equations (7.9) through (7.11).

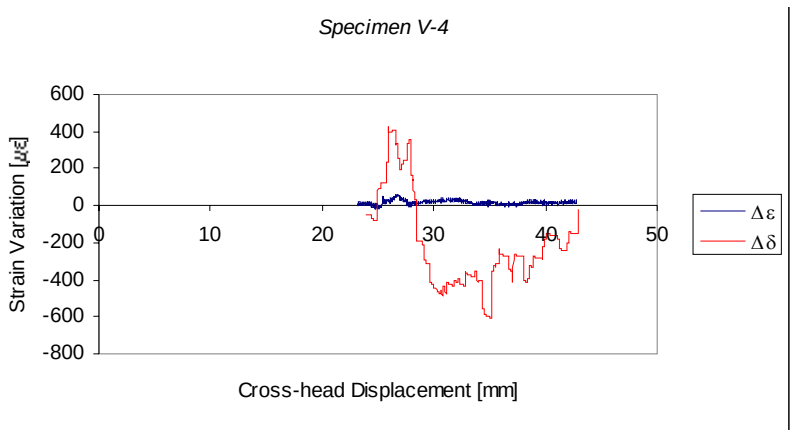

Figure 8-18: Strain Variation of Specimen V-4

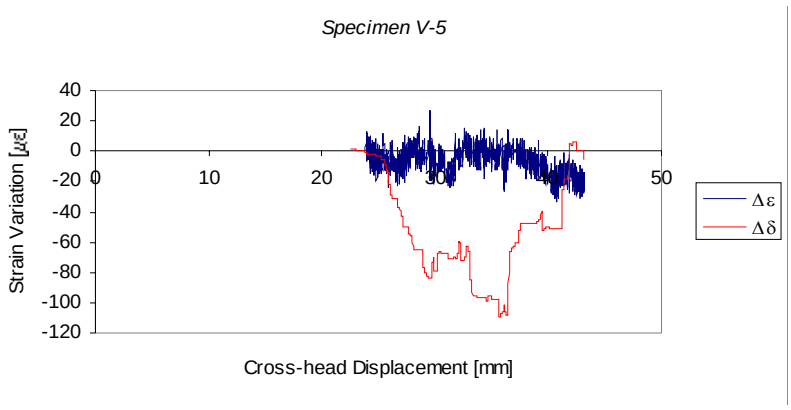

Figure 8-19: Strain Variation of Specimen V-5

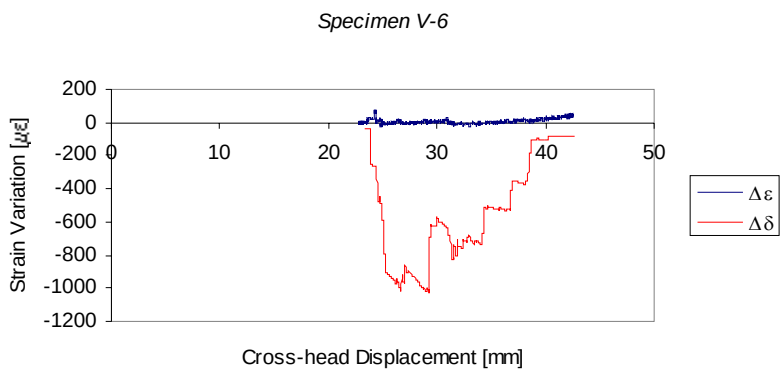

Figure 8-20: Strain Variation of Specimen V-6

8.5.3 Fracture Energy Release Rate

To calculate values of fracture toughness for specimens *V-1* to *V-3*, areas encircled by the loading and unloading curves in Figure 8-14 to 8.15 were evaluated for each individual cycle. Subsequently, given the measured peel distances, Equation (3.13) was evaluated. Graphical results of this analysis are given in Figure 8-21. As may be observed, average fracture toughness of specimen *V-1* and *V-2* are nearly identical, while that of specimen

V-3 varies significantly. However, scatter of test *V-3* is extremely low, which indicates profound differences in crack resistance for this specimen. Given the fact that surface differences were noticed prior to application of the composite overlay, it may be assumed that this discrepancy is predominantly due to variation in surface morphology. As such, specimen *V-3* may have retained more of the weak cement paste on its surface. However, as surface conditions were not recorded prior to testing, this assumption could not yet be confirmed.

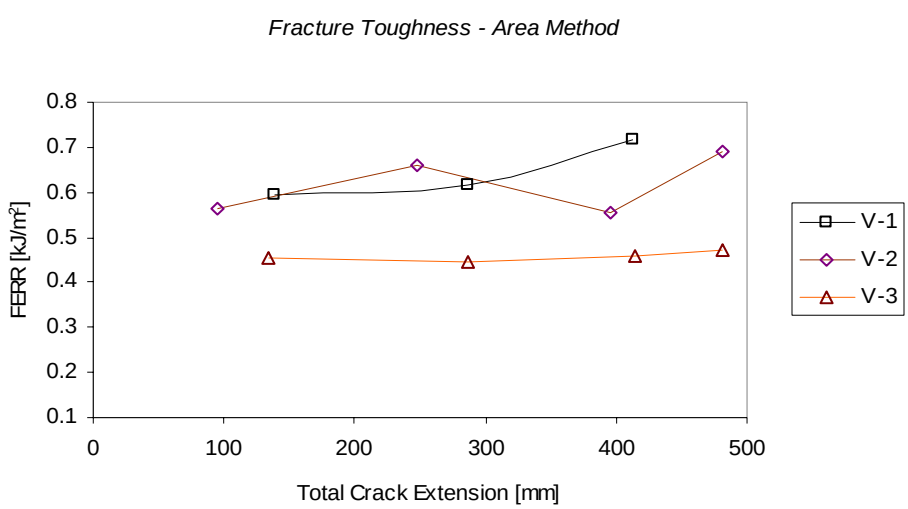

Figure 8-21: Fracture Toughness of Specimens V-1 to V-3

For evaluation of fracture toughness for specimens *V-4* to *V-6*, data of crack propagation was manually extracted from the recorded video sequences. Using an Excel spreadsheet, load-displacement data was combined with data extracted from the video acquisition system. Herein, parameters x, α, and Δ were determined for each loading point. Material properties B, t and E_{11} were determined as described in Section 8.4.

Given the inhomogeneous concrete surface, peeling did not occur in a perfectly continuous fashion. Instead, variation in material resistance along the specimen surface periodically arrested the cracking process. Once the strain energy was large enough to overcome crack resistance of a specific location, peeling commenced. It should be noted that severity of this phenomenon varied significantly along the length of specimens.

As fracture toughness is defined by the rate of change of potential energy with respect to crack extension [14], points of constant crack length were omitted from the analysis. Hence, points of fracture toughness, shown in Figure 8-22, represent a change in potential energy of the CFRP membrane with respect to an individual crack extension at that specific instance. A numerical comparison of average energy release rates for all six specimens is given in Table 8-1.

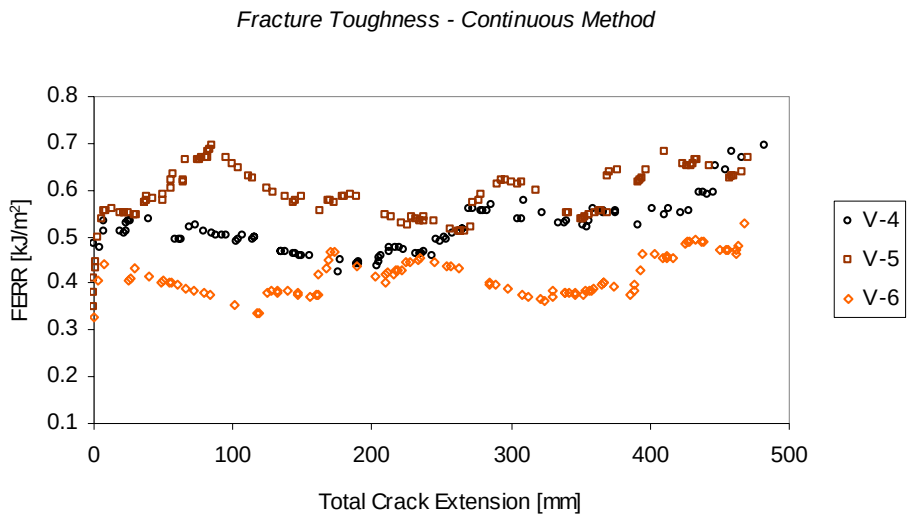

Figure 8-22: Fracture Toughness of Specimens V-4 to V-6

Table 8-1: Comparison of Fracture Toughness for Specimens V-1 to V-6

SPECIMEN #	G_{AREA} [kJ/m^2]	SPECIMEN #	$G_{CONTINUOUS}$ [kJ/m^2]
V-1	0.641	*V-4*	0.516
V-2	0.618	*V-5*	0.583
V-3	0.457	*V-6*	0.415

It may be seen that results obtained for G_{Area} and $G_{Continuous}$ are in relatively good agreement. Nonetheless, a drawback of the previous validation methodology is given by the fact that results for both area method and continuous method were obtained from different specimens. It would thus be favorable to obtain fracture energy release rate based on the two approaches using identical specimens. Currently, thus is restricted by the fact that continuously tested specimens are lacking cyclic data, i.e. curves that depict the loading and unloading curves for various peel lengths, and that continuous monitoring of crack propagation was not performed on specimens tested in a cyclic manner. To overcome this deficiency, an alternative approach was followed, herein defined as *pseudo area method*.

As defined earlier, an analytical load-displacement relationship can be obtained using Equation (7.9). As shown in Figure 8-23 to 8-25, a total of three to four theoretical loading/unloading curves were fit to the existing (experimental) and analytical load-displacement plots of specimens *V-4* to *V-6*. Herein, the loading/unloading curves were calculated using Equation (7.9) and crack length was supposed to remain constant from the onset of unloading to the point where the previous deflection was exceeded in the subsequent loading cycle. As may be seen, the overall shape of the analytical loading curve agrees well with that of the experimental load-displacement plot. Nonetheless, on specimens *V-4* and *V-5*, Equation (7.9) yields loads in excess of those obtained from experiments. This difference may generally be attributed to variations in the

experimentally determined tensile modulus, E_{11}, of the composite membrane. Aspects of determining material properties are further elucidated in Appendix C.

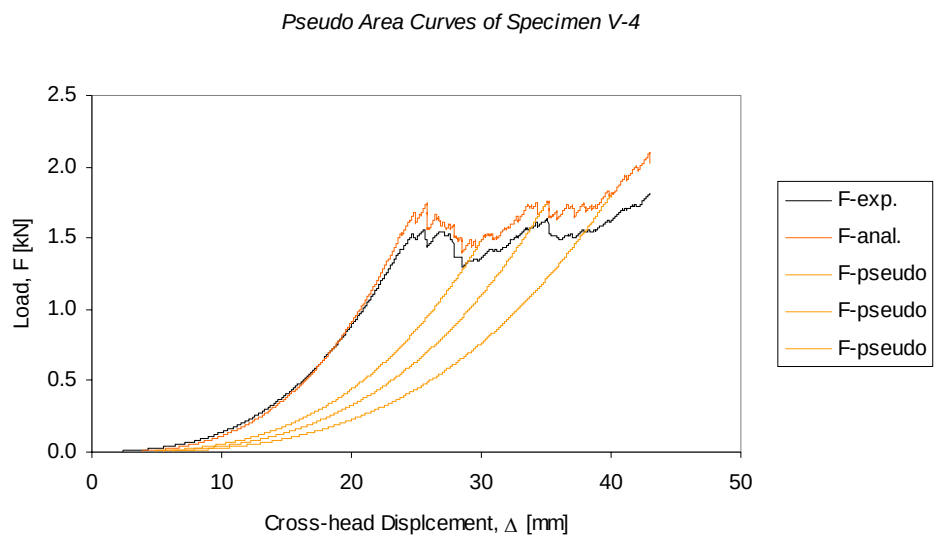

Figure 8-23: Pseudo Area Curves of Specimen V-4

Compared to analysis of the area method, the pseudo area approach followed a similar rationale, i.e. the area encircled by the analytical load-displacement curve and pseudo loading/unloading curves was divided by the incremental crack growth during each cycle. Figure 8-26 to 8-28 illustrate that results of the pseudo area- and continuous method are in excellent agreement. Unlike the previous comparison, results are extracted from identical specimens such that differences in substrate morphology, leading to variations in fracture resistance, are no longer relevant.

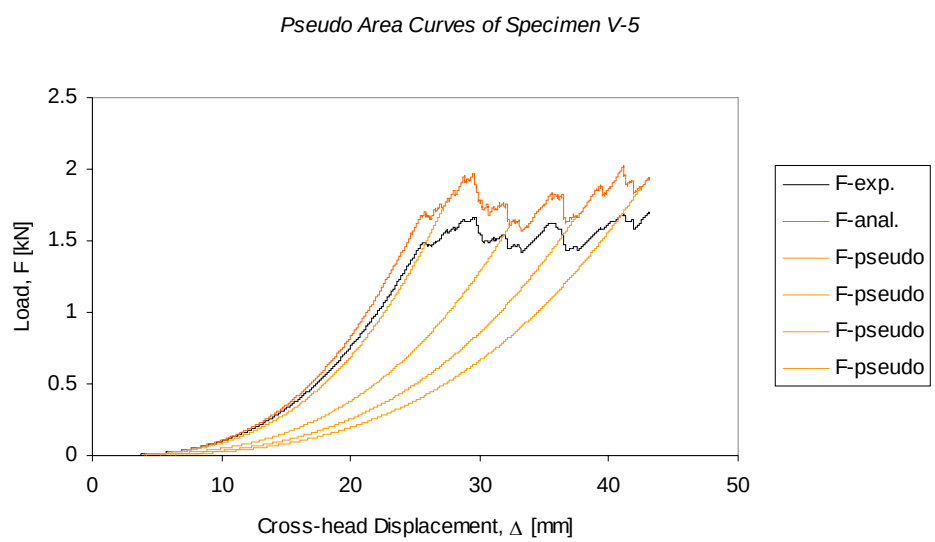

Figure 8-24: Pseudo Area Curves of Specimen V-5

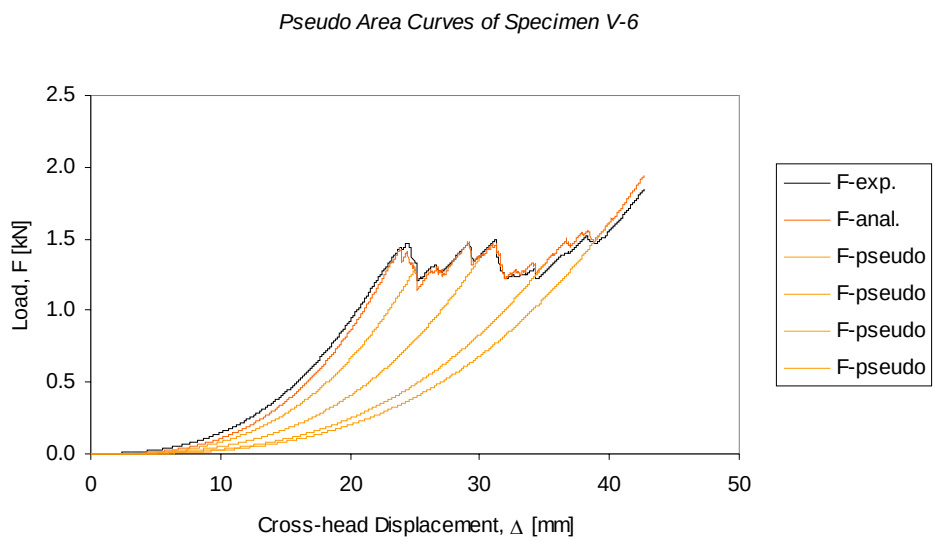

Figure 8-25: Pseudo Area Curves of Specimen V-6

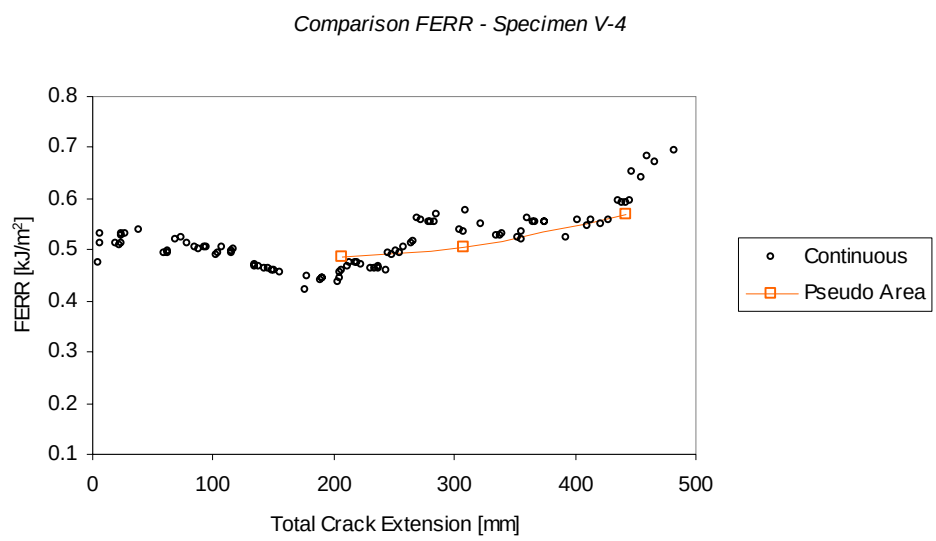

Figure 8-26: Comparison of Fracture Toughness between Continuous and Pseudo Area Method – Specimen V-4

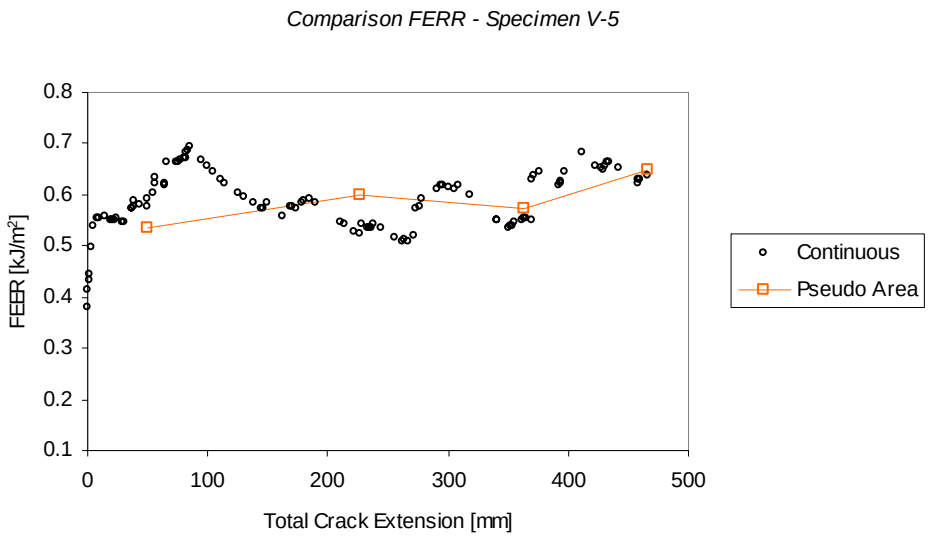

Figure 8-27: Comparison of Fracture Toughness between Continuous and Pseudo Area Method – Specimen V-5

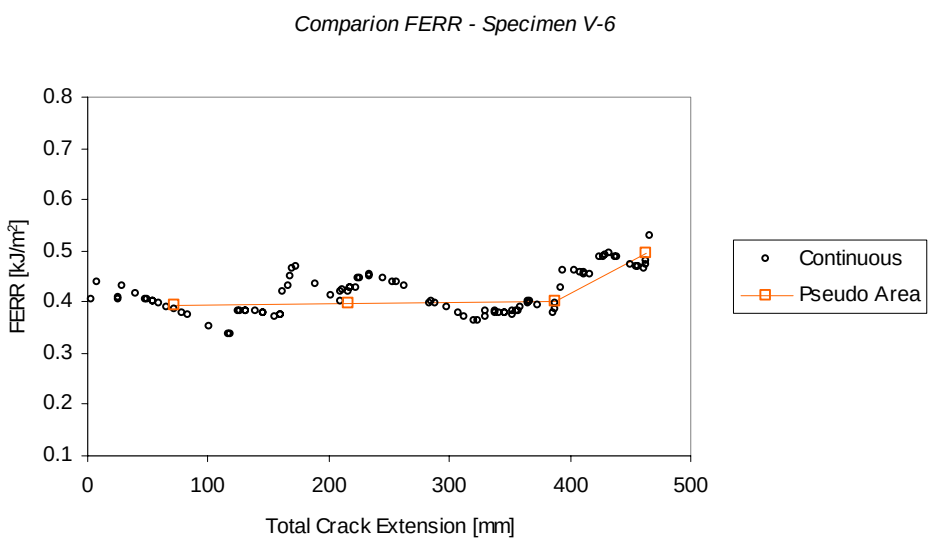

Figure 8-28: Comparison of Fracture Toughness between Continuous and Pseudo Area Method – Specimen V-6

8.6 PRELIMINARY CONCLUSIONS

Several preliminary conclusions can be drawn from the results presented in this Chapter. Firstly, as shown in Section 8.5.2, the assumption of equal strain along the CFRP membrane could be confirmed, which was named a precondition for applicability of Equations (7.9) to (7.11). Moreover, a method of calculating fracture toughness alternative to that provided by the well-known area method has been established and proven experimentally, using two different approaches. Herein, two sets of specimens were evaluated one using the continuous method while the other was tested via the area approach. While results from these analyses were indicative of good agreement between

the two approaches, a second methodology, defined as pseudo area method, was utilized to provide two sets of results from a single specimen. Due to the excellent agreement among data sets, Equation (7.11) has proven applicable for further evaluation of fracture energy release rate using a continuous testing methodology. As such, time intensive cycling procedures, typically linked to the area method, can be averted.

Secondly, given the similarity of experimental and analytical load-displacement graphs depicted in Figure 8-23 to 8-25, Equation (7.9) appears to adequately represent the relationship between internal and external forces acting on the CFRP strip. Nonetheless, inadequate analysis of CFRP test coupons remains a possible factor for discrepancies in Figure 8-23 to 8-25. Measurement and testing of coupons must therefore be performed with great care.
Further, it can be shown that strain in the CFRP material remains at levels well below that of possible fiber fracture. Thus, test coupons are expected to reflect the actual material behavior, even if they are obtained from a material that has previously been subjected to substantial levels of loading.

Finally, it was shown that the resistance curve of an abraded concrete surface is significantly different from that of a smooth, homogeneous material, such as steel or aluminum. Hence, peel tests performed on concrete are typically subject to a more abrupt release of energy. Also, crack arrest is likely to occur at locations that show a high degree of surface roughness. As shown in Appendix B, significant variations in crack resistance may lead to locally unstable behavior, even for systems that are otherwise stable.

9 EXPERIMENTAL PROGRAM

9.1 INTRODUCTION

Hitherto, an analytical model for evaluation of fracture toughness on CFRP-rehabilitated concrete specimens has been presented and validated, based on comparison between continuous- and cyclic peel methodologies. As shown, results from both approaches are in good agreement and thus allow use of continuous peeling for all further tests.

While the previous discussion has focused on introduction and validation of the proposed test method, the actual defect criticality study will be presented in the following. Herein, a selection of all defects addressed in this study was given in [2] and further details will be presented in corresponding parts of this report. These entail specific details about specimen preparation, layup of materials as well as initiation of defects.

Conditioned by the varying complexity of defects, i.e. certain defects required more extensive preparation efforts than others, testing was not performed in an order identical to that given in Table 9-1. Also, to date, only a limited selection of defects has been addressed in the investigation. These defects are highlighted in Table 9-1.

9.2 DEFECTS AND MODELING PARAMETERS

A list of all defects, including their initiating stage, system designation and defect number, is presented in Table 9-1. Similar to previous discussion, defects are categorized according to their initiating stage during rehabilitation. Given the need to establish a baseline of fracture toughness based on a sound, i.e. defect-free, specimen, a category for testing of control specimens for both wet layup and prefabricated strips has been included. They are herein denoted as [C-W] for wet layup and [C-P] for prefabricated materials. For these specimens, an identical preparation and layup procedure is strictly followed to minimize the effect of variations during specimen fabrication on measurement of fracture toughness. Detailed information on procedural steps for fabrication of control specimens are provided in a later Section of this report.

Due to the fact that defects may occur at various levels of intensity, a number of possible variations were further considered. From experience gained in the field, the most common or likely occurrence of a particular defect was recorded and implemented into the test protocol, which is given in Table 9-2. As may be noted, most defects were studied using two different levels of severity, while some parameters appeared to contain such large variation that only a single level was chosen. Detailed information on procedural steps used to induce such defects is given in the corresponding Sections.

To obtain representative results, a total of three test specimens per defect parameter were adopted. While this resulted in a fairly large number of test specimens (a total of 144, including control specimens for both strengthening systems), assessment of criticality from fewer specimens appeared unsuitable. As results of Chapter 8 had shown, identical surface treatment did generally not result in similar surface textures for all specimens. Hence, to adjust for this given error, the number of test specimens had to be increased.

Table 9-1: Experimental Program (Designation of Defects)

STAGE	SYSTEM TYPE	DEFECT #	DESIGNATION
CONTROL	WET LAYUP	[C-W]	Control beams for wet layup
	PREFABRICATES	[C-P]	Control beams for prefabricates
RAW AND CONSTITUENT MATERIALS	WET LAYUP	[1]	Resin moisture uptake
		[2]	Wavy fibers
		[3]	Damage to free edges
SITE PREPARATION	WET LAYUP	[4]	Substrate moisture
		[5]	Incorrect stoichiometry
		[6]	Inadequate primer
		[7]	Moisture on primer
		[8]	Prolonged primer cure
	PREFABRICATES	[9]	Substrate moisture
		[10]	Moisture on primer
		[11]	Prolonged primer cure
FIELD INSTALLATION	WET LAYUP	[12]	Concrete cavities
		[13]	Voids/disbonds at bondline
		[14]	Voids/delamination in composite
		[15]	Resin rich/starved regions
	PREFABRICATES	[16]	Voids at concrete/adhesive interface
		[17]	Debond at adhesive/prefabricates interface
		[18]	Excessive bondline thickness
SERVICE	WET LAYUP	[19]	Penetration of moisture
		[20]	Heat damage
		[21]	Impact damage
	PREFABRICATES	[22]	Penetration of moisture
		[23]	Heat damage
		[24]	Impact damage

Note: see Table 9-2 for modeling parameters and specimen quantities

Table 9-2: Experimental Program (Model Parameters)

DEFECT #	MODEL PARAMETERS	AMOUNT	# OF SPECIMENS	TOTAL # OF SPECIMENS
[C-W]	Wet layup under controlled environment	-	6	6
[C-P]	Adhesive bonding of prefabricates under controlled environment	-	6	6
[1]	Exposure in humidity chamber	77°F-80%RH 77°F-80%RH	3 3	6
[2]	Introduction of fiber waviness during layup	-	3	3
[3]	Remove stitching from fabric	½" into fabric 1" into fabric	3 3	6
[4]	Exposure in humidity chamber	77°F-80%RH 77°F-80%RH	3 3	6
[5]	Incorrect resin/hardener ratios	-10% RH -25% RH	3 3	6
[6]	Rich and poor priming	No priming 200% priming	3 3	6
[7]	Exposure of primed specimen to moist environment	-	3	3
[8]	Application of layup subsequent to complete cure of primer	As is Roughened	3 3	6
[9]	Exposure in humidity chamber	77°F-80%RH 77°F-80%RH	3 3	6
[10]	Exposure of primed specimen to moist environment	-	3	3
[11]	Application of layup subsequent to complete cure of primer	As is Roughened	3 3	6
[12]	Drilled cavities in concrete substrate – ¼-in ∅	2.5% of area 5% of area	3 3	6
[13]	Teflon plates at bondline, round shape – ½-in ∅	10% of area 25% of area	3 3	6
[14]	Teflon plates between individual composite layers – ½-in ∅	10% of area 25% of area	3 3	6
[15]	Altering amounts of resin utilized during layer infiltration	-50% +50%	3 3	6
[16]	Teflon plates between individual composite layers – ½-in ∅	10% of area 25% of area	3 3	6
[17]	Strips bonded to wrong side	-	3	3
[18]	Altered bondline thickness	5-mm 7-mm	3 3	6
[19]	Exposure to humid/wet environment	1 day 1 week	3 3	6
[20]	Exposure to high temperatures (heat gun)	75% T_g (1hr) 95% T_g (1hr)	3 3	6
[21]	Localized high-velocity/low-mass impact via impact hammer	5-J 10-J	3 3	6
[22]	Exposure to humid/wet environment	1 day 1 week	3 3	6
[23]	Exposure to high temperatures (heat gun)	75% T_g (1hr) 95% T_g (1hr)	3 3	6
[24]	Localized high-velocity/low-mass impact via impact hammer	5-J 10-J	3 3	6

9.3 CONSTITUENT MATERIALS

9.3.1 CONCRETE SPECIMENS

Specimens utilized for the criticality study are identical to those described in Section 8.2.1. However, based on findings in Chapter 8, digital images of the surface morphology were taken at four equally spaced locations along the specimen surface following surface abrasion. These would later aid in assessing the effect of differences in surface conditions on fracture toughness. As previously discussed, significant variations in surface appearance were noted among specimens, despite the fact that treatment adhered to identical preparation procedures.

9.3.2 CFRP MATERIALS

Given the fact that two separate composite systems are used in the present study, namely wet layup of dry fabric and adhesive bonding of prefabricated strips, the constituent materials of both systems must be briefly discussed. To utilize constituents representative of those used in the field, all CFRP materials were obtained from Structural Composite Construction Incorporated (SCCI) of Montclair, CA.

9.3.2.1 Dry Fabric

The dry carbon fabric use in the criticality study was identical to that described in Section 8.2.2.1. For field-use, the material is typically supplied on rolls of 6-in (152.4-mm) width. To minimize the chance of deterioration, i.e. fiber pullout or fuzzing, along the sides, the material contains double stitching on both edges. Although the fabric used for the fracture study was cut from a wider roll, integrity could largely be preserved.

9.3.2.2 Prefabricated Strips

The SCCI CS-02 carbon fiber strip (Figure 9-2) was employed to study the effect of defects on adhesively bonded composite material. It is a thin, highly uniform material and specifically designed for structural adhesive bonding. Further, it is compatible with most resin systems and shows a minimum glass transition temperature of 230°F (110°C). Its physical properties are given in Table 9-3. As such, one side of the material is pre-treated at the factory to ensure adequate surface roughness. Hence, only one side of the material is marked “bondable” and adhesion of the wrong side will result in inferior performance.

9.3.2.3 Epoxy Resin System

A hi-modulus fiber matrix 1 (FM-1) epoxy resin system was used on the wet layup specimens. It is a low viscosity epoxy for saturating carbon and glass fibers for structural repairs and is formed by combining a viscous part A (resin) and a liquid part B (hardener), as shown in Figure 9-1. Classified as a 100% solids, solvent-free, two-component moisture insensitive epoxy system, it employs an easy mix ratio of 2 parts resin to 1 part hardener by volume, leaving little room for mixing errors due to incorrect mix fractions. Further, the resin provides a relatively long pot life with rapid strength development. Unlike the Jeffco resin system that was used in the validation program, the FM-1 resin system did not require two separate batches for priming and layup. Finally,

the FM-1 resin system allows low temperature cure as low as 40°F (4°C), making it excellent for in-situ applications. Physical properties are given in Table 9-4.

Figure 9-1: Two-component FM-1 Resin System

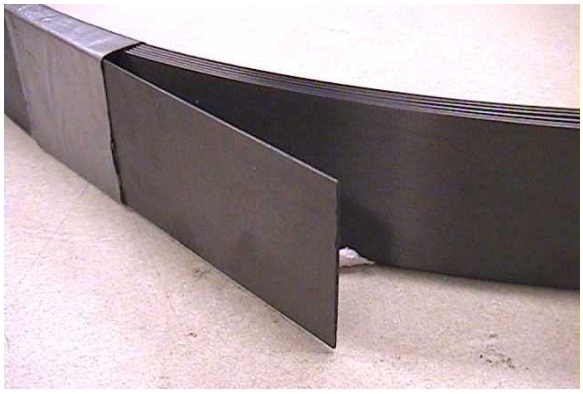

Figure 9-2: CS-02 Pultruded Carbon Strips

Table 9-3: Physical Properties of Reinforcing Material

MATERIAL PROPERTY	T-700 CARBON FIBER	CS-02 STRIPS
Nominal Width	24 in	2 in
Nominal Thickness	~ 0.014 in	0.05 in
Tow Count	12,000	-
Tensile Strength	751 ksi	305 ksi
Tensile Modulus	33.7 msi	20.5 msi
Ultimate Strain	2.2 %	1.2 %

9.3.2.4 Bonder Gel

Similar to the FM-1 resin system, the SCCI bonder gel BG-02 is a 100% solids, solvent-free, two-component moisture insensitive epoxy structural adhesive system. It has a unique hi-modulus of elasticity and employs a gel-like consistency, designed to bond mating or non-mating surfaces, where the glue-line thickness will not exceed 1/8-in (3.2-mm) and is further designed to structurally bond grip systems, grout anchor bolts or seal cracks. As for the FM-1 resin system, a mix ratio of 1 to 1 by volume simplifies the proper in-situ preparation of the bonder. Moreover, it is fast setting and allows for cure at low temperatures as low as 40°F (4°C). Physical properties of the BG-02 system are given in Table 9-4.

9.4 SPECIMEN PREPARATION

Preparation of specimens was largely identical to the procedure outlined in Section 8.3. However, specific parameters were altered for specimens that were to contain artificially induced defects. To attain a uniform distribution of constituents, all resin mixing was performed using a rotary drill head, as shown in Figure 9-3. It was noted that a honey-like viscosity was reached after approximately one minute of mixing.

Table 9-4: Physical Properties of Matrix/Adhesive Material

MATERIAL PROPERTY	FM-1 RESIN SYSTEM	BG-02 BINDER GEL
Viscosity (mixed)	700-900 cps	Gel
Pot Life	~ 60 min	~ 30 min
Tack-Free Time (75°F)	4.5 hrs	2-4 hrs
Glass Transition Temperature T_g [1]	>135°F (57°C)	-
Heat Deflection Temperature [2]	-	124°F (51°C)
14-day Tensile Strength	6000 psi	7200 psi
Tensile Modulus	-	4.4×10^5 psi
Elongation at Break	2-4 %	-

[1] *Measured at 90°F (32°C)*
[2] *Per ASTM-D-648*

9.4.1 CONTROL SPECIMENS – WET LAYUP

To obtain a baseline value of fracture toughness, several ideally defect-free specimens were fabricated. Preparation of the wet layup control specimens included proper surface abrasion and subsequent cleaning by pressurized air. Similar to Section 8.3.2, a pre-crack of 14.75-in (374.7-mm), extending to both sides of the center notch, was induced using a thin polyester film. To prevent out-of-plane waviness, the notch was temporarily filled using wooden blocks. After taping of the pre-crack film, the surface was adequately primed, i.e. two coats of resin were applied to the dry concrete surface and allowed to cure for about 10 to 15 minutes. During this time, the dry composite fabric was inspected

for any anomalies such as fiber fuzzing, pullout, or surface contamination due to dust or other foreign materials.

Using mohair rollers, the primed surface was again saturated to supply resin to the bottom of the subsequently placed dry fabric. The fabric was placed onto the wet concrete and a second coat of resin was applied, followed by successive rolling that was initiated at the center of the specimen and progressed towards either end. After a second layer had been placed following an identical procedure, the specimen was allowed to cure.

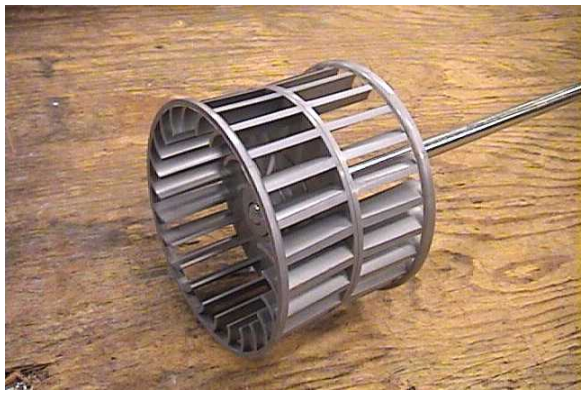

Figure 9-3: Rotary Mix-head

9.4.2 DEFECT [3]: DAMAGE TO FREE EDGES

Damage of the transverse stitching, which may result in deterioration of the free edge of the dry composite fabric, has already been encountered numerous times during field installation. The likely result of damaged or missing transverse stitching is separation of individual tows in combination with a flattening effect as fibers are no longer restricted against transverse movement. This may lead to resin-rich areas and local waviness. While transverse stitching does not affect tensile properties of the laminate, resin-richness is likely to affect bond as well as interlaminar properties of the laminate.

The parameters assigned for this defect are based on actual damage inspected in the field. As shown in Figure 9-4, transverse stitching was damaged over a width of approximately ½ to 1-in (12.7 to 25.4-mm) propagating into a single side of the material. Since it is highly unlikely that this defect occurs on two opposite sides simultaneously, only the one-sided form of this anomaly was studied.

As this defect only affects the laminate properties, preparation of the concrete specimen remained unaltered. Hence, the surface was abraded, cleaned and primed according to previously described procedures. For modeling, the transverse stitching of the T-700 fabric was removed using a scalpel cutter. Herein, the stitching was cut in-between every single tow. Further, to investigate the most severe form of this anomaly, removal of transverse stitching was continued throughout the entire bonded length of the laminate, as shown in Figure 9-5. Subsequently, the material was laid up in the normal fashion.

During layup, several characteristics of this defect could be noted. Firstly, the individual fiber tows tended to overlap, which was a phenomenon that was particularly pronounced on fabric containing the 1-in deep anomaly. Secondly, due to the loss of bond to adjacent

fibers, tow twisting was noted, resulting in a more difficult layup procedure. Particular care was necessary to obtain a flat appearance, as tows tended to twist even after they were saturated with the resin system. Thus, a more intensive rolling procedure was required. Finally, fiber gaps tended to open up during the rolling process. As depicted in Figure 9-6, these gaps facilitated the development of resin-rich regions between adjacent tows. Ultimately, the layup tended to be noticeably wider that that of the control specimens.

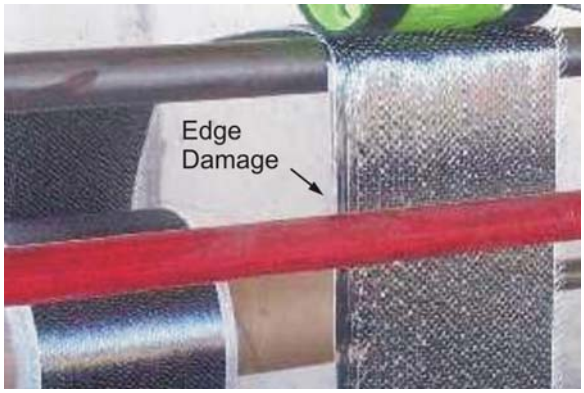

Figure 9-4: Damage to Transverse Stitching in Field Installation

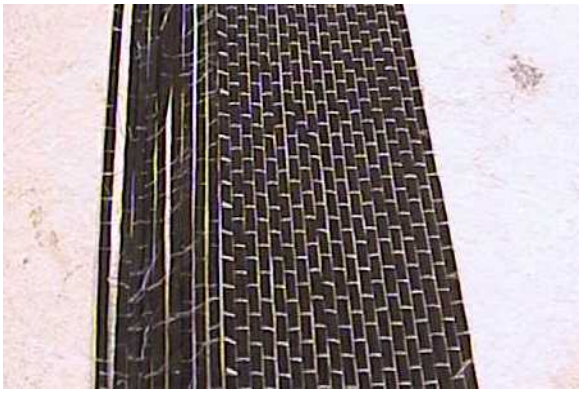

Figure 9-5: Removal of Transverse Stitching

9.4.3 DEFECT [5]: INCORRECT STOICHIOMETRY

In field installation, stoichiometric inconsistencies mostly occur due to deviation from the prescribed resin/hardener ratio. These deviations originate from incorrect quantity measurements and thus remain susceptible to human error.

The experimental program addresses this defect in form of intentional deviations from an ideal resin/hardener ratio of 2:1 (by volume). To model realistic values, reductions of 10 and 20% were studied, i.e. the resin system was given insufficient amounts of hardener, presumably resulting in prolonged or possibly incomplete cure of the matrix material. In terms of the resin/hardener ratio, these deviations resulted in ratios of 2.22:1 and 2.67:1,

respectively. To exclusively study the effects of stoichiometric alteration of the infiltrating resin, priming was performed using a separate resin batch.
During infiltration, a significant effect of resin/hardener ratio on overall viscosity and workability of the material was noted. As such, an increase in viscosity, i.e. reduction in workability, was noted specimens for all specimens. However, this effect was more pronounced for specimens that were laid up using the 2.67:1 resin mix. This effect originated from differences in viscosity of the two resin constituents, as described in Section 9.3.2.3. Although no secondary effects were noted, an increase in viscosity tends to promote formation of voids, fabric lift-up during infiltration and rolling, as well as incomplete wet-out of critical regions.

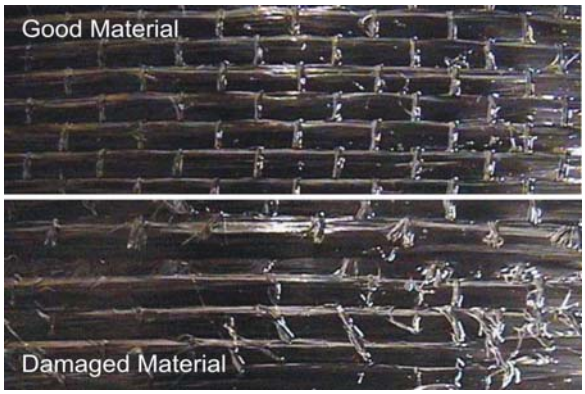

Figure 9-6: Local Effects of Damaged Transverse Stitching

9.4.4 DEFECT [6]: INADEQUATE PRIMER

While primers are used to provide a "bondable" surface and quench the absorption so that none of the saturating resin is drawn from the wet laminate, thickness of the primer should be kept as thin as possible. In regions of excessive priming, resin-rich areas and low stress transfer may result. To study former extremes, three specimens with no prime coating were fabricated. In addition, a second set of specimens was made using approximately twice as much primer resin as outlined in Section 9.4.1, i.e. four coats. This resulted in significant resin build-up on the surface, as illustrated in Figure 9-7. During the subsequent layup, resin infiltration was performed in the conventional manner. As such, both primed and unprimed specimens received one coat of resin prior to placement of the first layer.

9.4.5 DEFECT [11]: PROLONGED PRIMER CURE

Prolonged primer cure was studied by addressing two different preparation procedures. While both procedures resulted in a primer coat that was fully cured, subsequent application of the composite material was performed onto different surface textures. Herein, the primer of the first set of specimens was left in an "as is"-state, i.e. the CFRP material was applied onto a smooth, glossy surface with little to no surface texture. In contrast, the cured primer coating of the second set of specimens was roughened using gp size#120 sandpaper and chemically cleaned using MEK. To enhance bond of the cured, glossy primer surface, sanding was continued until most of the surface shine had been

removed. Subsequently, cotton sticks containing MEK were used to clean the surface of any residue left from the sanding (Figure 9-8). This procedure was continued until no additional residue was noted in the cotton sticks. Finally, all MEK was allowed to evaporate. The difference in surface appearance between the abraded and "as is" specimens is shown in Figure 9-9.

Figure 9-7: Resin Build-up in Regions of Excessive Priming

Similar to all previous layup procedures, one coat of infiltrating resin was applied to the cured primer prior to placement of the first fabric layer. During layup, it was noted that the smooth surface of the cured primer promoted fiber mobility, i.e. fiber misalignment caused by rolling. However, by rolling from the center of the specimens towards the ends in one continuous movement, fiber waviness could mostly be prevented.

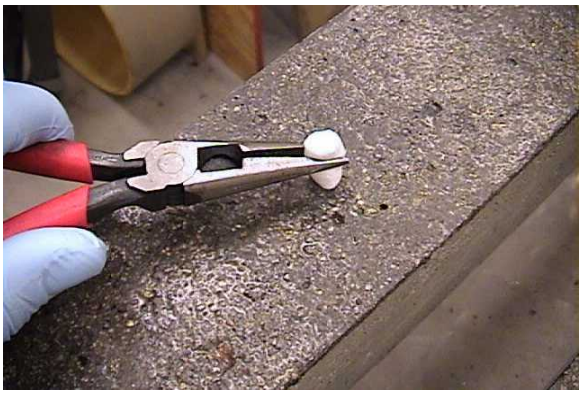

Figure 9-8: Solvent Wiping of Abraded Concrete Surface

Figure 9-9: Comparison Between Abraded and "As is" Surfaces

9.5 TESTING

Testing of specimens was performed after cure of exactly 4 days. This duration was chosen based on results of a previously conducted DSC analysis, results of which are given in Figure 9-10. As may be noted, most of the cure process occurred within the first two days following mixing. Although a continuous increase in cure could be noted throughout the test period, the change in exothermal energy became substantially less once the resin had been cured for 2 to 4 days. Further, due to continuation of resin cure with increasing age of specimens, all testing was performed during a single day. As such, possible effects of differences in degree of cure were eliminated.

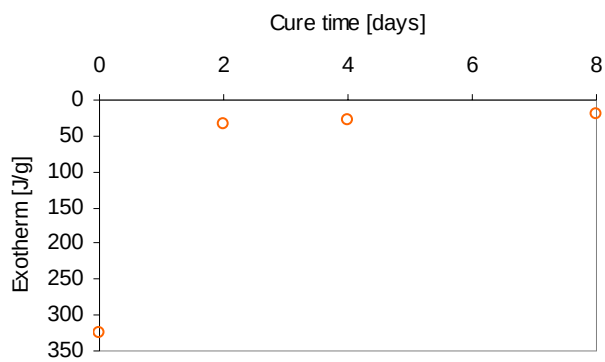

Figure 9-10: DSC Cure Study for FM-1 Resin System

Similar to previous specimens, a brittle, white fluid was used to enhance visibility of crack growth along the edges of specimens. Once the coating had dried, paper rulers were attached to allow for correlation between the recorded video images and actual crack length on each side of the specimen. Specimens were placed onto the steel fixture and the horizontal and vertical position of the loading head was calibrated such that the loading rod would barely touch the composite membrane. Also, it was ensured that the steel rod was situated equidistant from both ends of the specimen.

All testing was performed in a quasi-static manner, using a vertical cross-head velocity of 0.04-in/min (1-mm/min). Specimens were loaded to the point of crack initiation while

continuously recording load-displacement data. Prior to crack initiation, video recording was initiated and continued until all CFRP material was peeled from the concrete substrate. Herein, abnormal peel behavior, such as crack "jumps" or interlaminar separation of plies was documented for further evaluation. Upon completion of a test, video recording was terminated and the loading rod was returned to its initial position. After each test, the yet unbonded regions of the CFRP membranes were manually peeled off. Average peel width was determined from width measurements taken on both sides of the composite sheet. Subsequently, tensile test coupons of 1 x 10-in (25.4 x 254-mm) were cut from the smooth center regions of the laminate using a wet tile saw. Results from these tests were used to calculate fracture energy release rate of each specimen.

As mentioned earlier, testing of specimens was not performed in an order following that given in Table 9-1. Hence, Table 9-5 provides information necessary to correlate between defect number and specimen number.

Table 9-5: Correlation between Defect- and Specimen Number

DEFECT #	SPECIMEN #	PARAMETER	SPECIMEN #	PARAMETER
[C-W]	*T-1, T-20*	-	-	-
[3]	*T-2 to T-4*	*½" into fabric*	*T-5 to T-7*	*1" into fabric*
[5]	*T-14 to T-16*	*-25% R/H-ratio*	*T-17 to T-19*	*-10% R/H-ratio*
[6]	*T-21 to T-23*	*No priming*	*T-24 to T-26*	*200% priming*
[8]	*T-8 to T-10*	*Abraded*	*T-11 to T-13*	*As is*

10 TEST RESULTS

10.1 Load-Deflection Curves

In the following sections, load-displacement graphs from all previous peel testing are shown and discussed. The plots are given for each of the defect categories, including results for the control specimens *T-1* and *T-20*. Further, graphs depict only a single parameter of one defect category. As such, possible effects of these parameters on load-displacement behavior were more easily noticeable.

10.1.1 Control Specimens – Wet Layup

The load-displacement plots for wet layup control specimens *T-1* and *T-20* are depicted in Figure 10-1. It may be noted that load-displacement behavior was nearly identical, indicating good reproducibility of the performed layup procedure. Also, peeling occurred at a relatively constant load level, which supports the assumption that control specimens were evenly fabricated throughout the bonded distance. From a displacement at onset of cracking of roughly 26-mm, it can be concluded that the strain in the CFRP membrane was about 0.0024-mm/mm. Hence, previous assumption of linear-elastic behavior throughout the entire course of the tests can also be confirmed. Finally, comparing the surface morphology between specimens *T-1* and *T-20*, as shown in Figure D-1 and Figure D-3 of Appendix D, it may be noted that specimen *T-20* displayed a substantially higher degree of aggregate exposure. Interestingly, this observation cannot as yet confirm a generally expected increase in peel force due to higher surface roughness.

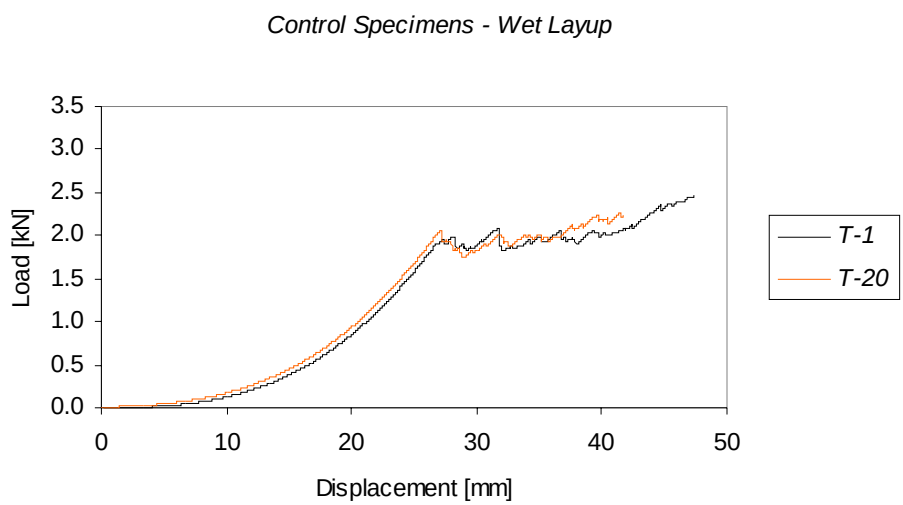

Figure 10-1: Load-displacement Behavior of Control Specimens (Wet Layup)

10.1.2 Defect [3]: Damage to Free Edges

Load-displacement behavior for both degrees of edge damage is shown in Figure 10-2 and Figure 10-3. A direct comparison between the two graphs leads to the conclusion that an increase in fabric disturbance caused a larger variation in load-displacement behavior. As shown, data scatter was significantly higher for specimens containing a 1-in wide defect, while those containing narrower edge defects tended to be more uniformly

distributed. Further, compared to control specimens, data scatter within a single specimen increased noticeably. This may be attributed to the fact that irregularities, caused by fiber overlap, twisting or transverse movement of fiber tows, resulted in localized resin-rich regions. It is noteworthy that for some specimens, average peel force was higher compared to that experienced for control specimens.

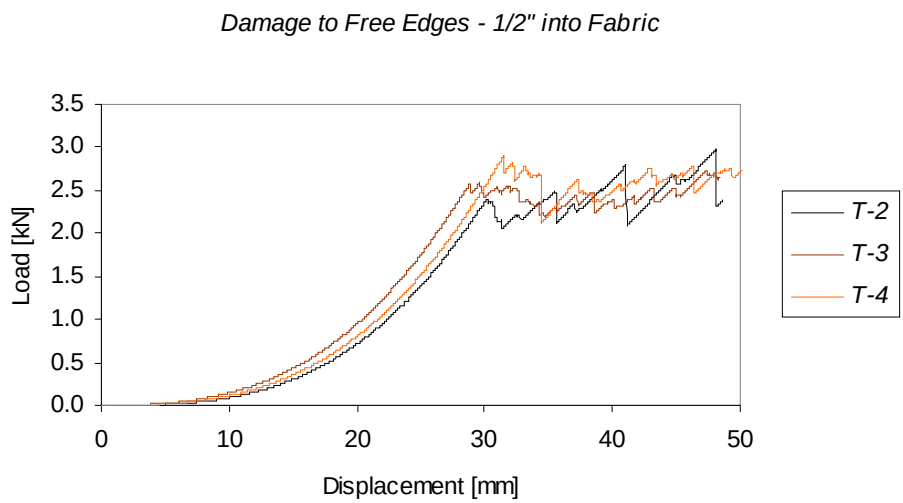

Figure 10-2: Load-displacement Behavior of Specimens T-2 to T-4

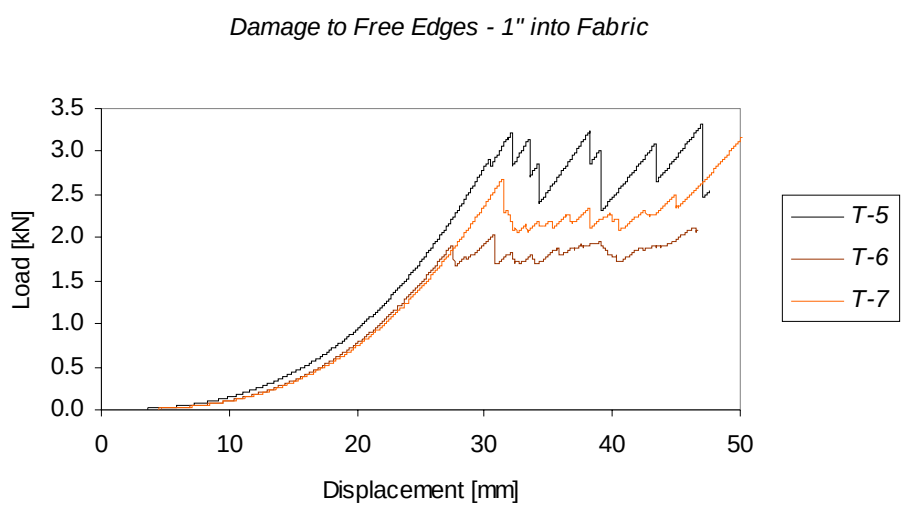

Figure 10-3: Load-displacement Behavior of Specimens T-5 to T-7

10.1.3 Defect [5]: Incorrect Stoichiometry

Observing graphs of load-displacement behavior for specimens using incorrect stoichiometry (Figure 10-4 and Figure 10-5) resulted in the following findings. Firstly, similar to the previous Section, data scatter was substantially higher that that of control specimens. Secondly, a 25% reduction in resin/hardener ratio appeared to result in crack "jumping", i.e. the crack front was arrested at specific intervals and further cracking is

prevented. Once a sufficient amount of elastic strain energy had built up in the CFRP membrane, cracking commenced in a rapid manner, resulting in a sudden crack jump, accompanied by a substantial loss in peel force. In contrast, resins with only a 10% reduction in resin/hardener ratio generally resulted in a more constant peel force with fewer locations of crack arrest. The difference in average peel force between specimen *T-17* and specimens *T-18* and *T-19* may be attributed to differences in surface appearance, as shown in Figure D-3 of Appendix D. As may be noted, specimen *T-17* retained a substantial amount of cement paste, possibly resulting in an overall decrease in peel force.

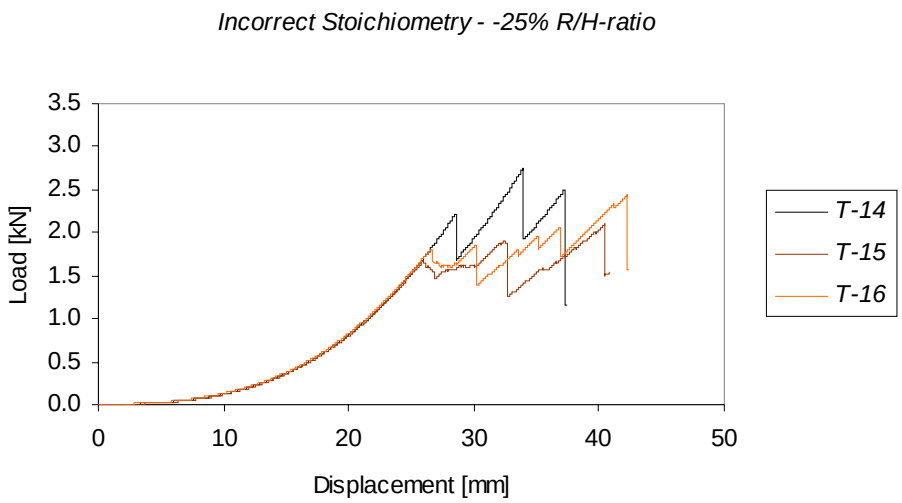

Figure 10-4: Load-displacement Behavior of Specimens T-14 to T-16

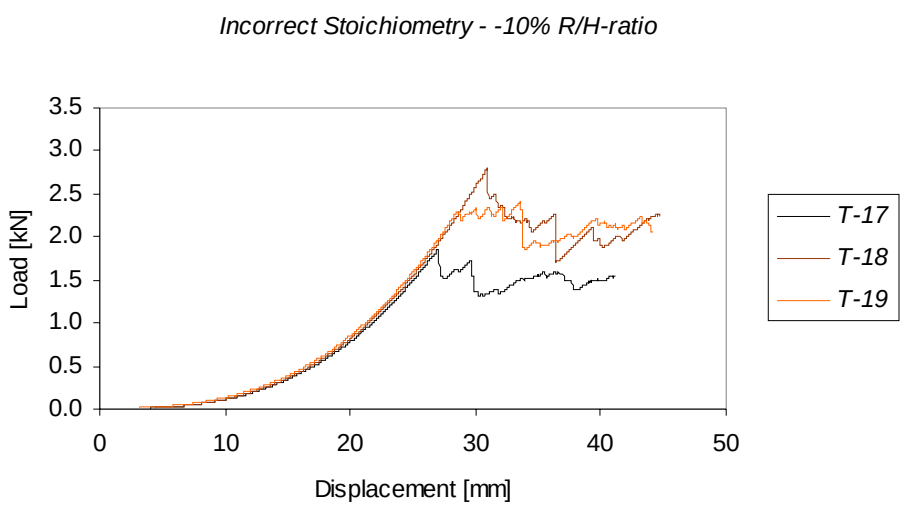

Figure 10-5: Load-displacement Behavior of Specimens T-17 to T-19

10.1.4 Defect [6]: Inadequate Primer

The effects of inadequate priming on load-displacement behavior are depicted in Figure 10-6 and Figure 10-7. Interestingly, load-displacement behavior of unprimed specimens was largely similar to that observed for control specimens. However, a minimal increase in data scatter was noticed. Also, average peel force was slightly lower, indicating a reduction in bond strength due to insufficient infiltration of the substrate.

Unlike the unprimed specimens, excessive priming appeared to promote an increase in data scatter. Such behavior may be linked to a higher non-uniformity of the bondline thickness and consequent formation of resin-rich regions. While bond strength was slightly increased, uniformity of the peel behavior was compromised, again resulting in a larger data scatter within a single test.

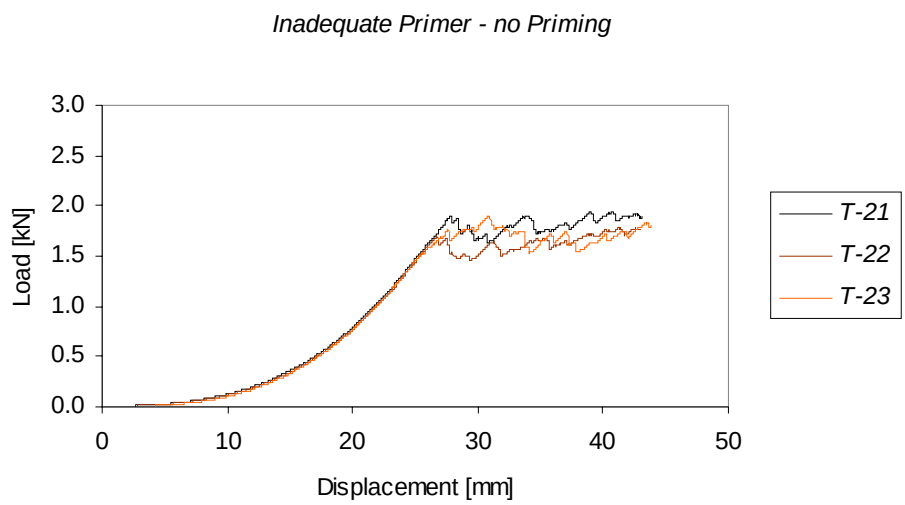

Figure 10-6: Load-displacement Behavior of Specimens T-21 to T-23

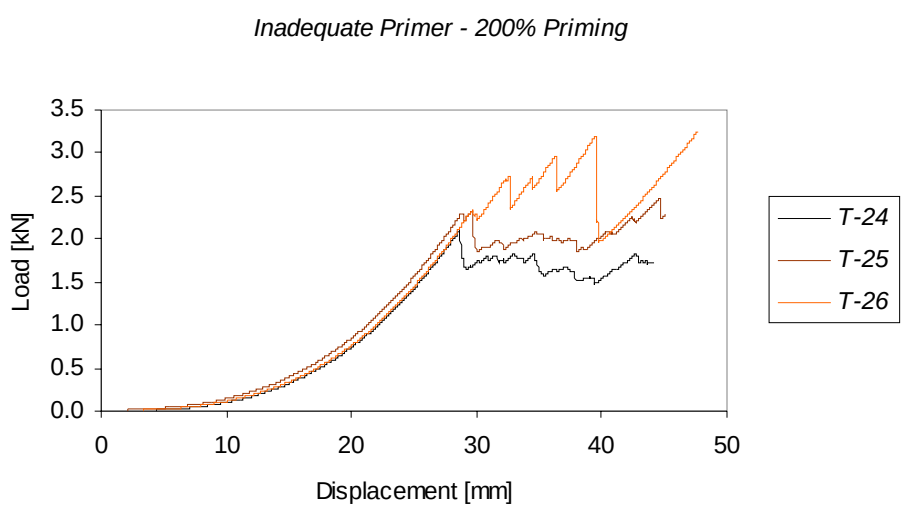

Figure 10-7: Load-displacement Behavior of Specimens T-24 to T-26

10.1.5 Defect [8]: Prolonged Primer Cure

Results for specimens fabricated under the condition of prolonged primer cure are shown in Figure 10-8 and Figure 10-9. Foremost, a large reduction in peel force was noted, averaging at only 25% of that recorded for control specimens. While both defect parameters resulted in substantial data scatter, specimens fabricated under the "as is" condition experienced the most dramatic crack "jumping". For all three specimens, two distinct instances of sudden load reduction could be noticed. Although an identical behavior could be linked to specimen *T-10*, specimens *T-8* and *T-9* appeared to peel in a more continuous manner. Further, average peel force was slightly higher for specimens that were abraded and solvent-wiped prior to application of the CFRP overlay.

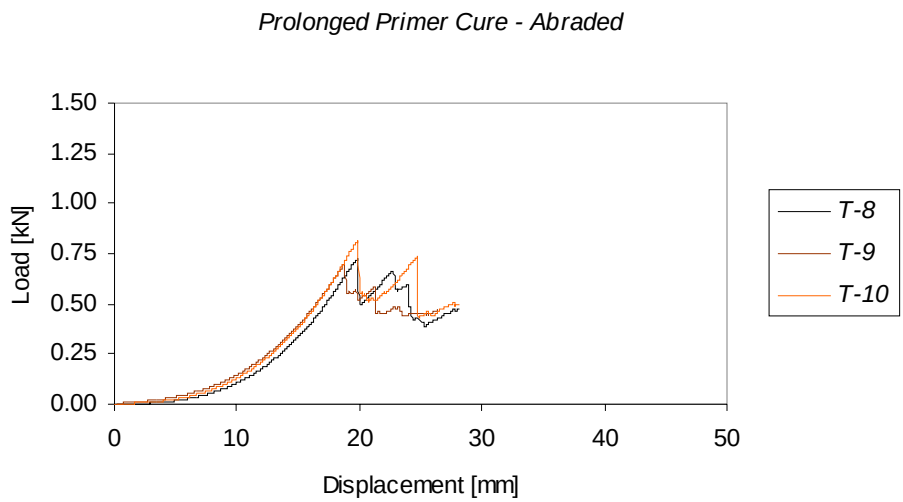

Figure 10-8: Load-displacement Behavior of Specimens T-8 to T-10

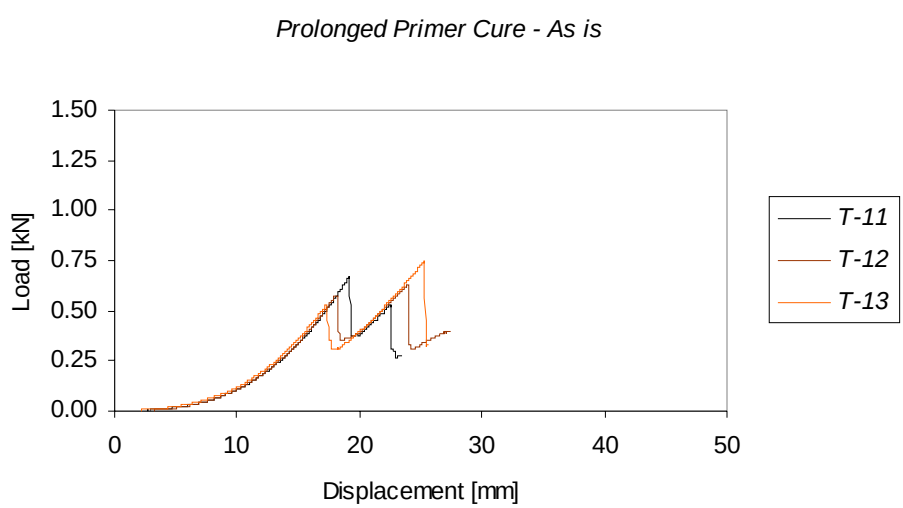

Figure 10-9: Load-displacement Behavior of Specimens T-11 to T-13

10.2 FRACTURE ENERGY RELEASE RATES

As fracture toughness has previously been introduced as a relative measure for bond strength, this Section presents graphs of fracture energy release rate for all tests. Again, results are given in the order they were listed in Table 9-1 instead of their sequence of testing. Using crack propagation data from the video monitoring equipment in conjunction with displacement data obtained from the loading frame, FERR was computed via Equation (7.11). Further, data scatter was determined based on the minimum and maximum values recorded during each test.

Apart from the graphical representation, numerical results are presented in tabular format in each corresponding Section, including specimen number, defect parameter, FERR of the individual specimen, as well as an average value of *G* computed for each set of specimens. Lastly, the percentage of increase/decrease with respect to the control specimens is given.

10.2.1 CONTROL SPECIMENS – WET LAYUP

Similar to the load-displacement graphs depicted in Section 10.1.1, fracture toughness of the two specimens was in good agreement. Further, data scatter is nearly identical for both specimens. From Figure D-1 and D-3 in Appendix D, it may again be noted that the surface morphology of specimen T-20 displays a noticeably higher aggregate exposure, which was reflected as a slight increase in fracture toughness. Nonetheless, this increase is minimal and may therefore originate from additional factors, including minute differences in the infiltration procedure, causing a variation in bondline thickness, etc. Overall, it can be assumed that the obtained values of fracture toughness for specimens fabricated via the wet layup procedure were largely representative of the actual fracture toughness expected for such manufacturing method. Numerical values and graphical representations of fracture toughness are given in Table 10-1 and Figure 10-10, respectively.

Table 10-1: FERR of Control Specimens

SPECIMEN #	PARAMETER	$G_{AVERAGE}$ [kJ/m^2]	$G_{OF\ SET}$ [kJ/m^2]	$\pm G_{CONTROL}$ [%]
T-1	n.a.	0.856	0.869	n.a.
T-20	n.a.	0.882		

10.2.2 DEFECT [3]: DAMAGE TO FREE EDGES

Fracture toughness for specimens that were manufactured under the influence of edge damage is given in Table 10-2 and Figure 10-11. Interestingly, for specimens containing the ½-in deep defect, fracture toughness appeared to increase by a significant amount, while the increase in *G* was not as pronounced for the 1-in (25.4-mm) deep defect. Nonetheless, both sets of specimens reflected an increase of fracture energy release rate between 24 and 42%. These results can possibly be explained as follows.

Firstly, as illustrated in Figure D-1 of Appendix D, surface treatment resulted in a substantial degree of surface roughness, resulting in an increase in “bondable” area. This is supported by the fact that specimens *T-3* and *T-6* show the lowest degree of aggregate exposure and are also found to have resulted in the lowest fracture toughness of each set

of specimens. In fact, results of specimen *T-6* are slightly lower compared to those of control specimens. Alternatively, the average increase in fracture toughness could be attributed to the fact that, although transverse integrity of the fiber tows was diminished, flatness could have possibly been increased. Given the fact that the weak transverse stitching had been removed throughout the bonded length of the material, the fiber tows were now able to bond directly to the underlying substrate, i.e. bondline thickness slightly lowered.

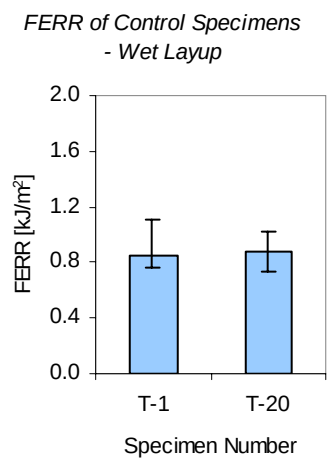

Figure 10-10: Comparison of FERR for Control Specimens

It can further be noted that data scatter is more pronounced for specimens of high fracture toughness, i.e. those that display higher aggregate exposure. As mentioned, high aggregate exposure tends to result in a more frequent and sudden crack arrest, leading to rapid, locally unstable crack propagation. A higher data scatter therefore accompanies it.

Table 10-2: FERR of Defect [3]

SPECIMEN #	PARAMETER	$G_{AVERAGE}$ [kJ/m^2]	$G_{OF\ SET}$ [kJ/m^2]	$\pm G_{CONTROL}$ [%]
T-2	½”	1.240		
T-3	½”	1.046	1.230	+42.0
T-4	½”	1.405		
T-5	1”	1.217		
T-6	1”	0.829	1.075	+24.0
T-7	1”	1.179		

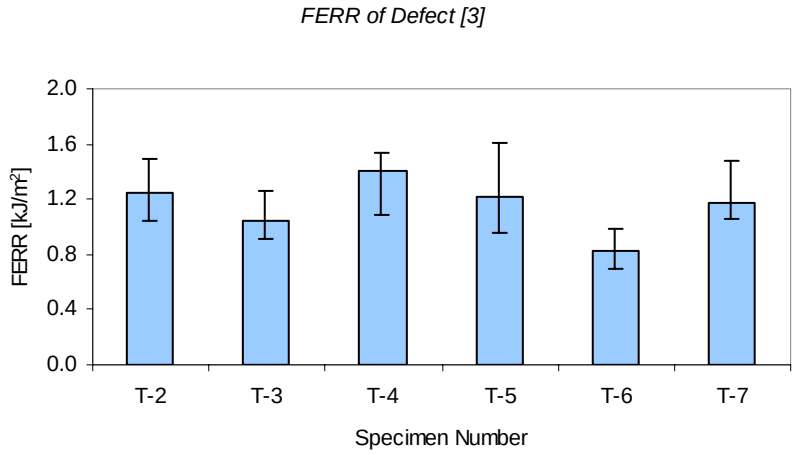

Figure 10-11: Comparison of FERR for Defect [3]

10.2.3 DEFECT [5]: INCORRECT STOICHIOMETRY

The effects of stoichiometric variation are represented in Table 10-3 and Figure 10-12, showing a reduction in fracture toughness with increasing alterations in resin/hardener ratio. As mentioned, resins mixed from a –25% resin/hardener ratio showed a significant increase in viscosity, which may have resulted in formation of dry areas, voids or resin-richness, all being potential factors for a reduction in fracture toughness. Given the fact that surface morphologies of specimens *T-14* to *T-16* (Figure D-2 of Appendix D) display a rougher texture than those found for the two control specimens, it can be assumed that the reduction in fracture toughness is solely due to the variation in resin properties. Conversely, the minimal increase of about 5% for specimens with a –10% stoichiometric variation may be linked to the higher surface texture of specimens *T-18* and *T-19*, which may be observed in Figure D-2 of Appendix D. In this context, the high paste content of specimen *T-17* also provides an explanation for the substantial decrease in fracture toughness by approximately 22%.

Table 10-3: FERR of Defect [5]

SPECIMEN #	PARAMETER	$G_{AVERAGE}$ [kJ/m^2]	$G_{OF\ SET}$ [kJ/m^2]	$\pm G_{CONTROL}$ [%]
T-14	-25% R/H-ratio	0.691		
T-15	-25% R/H-ratio	0.732	0.714	-17.8
T-16	-25% R/H-ratio	0.718		
T-17	-10% R/H-ratio	0.683		
T-18	-10% R/H-ratio	1.069	0.913	+5.1
T-19	-10% R/H-ratio	0.987		

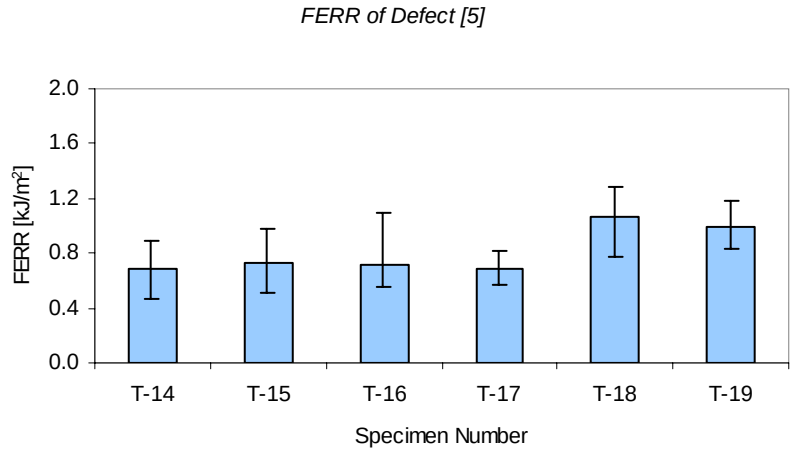

Figure 10-12: Comparison of FERR for Defect [5]

10.2.4 DEFECT [6]: INADEQUATE PRIMER

As may be noted from Table 10-4, only a slight reduction in fracture toughness was experienced for specimens containing unprimed surfaces. Herein, the reduction of 4.7% may originate from a variety of factors and cannot generally be linked to alterations in the priming process. In addition, surface images of specimens *T-21* to *T-23* do not display a significant difference in texture if compared to the control specimens. As such, it can be excluded that an increase in surface texture has compensated for an otherwise predominant reduction in fracture toughness due to insufficient priming.

With respect to data scatter, it can be noted that specimens containing 200% primer reflect a substantially higher variation in fracture toughness. This may again be linked to variations in bondline thickness. Due to the difficulty of introducing a uniform resin-rich layer or primer (compare Figure 9-7), some specimens were possibly more saturated than others.

Table 10-4: FERR of Defect [6]

SPECIMEN #	PARAMETER	$G_{AVERAGE}$ [kJ/m^2]	$G_{OF\ SET}$ [kJ/m^2]	$\pm G_{CONTROL}$ [%]
T-21	No priming	0.836		
T-22	No priming	0.821	0.828	-4.7
T-23	No priming	0.828		
T-24	200% priming	0.904		
T-25	200% priming	1.058	1.079	+24.1
T-26	200% priming	1.275		

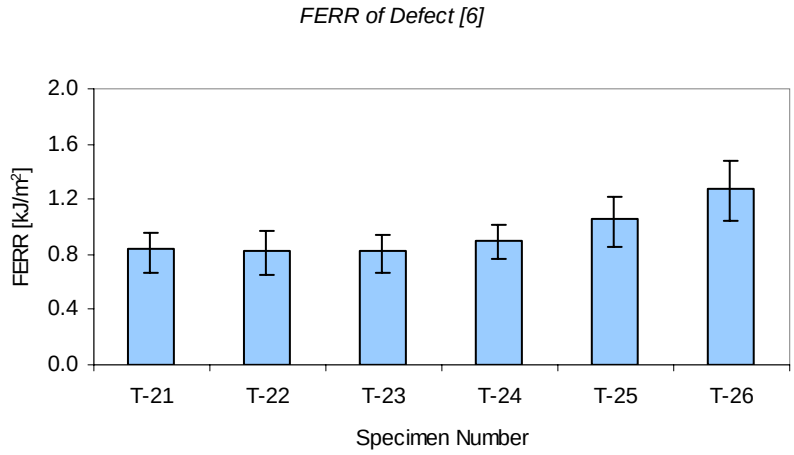

Figure 10-13: Comparison of FERR for Defect [6]

10.2.5 DEFECT [8]: PROLONGED PRIMER CURE

As depicted in Table 10-5 and Figure 10-14, the fracture energy release rates calculated for specimens of prolonged primer cure clearly reflect a dramatic decrease in bond strength. While data scatter is relatively small, the reduction in fracture toughness ranges from 85% to nearly 90% of that measured for control specimens. Herein, abrasion of the cured primer surface and subsequent cleaning with MEK did not results in a significant increase in fracture energy. Also, as seen from FERR plots of Appendix E, fewer data points could be recorded during testing, which was conditioned by abrupt nature of crack propagation for these specimens.

From the above finding, it can be concluded that prolonged primer cure causes a dramatic reduction in fracture energy in combination with sudden and rapid crack propagation. Particularly, the efficacy of subsequent surface abrasion has been shown to cause only a negligible increase in fracture toughness.

Table 10-5: FERR of Defect [8]

SPECIMEN #	PARAMETER	$G_{AVERAGE}$ [kJ/m^2]	$G_{OF\ SET}$ [kJ/m^2]	$\pm G_{CONTROL}$ [%]
T-8	Abraded	0.147		
T-9	Abraded	0.112	0.129	-85.2
T-10	Abraded	0.128		
T-11	As is	0.096		
T-12	As is	0.098	0.094	-89.2
T-13	As is	0.089		

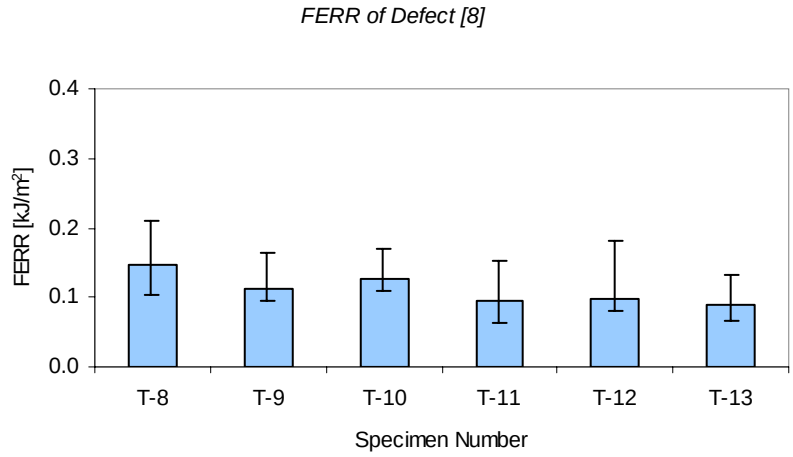

Figure 10-14: Comparison of FERR for Defect [8]

10.3 Fracture Surfaces

Apart from evaluation of fracture energy release rates, observation of fracture surfaces can provide valuable information on fracture behavior. Herein, it is essential to differentiate between different failure modes as well as different propagation paths. For the test setup utilized in this study, cracking mainly occurred in form of mode II, which may be shown by observing the fracture image shown in Figure 10-15. A chipped structure of the cement paste clearly indicates this mode. In comparison, the image shown in Figure 10-16 was obtained from a surface that was peeled off manually, once the test had been completed. It can be seen that the surface texture is substantially different from that in the previous illustration, given the fact that the membrane was removed under a mode I condition rather than a mixed mode. Regarding crack propagation, fracture is likely to occur along two predominant paths, namely the top layer of the concrete substrate and the adhesive layer. Correspondingly, these types of cracking are denoted cohesive and adhesive failure.

Figure 10-15: Fracture Surface Obtained from Actual Test Conditions

Figure 10-16: Fracture Surface Obtained from Manual Peel-off

Images obtained from the two control specimens *T-1* and *T-20* are depicted in Figure 10-17 and Figure 10-18, respectively. It can be noted that both specimens underwent cracking with significant removal of paste material, hence the failure path was mostly cohesive. Only few regions show signs of the composite membrane, possibly indicating protrusion of a strong aggregate particle that could not be penetrated by the propagating crack front.

Figure 10-17: Fracture Surface of Control Specimen (T-1)

Figure 10-18: Fracture Surface of Control Specimen (T-20)

In contrast, images in Figure 10-19 and Figure 10-20 represent fracture surfaces of specimens *T-25* and *T-26*, i.e. those that were prepared with excessively primed surfaces. On specimen *T-25*, removal of the cement cover did not occur over the entire area, while specimen *T-26* peeled without any sign of paste removal. The reasoning for this phenomenon is twofold. Firstly, the high accumulation of resin primer may have caused adhesive failure, especially in regions where bondline thickness was substantially higher. In such regions, the benefit of high adhesion was lost and possibly resulted in crack propagation along the adhesive interface. Secondly, compared to control specimens, specimens *T-25* and *T-26* displayed a significantly higher degree of aggregate exposure (as shown in Figure D-3 and D-4 in Appendix D), i.e. to cause cohesive failure, the crack front was required to penetrate through the strong aggregate. As a result, the crack propagated along the outermost surface of the aggregate, causing a crack surface that shows very little signs of concrete residue.

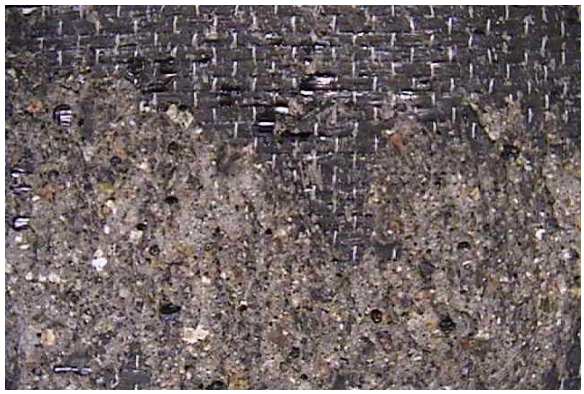

Figure 10-19: Fracture Surface of Specimen T-25

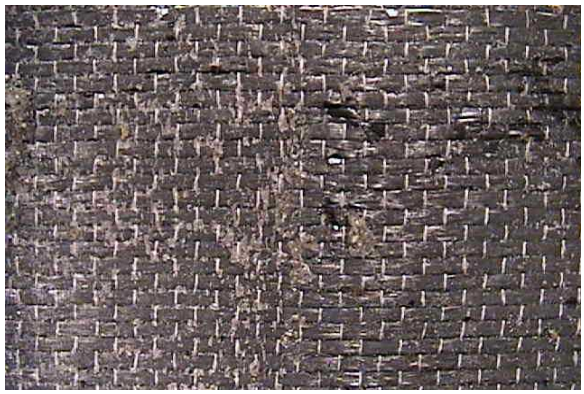

Figure 10-20: Fracture Surface of Specimen T-26

As expected, specimens fabricated under the condition of prolonged primer cure depict fracture surfaces that are clearly representative of adhesive, i.e. lower-energy failure. As such, fracture images of the abraded specimen *T-8* and "as is" specimen *T-11* depict a smooth, low-texture surface with no signs of cohesive failure, as depicted in Figure 10-21

and Figure 10-22, respectively. From direct comparison, it may be noted that abrasion has caused only a minimal effect, noticeable in form of several white spots throughout the fracture surface. Nonetheless, mechanical and chemical surface abrasion appears to be entirely ineffective in recovering adhesive properties of a cured resin system.

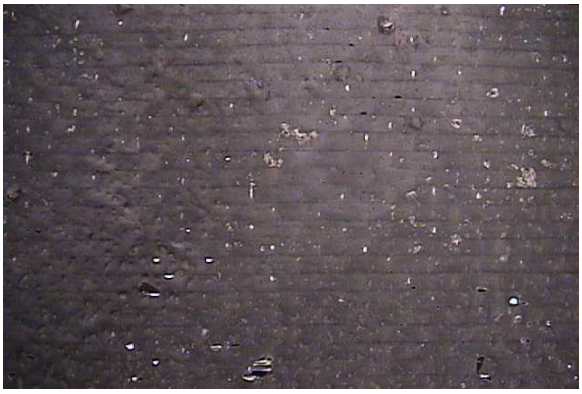

Figure 10-21: Fracture Surface of Specimen T-8

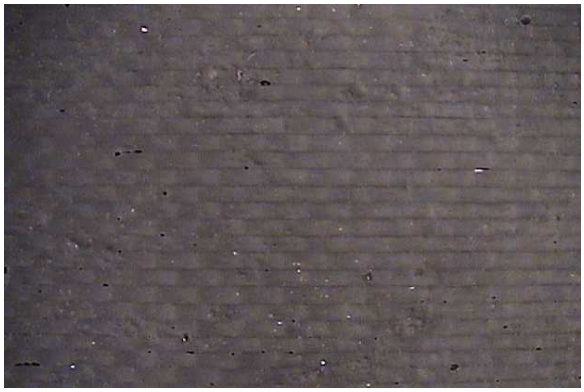

Figure 10-22: Fracture Surface of Specimen T-11

11 DISCUSSION

Despite the limited number of defects investigated to date, preliminary findings may be utilized to assess the relative criticality of several defects of wet layup systems. Currently available data already provides valuable indications that may serve to enhance the efficacy of in-situ rehabilitation procedures. As was shown, measuring fracture toughness is suitable for providing information on bond quality and may thus be utilized to categorize defects in terms of their relative criticality. In the following, results of Chapter 10 will be discussed.

Given the fact that the present study was based on assessing fracture toughness as a relative measure, establishment of a baseline value, representing a structurally sound layup, was a foremost necessity. To obtain such baseline, a set of control specimens was fabricated, using identical and reproducible layup procedures. Results of fracture tests on control specimens *T-1* and *T-20* have indicated that load-displacement behavior and fracture toughness were in good agreement. It can thus be concluded that a fracture energy release rate of 0.87-kJ/m^2 was representative for bond strength of a properly rehabilitated component, provided that surface treatment and constituent materials are identical to those utilized in the present study. For a direct comparison of fracture toughness for all specimens included in the present study, comprehensive results are again depicted in Figure 11-1.

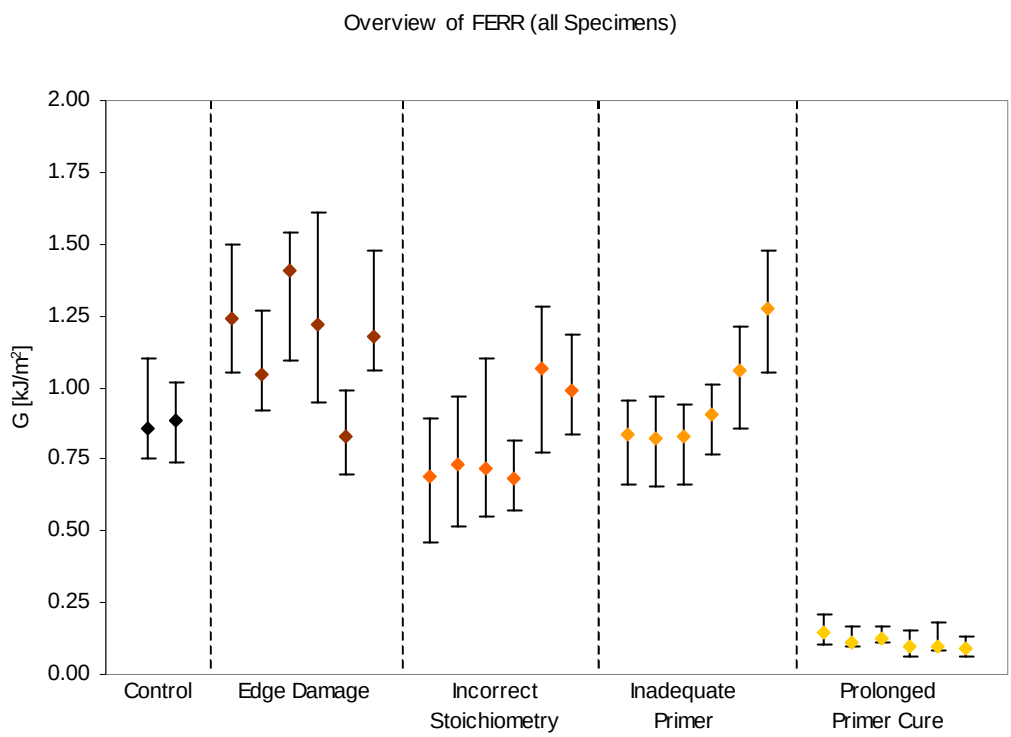

Figure 11-1: Comprehensive Comparison of FERR

During fabrication and testing of specimens containing different levels of edge damage, it was shown that defects related to edge damage generally result in difficulties during the layup procedure. As such, the unrestricted fiber tows tend to spread apart during rolling, causing fiber twisting and overlapping, eventually leading to formation of resin-rich regions. Further, given the lowered restrictedness, fiber waviness was likely to occur.
Surprisingly, fracture toughness measured for these specimens was generally higher than that evaluated for control specimens, indicating an increase in bond strength for systems that do not employ transverse stitching. More specifically, specimens containing a ½-in wide region of damage experienced an increase in fracture toughness of 42% while those with more significant loss in fiber integrity showed an increase of only 24%.
Although a rationale for this increase in bond strength may be given based on the differences in surface morphology, a second mechanism may be responsible for this. As mentioned earlier, removal of transverse stitching may have resulted in a flattening effect thus leading to a decrease in bondline thickness in regions where transverse stitching would have otherwise caused accumulation of higher levels of resin. In this context, it should be mentioned that alternative materials are currently being used for external strengthening of concrete structures, some of which do not utilize transversely oriented material. As shown in Figure 11-2, these materials are purely unidirectional with no additional transverse material to restrict fiber mobility. Instead, the CFRP tows are placed onto a backing paper that is removed as the material is placed onto the structure. As such, fiber distortion can be largely prevented while ensuring a preferably thin interfacial region between concrete and composite. The material shown in Figure 11-2 is currently applied in structural rehabilitation efforts in Sweden.

Figure 11-2: Weft-free Material for Structural Rehabilitation

Stoichiometric alterations up to a level of 10% have shown to result in an increase of fracture toughness, indicating the noticeable effect of surface texture on measurement of bond strength. Nonetheless, it can be assumed that the effect of stoichiometric alteration up to levels of 10% are rather insignificant and that although exact measurement of constituents should be performed with care, slight deviation from the prescribed mix ratio do not result in significant reduction in bond quality. However, it was shown that alterations in mix ratio of 25% substantially lowered fracture toughness. Also, for these specimens, surface texture did not vary from that found on control specimens. In

comparison, surface morphology of specimens fabricated under a 25% reduction in resin/hardener ratio was actually more textured compared to control specimens. Hence, based on the effects of surface roughness alone, these specimens should have yielded higher values of *G*.
It can thus be concluded that a reduction of resin/hardener ratio at levels significantly exceeding 10% must be viewed critical. As mentioned, it remains uncertain whether these effects originate from mechanical degradation of the resin system or secondary effects such as formation of voids and dry regions due to an increase in resin viscosity.

Unlike previous findings, no detrimental effects could be shown for the case of alterations in the priming procedure. While all specimens showed a similar surface texture, the slight increase in fracture toughness for excessively primed specimens may be attributed to the fact that these specimens did not contain any unfilled cavities on the concrete surface. Due to the rolling process, which was performed at an uncured state of the resin, most of the matrix material was possibly removed from underneath the carbon fabric and forced into the fiber structure. As a result, bondline thickness of these specimens was presumably identical to that of unprimed specimens. It should again be noted that, while the priming process serves quenching of the dry and porous concrete surface, it further allows formation of a tacky surface, presupposing that the material is allowed to set for about 15 minutes. However, the importance of this procedural step is only given for overhead applications, i.e. situations where the weight of the wet material would otherwise results in separation of the CFRP and host material.
Consequently, surface priming should not be omitted in applications that demand a certain level of initial surface tackiness. For level applications in which the resin may not drain from the substrate and for which material sag is of no concern, priming is of lesser importance.

Further, it was shown that prolonged primer cure has a detrimental effect on bond strength, resulting in a reduction of fracture toughness up to 90%. Herein, only a slight difference in reduction was noted for specimens whose primer surface was exposed to abrasion and solvent wipe prior to application of the CFRP overlay. It must thus be assumed that manual sanding is ineffective in providing adequate surface roughness of the previously cured resin system. Herein, it appears feasible to study the efficacy of electric disc sanders.
For all previous tests, cracking occurred in either a truly cohesive manner, i.e. through the top layer of weak cement paste, or along the concrete/adhesive interface. Herein, the adhesive is represented by the resin system used for both infiltration and bonding. Instead, crack propagation on specimens *T-8* to *T-13* occurred within the adhesive material. This indicates that the outer surface of the cured resin system was unable to allow a second bond of equal strength to form. Hence, a weak failure plane developed. This is further supported by images taken of the fracture surface (Figure 10-21 and Figure 10-22), which neither display signs of concrete residue nor any fiber texture.

Finally, in view of the analytical methodology followed in this investigation, fracture toughness was evaluated using a simple theoretical model. However, the model necessitated calculation of tensile modulus of the CFRP membrane for each of the

specimens tested. Herein, it was shown that the maximum vertical cross-head displacement prior to initial cracking did not exceed 30-mm, indicating a maximum tensile strain of only 0.3%. Consequently, throughout the peel test, all CFRP materials remained in a truly elastic range, yielding validity of subsequent coupon testing.

Also, a data scatter was more pronounced for specimens with higher levels of surface roughness, indicating the occurrence of crack "jumping" and local instability, as outlined in Appendix B. Lastly, it should be noted that a direct comparison between fracture surfaces obtained from test specimens (Figure 10-15) and those obtained from manual peel off (Figure 10-16) has shown a substantial difference in fracture surfaces. This observation supports the difference in fracture modes between the two forms of peeling, which was a precondition for representative results of this study.

12 CONCLUSIONS

Although structural rehabilitation via CFRP composite overlays has been studied and successfully applied for numerous years, the effect of defects on performance and integrity of such rehabilitated systems remains largely unknown. Hence, an urgent need for establishing the criticality of defects exists.
In the current study, general background information on previous fracture testing was provided. From this, a theoretical approach for measuring fracture toughness was introduced using alternative means of continuously measuring crack propagation using a stationary video monitoring system. It was found that the test setup and fracture mechanisms utilized in the present study are largely representative of mechanisms experienced in structural rehabilitation. Prior to testing, a validation study was conducted, confirming applicability if the proposed model.

From preliminary results of this study, numerous conclusions can be drawn. These include the following:

1. Levels of concrete abrasion significantly influence fracture toughness of a rehabilitated system. Herein, an increase in surface texture, originating from a higher degree of aggregate exposure, results in an increase of fracture toughness. In view of defect criticality, it must be assumed that the effects of defects may be overshadowed by alterations in surface roughness.

2. Damage to the transverse stitching of CFRP materials may cause difficulties during the layup procedure, possibly resulting in local overlapping and twisting of fiber tows. While this defect complicates the installation procedure, the levels addressed in this study did not show to cause a reduction in fracture toughness. Instead, fracture toughness was increased in most cases, possibly indicating the effect of enhanced fiber straightness. It was found use of carbon fabric not containing transverse stitching might in fact yield higher fracture energy release rates. However, such conclusion should be confirmed through further experimental studies.

3. Stoichiometric alterations of the adhesive/laminating resin of levels up to 10% have not indicated a detrimental effect on fracture properties. However, for larger variations in resin/hardener ratio, viscosity of the epoxy resin system utilized in the present study has increased substantially, resulting in lower workability.

4. Omission of primer coating has not been indicative of detrimental effect on fracture toughness. Nonetheless, it should be noted that priming partially serves to provide a tacky surface that reduces the likeliness of sagging, a phenomenon that is particularly critical in overhead regions.

5. Compared to all previous defects, prolonged primer cure must be considered highly critical, as reductions in fracture toughness of up to 90% were noted.

Unlike the cohesive failure of other specimens, fracture surfaces indicated failure within the adhesive. Further, the smooth texture of failure surfaces indicated the low efficacy of post-cure abrasion and solvent wipe. It must hence be concluded that primer coats must not be allowed to completely cure as manual surface abrasion has proven ineffective to provide a "bondable" surface.

From above findings, a preliminary criticality matrix was assembled and is shown in Table 12-1. However, it should be noted that applicability of these results largely depends on the location of the defect. As shown in Chapter 2, variation in shear and peeling stresses along the length of a rehabilitated concrete beam is significant. Thus, these findings may only serve as a preliminary indication towards criticality. A more detailed analysis considering the effects of defect location must hence follow.

Table 12-1: Relative Criticality Rating

DEFECT	PARAMETER	$\pm G_{CONTROL}$ [%]	CRITICALITY RATING	COMMENTS
Damage to free edges	½-in deep	+42.0	Low	-
	1-in deep	+24.0	Medium	Although no reduction in fracture toughness was noted, fiber integrity is reduced substantially, resulting in inferior handling and possibly induction of secondary defects (waviness, resin-richness)
Incorrect Stoichiometry	-10% R/H-ratio	+5.1	Low	A deviation from the prescribed R/H-ratio of up to 10% may be viewed as extreme, considering the fact that resins are typically mixed from complete kits, i.e. the constituent quantities are determined during manufacture of the resin system
	-25% R/H-ratio	-17.8	Medium	Given above reasoning, deviation from the R/H-ratio of 25% or more must be considered highly unlikely. Nonetheless, it was shown that alterations in resin viscosity adversely affect workability, indicating that use of overaged resin systems may result in a similar reduction of fracture toughness, mainly conditioned by implementation of secondary defects (voids, dry spots)
Inadequate Priming	No priming	-4.7	Low	For the test configuration employed in this study, omission of priming did not yield lower fracture toughness. Nonetheless, considering that priming is performed to obtain a tacky surface, it remains an essential precondition, particularly in overhead applications

Table 12.1: Relative Criticality Rating (continued)

DEFECT	PARAMETER	$\pm G_{CONTROL}$ [%]	CRITICALITY RATING	COMMENTS
Inadequate Priming	200% priming	+24.1	Low	Excessive priming is not critical presupposing that the primer coat retains sufficient workability during layup and rolling of the composite laminate. By forcing excessive material into the fiber structure, bondline thickness is automatically reduced to a minimal obtainable thickness
Prolonged Primer Cure	Abraded	-85.2	High	Although post-cure abrasion and chemical treatment of cured resin surfaces has shown to result in a minimal increase in fracture toughness, it cannot provide sufficient surface roughness. In situations where prolonged primer cure has occurred or is unavoidable, use of highly abrasive mechanisms, such as electric disc sanders, must be considered
	As is	-89.2	High	The glossy film of an unabraded primer surface results in adhesive failure and must therefore be avoided during layup. Also, in regions where several layers of laminate are stacked (layup of grid patterns) abrasion prior to application of subsequent material is essential

NOTATION

a	=	Length of crack extension [mm]
a'	=	Length of crack extension in modified beam theory [mm]
A	=	Crack area [mm^2]
a_0	=	Initial length of crack extension [mm]
A_c	=	Cross-sectional area of composite membrane [mm^2]
B	=	Width of composite membrane [mm]
C	=	Compliance [mm/N]
E	=	Total energy [J]
E_{11}	=	Average longitudinal tensile modulus of composite membrane [MPa]
F	=	Force exerted by loading frame [N]
f_c'	=	Compressive strength of concrete [MPa]
G	=	Fracture energy release rate (fracture toughness) [kJ/m^2]
P	=	Work done by external forces [J]
R	=	Fracture resistance [kJ/m^2]
s	=	Average difference in peel distance [mm]
S	=	Tensile force in composite membrane [N]
t	=	Thickness of composite membrane [mm]
U_s	=	Strain energy [J]
w	=	Distributed loading [kN/m]
W_s	=	Energy required to create new surfaces [J]
x	=	Ratio of loading rod displacement over average disbonding length [-]
Δ	=	Vertical displacement of loading rod [mm]
Π	=	Potential energy supplied by internal strain energy and external forces [J]
α	=	Ratio of average difference in peel distance over average disbonding length [-]

θ	=	Angle enclosed by composite membrane and concrete surface [°]
σ	=	Tensile stress in CFRP membrane [MPa]
σ_p	=	Peel stress at concrete/composite interface [MPa]
τ	=	Shear stress at concrete/composite interface [MPa]

APPENDIX A – CALCULATION OF FERR

From Figure A-1, the external loading force can be expressed as:

$$F = S(\sin\theta_1 + \sin\theta_2) \tag{A.1}$$

where

$$\sin\theta_1 = \frac{\Delta}{\sqrt{(a-s)^2 + \Delta^2}} \tag{A.2}$$

and

$$\sin\theta_2 = \frac{\Delta}{\sqrt{(a+s)^2 + \Delta^2}} \tag{A.3}$$

The composite membrane force is then defined as:

$$S = \varepsilon \cdot E_{11} A_c \tag{A.4}$$

with

$$\varepsilon = \frac{\sqrt{(a-s)^2 + \Delta^2} - (a-s) + \sqrt{(a+s)^2 + \Delta^2} - (a+s)}{(a+s) + (a-s)}$$

$$= \frac{\sqrt{(a-s)^2 + \Delta^2} - 2a + \sqrt{(a+s)^2 + \Delta^2}}{2a} \tag{A.5}$$

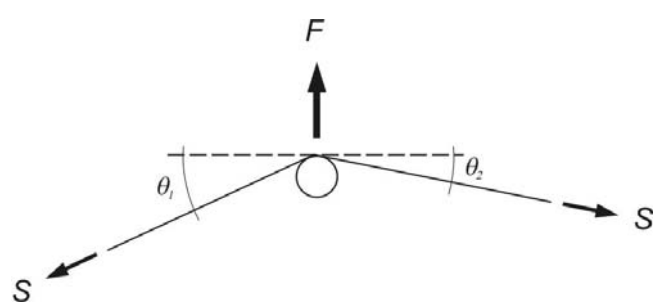

Figure A-1: Force Equilibrium at Point of Load Introduction for Unsymmetrical Peeling

Combining Equations (A.1), (A.4) and (A.5) leads to:

$$F = E_{11}Bt\frac{\sqrt{(a-s)^2+\Delta^2}+\sqrt{(a+s)^2+\Delta^2}-2a}{2a}\cdot\frac{\Delta}{\sqrt{(a-s)^2+\Delta^2}}$$
$$+E_{11}Bt\frac{\sqrt{(a-s)^2+\Delta^2}+\sqrt{(a+s)^2+\Delta^2}-2a}{2a}\cdot\frac{\Delta}{\sqrt{(a+s)^2+\Delta^2}} \qquad \text{(A.6)}$$

$$=E_{11}Bt\frac{\Delta\sqrt{(a-s)^2+\Delta^2}+\Delta\sqrt{(a+s)^2+\Delta^2}-2a\Delta}{2a\sqrt{(a-s)^2+\Delta^2}}$$

$$+E_{11}Bt\frac{\Delta\sqrt{(a-s)^2+\Delta^2}+\Delta\sqrt{(a+s)^2+\Delta^2}-2a\Delta}{2a\sqrt{(a+s)^2+\Delta^2}} \qquad \text{(A.7)}$$

$$=\frac{1}{2}E_{11}Btx\left[2+\frac{\sqrt{(1+\alpha)^2+x^2}}{\sqrt{(1-\alpha)^2+x^2}}+\frac{\sqrt{(1-\alpha)^2+x^2}}{\sqrt{(1+\alpha)^2+x^2}}\right.$$
$$\left.-2\left(\frac{1}{\sqrt{(1-\alpha)^2+x^2}}+\frac{1}{\sqrt{(1+\alpha)^2+x^2}}\right)\right] \qquad \text{(A.8)}$$

To calculate the potential energy stored in the CFRP membrane, Equation (A.8) is integrated with respect to Δ under the condition that peel length, a, remains constant. Hence:

$$U_s=\int F d\Delta\Big|_{a=const}+C \qquad \text{(A.9)}$$

$$=E_{11}Bt\left[\frac{1}{2}\frac{u^2}{a}+\frac{1}{2a}\sqrt{((a+s)^2+\Delta^2)((a-s)^2+\Delta^2)}\right.$$
$$\left.-\sqrt{(a-s)^2+\Delta^2}-\sqrt{(a+s)^2+\Delta^2}\right]+C \qquad \text{(A.10)}$$

The integration constant, C, is found by evaluating Equation (A.10) for the initial condition that:

$$U_s(x=0)=0\ . \qquad \text{(A.11)}$$

It follows that:

$$E_{11}Bt\left[\frac{1}{2a}\sqrt{(a+s)^2(a-s)^2}-\sqrt{(a-s)^2}-\sqrt{(a+s)^2}\right]+C=0 \qquad \text{(A.12)}$$

$$\Rightarrow \quad E_{11}Bt\left[\frac{1}{2a}|a+s|\cdot|a-s|-|a-s|-|a+s|\right]+C=0 \tag{A.13}$$

Since a is always greater than s for the present test configuration, the previous equation can be rewritten as:

$$E_{11}Bt\left[\frac{a^2-s^2}{2a}-2a\right]+C=0 \tag{A.14}$$

$$\Rightarrow \quad C=\frac{3a^2+s^2}{2a}E_{11}Bt \tag{A.15}$$

Upon substitution of Equation (A.15) into Equation (A.10), potential energy stored in the CFRP membrane may be written as:

$$U_s=E_{11}Bt\left[\frac{\Delta^2+s^2+3a^2}{2a}-\sqrt{(a-s)^2+\Delta^2}-\sqrt{(a+s)^2+\Delta^2}\right.$$
$$\left.+\frac{\sqrt{((a+s)^2+\Delta^2)((a-s)^2+\Delta^2)}}{2a}\right] \tag{A.16}$$

Finally, fracture toughness is calculated by differentiating Equation (A.16) with respect to the average peel distance, a, under the condition that membrane displacement, Δ, remains constant, resulting in:

$$G=-\frac{dU}{2Bda}\bigg|_{u=const} \tag{A.17}$$

$$=-\frac{1}{2}E_{11}t\left[3-\frac{\Delta^2+s^2+3a^2}{2a^2}-\frac{\sqrt{((a+s)^2+\Delta^2)((a-s)^2+\Delta^2}}{2a^2}\right.$$
$$+\frac{2(a+s)((a-s)^2+\Delta^2)+2(a-s)((a+s)^2+\Delta^2)}{4a\sqrt{((a+s)^2+u^2)((a-s)^2+\Delta^2)}}$$
$$\left.-\frac{a-s}{\sqrt{(a-s)^2+\Delta^2}}-\frac{a+s}{\sqrt{(a+s)^2+\Delta^2}}\right] \tag{A.18}$$

$$= E_{11}t\left[-\frac{3}{4}+\frac{\left(\frac{\Delta}{a}\right)^2}{4}+\frac{\left(\frac{s}{a}\right)^2}{4}+\frac{\sqrt{\left(1+\frac{s}{a}\right)^2+\left(\frac{\Delta}{a}\right)^2}\sqrt{\left(1-\frac{s}{a}\right)^2+\left(\frac{\Delta}{a}\right)^2}}{4}\right.$$

$$-\frac{\left(1+\frac{s}{a}\right)\left[\left(1-\frac{s}{a}\right)^2+\left(\frac{\Delta}{a}\right)^2\right]+\left(1-\frac{s}{a}\right)\left[\left(1+\frac{s}{a}\right)^2+\left(\frac{\Delta}{a}\right)^2\right]}{4\sqrt{\left(1+\frac{s}{a}\right)^2+\left(\frac{\Delta}{a}\right)^2}\sqrt{\left(1-\frac{s}{a}\right)^2+\left(\frac{\Delta}{a}\right)^2}}$$

$$\left.+\frac{1-\frac{s}{a}}{2\sqrt{\left(1-\frac{s}{a}\right)^2+\left(\frac{\Delta}{a}\right)^2}}+\frac{1+\frac{s}{a}}{2\sqrt{\left(1+\frac{s}{a}\right)^2+\left(\frac{\Delta}{a}\right)^2}}\right] \tag{A.19}$$

Substituting $x = \Delta/a$ and $\alpha = s/a$ into Equation (A.19) results in:

$$G = E_{11}t\left[-\frac{3}{4}+\frac{x^2}{4}+\frac{\alpha^2}{4}+\frac{\sqrt{(1+\alpha)^2+x^2}\sqrt{(1-\alpha)^2+x^2}}{4}\right.$$

$$-\frac{(1+\alpha)((1-\alpha)^2+x^2)+(1-\alpha)((1+\alpha)^2+x^2)}{4\sqrt{(1+\alpha)^2+x}\sqrt{(1-\alpha)^2+x^2}}$$

$$\left.+\frac{1-\alpha}{2\sqrt{(1-\alpha)^2+x^2}}+\frac{1+\alpha}{2\sqrt{(1+\alpha)^2+x^2}}\right] \tag{A.20}$$

$$= \frac{1}{4}E_{11}t\left[x^2+\alpha^2-3+\sqrt{(1+\alpha)^2+x^2}\sqrt{(1-\alpha)^2+x^2}\right.$$

$$+\frac{(1+\alpha)(2-\sqrt{(1-\alpha)^2+x^2})}{\sqrt{(1+\alpha)^2+x^2}}$$

$$\left.+\frac{(1-\alpha)(2-\sqrt{(1+\alpha)^2+x^2})}{\sqrt{(1-\alpha)^2+x^2}}\right] \tag{A.21}$$

APPENDIX B – SYSTEM STABILITY

As derived elsewhere [10], stable crack propagation demands that:

$$\frac{dG}{dA} \leq \frac{dR}{dA} \tag{B.1}$$

From Equation (7.8) for the case of symmetric peeling, i.e. $\alpha = s/a = 0$, fracture energy release rate may be expressed by:

$$G = E_{11}t\left(\frac{x^2}{2} + \frac{1}{\sqrt{x^2+1}} - 1\right) \tag{B.2}$$

Substituting $x = \Delta/a$ and taking the derivative with respect to *a* results in:

$$\left.\frac{dG}{da}\right|_{\alpha=0} = Et\left[-\frac{\Delta^2}{a^3} + \frac{\Delta^2}{a^3}\cdot\frac{1}{\left(1+\left(\frac{\Delta}{a}\right)^2\right)^{\frac{3}{2}}}\right] \tag{B.3}$$

$$= Et\frac{\Delta^2}{a^3}\left[-1 + \frac{1}{\left(1+\left(\frac{\Delta}{a}\right)^2\right)\sqrt{1+\left(\frac{\Delta}{a}\right)^2}}\right] \tag{B.4}$$

Upon re-substitution of $x = \frac{\Delta}{a}$, it follows that:

$$\left.\frac{dG}{da}\right|_{\alpha=0} = Et\left[\frac{x^2}{a}\left(-1 + \frac{1}{\left(1+x^2\right)\sqrt{1+x^2}}\right)\right] \tag{B.5}$$

Hence, given the fact that $(1+x^2) > 1$, $\sqrt{1+x^2}\,1$, and $a > 0$:

$$\left.\frac{dG}{da}\right|_{\alpha=0} < 0 \tag{B.6}$$

Accordingly, for the cast of symmetrical peeling, the system experiences stable fracture. To investigate the case of unsymmetrical peeling, the change of *G* with respect to crack extension, *a*, was graphed in Figure B-1. It may be observed that the slope of the graph

becomes steeper, i.e. more negative, as the difference in crack extension, *s*, increases. It may thus be concluded that the system remains stable for both symmetric and unsymmetrical peeling. Nonetheless, a rising or near-constant *R*-curve of the fractured material remains a precondition for validity of this conclusion. As shown in Figure B-2, large variations in the *R*-curve may result in local instability and so-called "jumping" of the crack. This phenomenon may hence be expected in situations when a crack propagates from regions of high aggregate exposure to regions of high cement paste content.

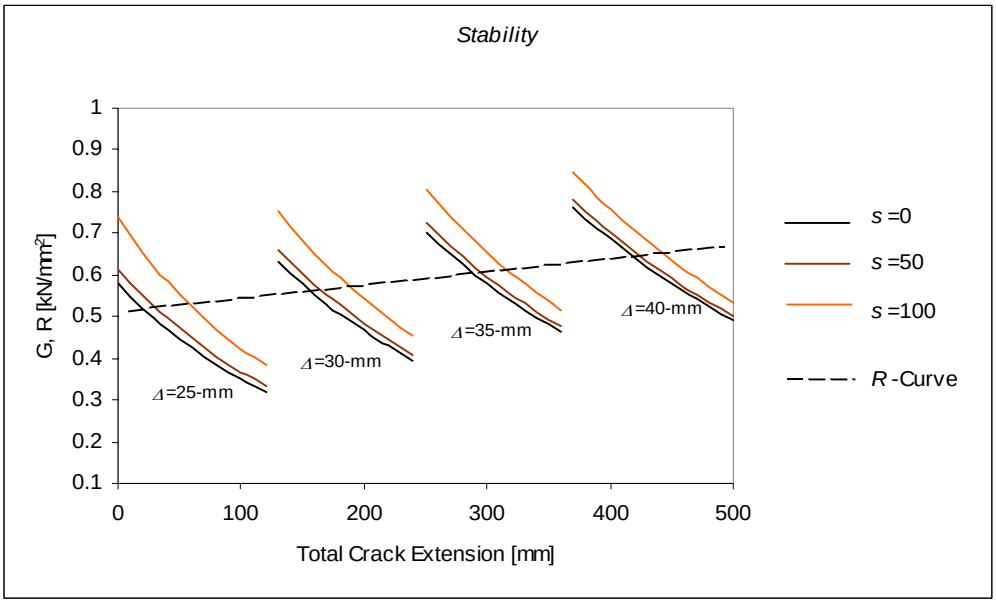

Figure B-1: Stability for Various Levels of Peeling Asymmetry

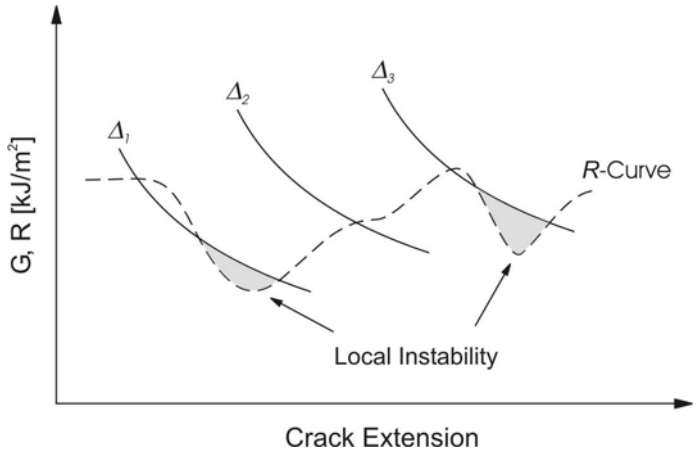

Figure B-2: Local Instability due to Variation in Fracture Resistance

APPENDIX C - EVALUATION OF MATERIAL PROPERTIES

CONCRETE COMPRESSIVE STRENGTH

As preparation and testing of concrete specimens continued over a period of several months, concrete compressive strength was monitored throughout progression of the experimental study. During the casting process of the first 70 specimens, one concrete test cylinder was cast to represent a set of seven concrete prisms. Once a set of specimens was tested, compressive strength of the corresponding compression cylinder was determined. The general layout of the test program shown in Figure C-1. Numerical results of the study are given in Table C-1.

It can be noted that average concrete compressive strength did not vary during the course of testing. Herein, specimen 7 must be considered an outlier.

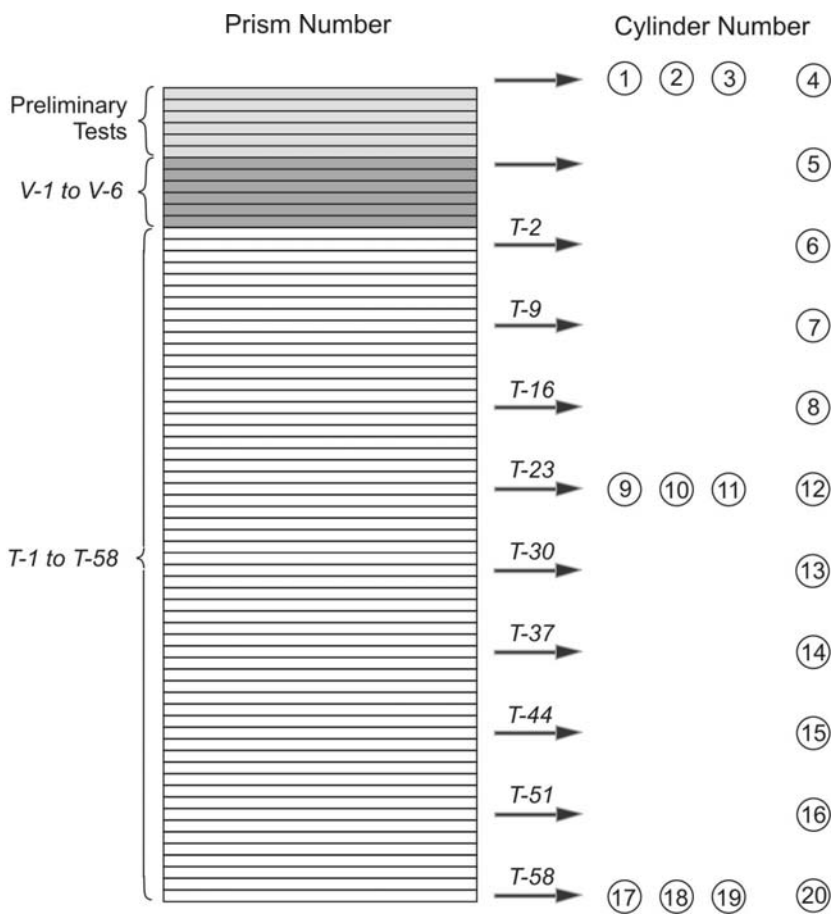

Figure C-1: Specimen Layout for Evaluation of Concrete Properties

Table C-1: Results of Concrete Study

CYLINDER #	TEST DATE	TEST TYPE	f_c' [MPa]	COMMENTS
1	08/02/01	Compression	5,940	21-day strength
2	08/09/01	Compression	5,430	28-day strength
3	08/09/01	Compression	5,160	28-day strength
4		Split Ring		
5	11/19/01	Compression	5,340	
6	-†	-	-	-
7	04/12/02	Compression	7,710	
8		Compression		
9	08/02/01	Compression	5,480	21-day strength
10	08/09/01	Compression	5,500	28-day strength
11	08/09/01	Compression	5,570	28-day strength
12		Split Ring		
13		Compression		
14		Compression		
15		Compression		
16		Compression		
17	08/02/01	Compression	5,370	21-day strength
18	08/09/01	Compression	5,820	28-day strength
19	08/09/01	Compression	5,870	28-day strength
20		Split Ring		

†: *Omitted during casting*

MATERIAL PROPERTIES OF CFRP

An extensive material test program was performed to evaluate the average longitudinal tensile modulus, E_{11}, average peel width, B, and thickness, t, of each composite membrane. Results of this analysis were used to evaluate Equation (7.11) to compute the FERR plots shown in Appendix E. Herein, following each peel test, the remaining regions of bonded material were peeled off manually and average peel width was determined from measurements taken at three equidistant locations. Further, tensile test coupons were cut from the initially unbonded CFRP material. Following ASTM D3039, a minimum of three coupons per specimen was tested as shown in Figure C-2.

As may be seen, load-displacement graphs generally display notable differences in stiffness among test coupons. This may be due to the unavoidable variation in material infiltration that is generally linked to the hand layup procedure. Also, erroneous thickness measurements are more likely to occur for materials that employ transversely stitched fiber tows, as this causes a wavy texture, i.e. locations that are not necessarily representative of the actual material thickness. The tensile modulus for each set of tensile test coupons is given in the lower right corner of each graph.

Finally, it is noteworthy that the CFRP tensile coupons were generally not tested to failure. On specimens that experienced failure, ultimate strain was about 1.5 to 1.8%, while the remaining tests were terminated at a strain of about 1.0%.

Figure C-3: Evaluation of Tensile Properties

LOAD-DISPLACEMENT GRAPHS

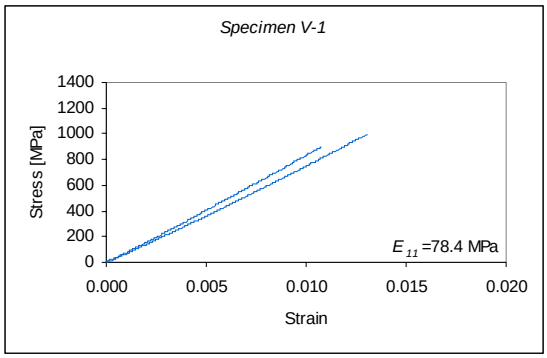

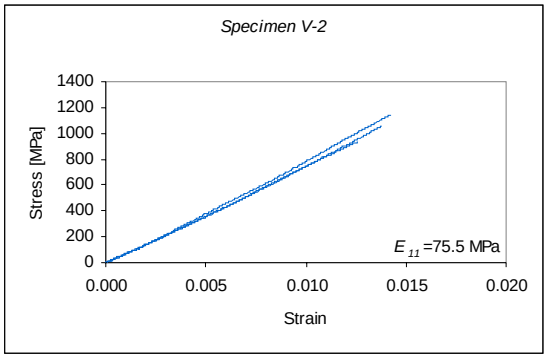

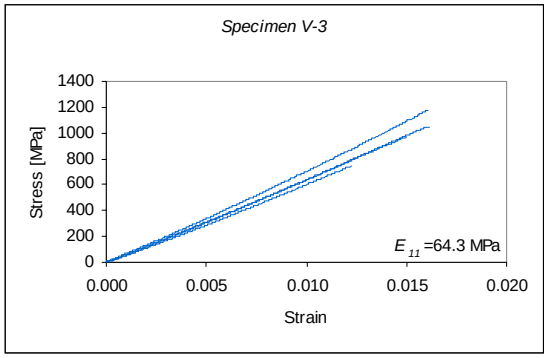

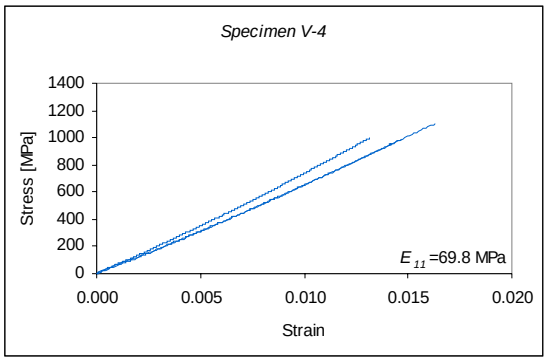

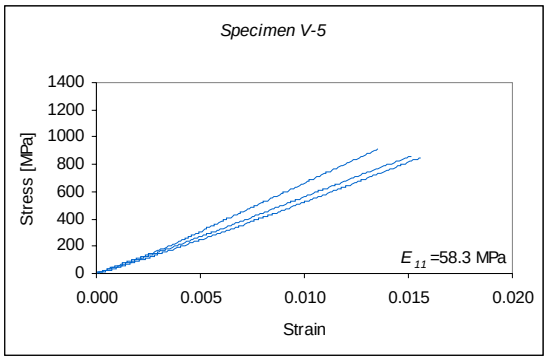
Specimen V-5
Stress [MPa]
Strain
E 11 =58.3 MPa

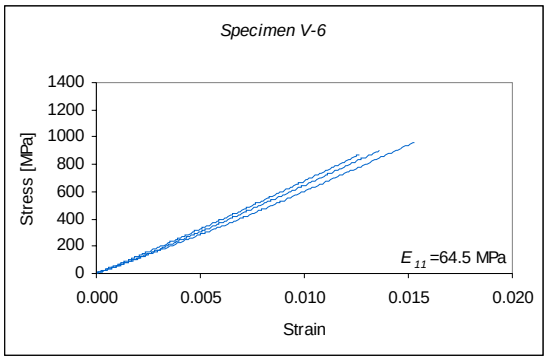
Specimen V-6
Stress [MPa]
Strain
E 11 =64.5 MPa

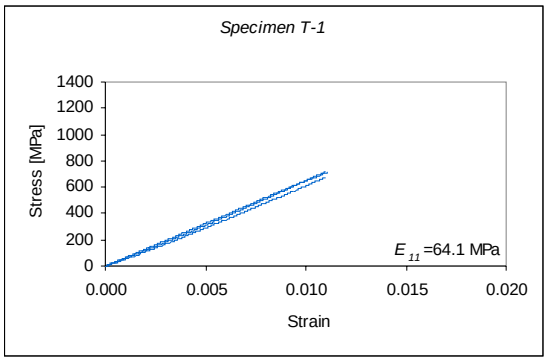
Specimen T-1
Stress [MPa]
Strain
E 11 =64.1 MPa

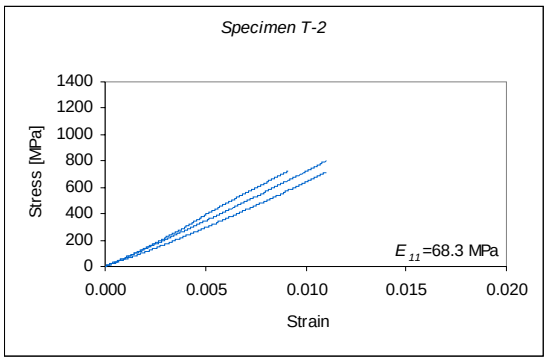
Specimen T-2
Stress [MPa]
Strain
E 11 =68.3 MPa

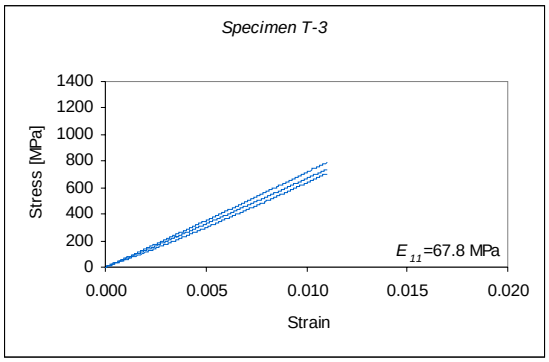
Specimen T-3
Stress [MPa]
Strain
E 11 =67.8 MPa

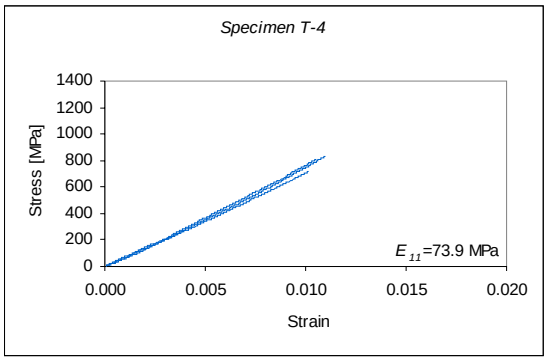
Specimen T-4
Stress [MPa]
Strain
E 11 =73.9 MPa

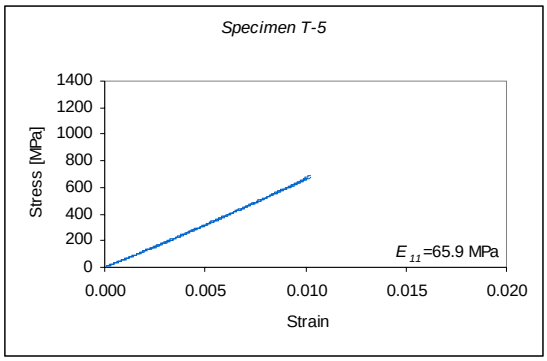
Specimen T-5
Stress [MPa]
Strain
E 11 =65.9 MPa

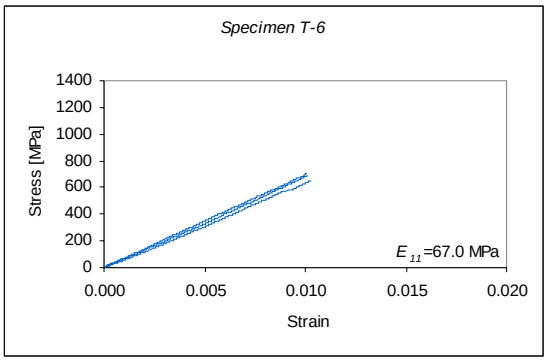
Specimen T-6
Stress [MPa]
Strain
E 11 =67.0 MPa

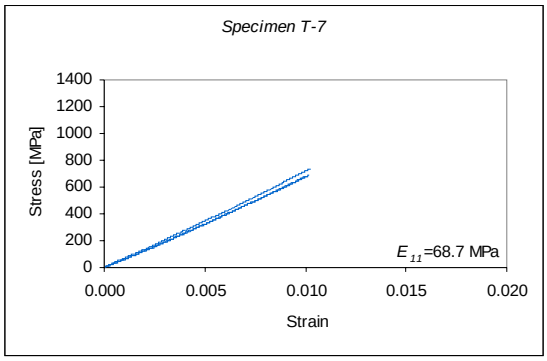
Specimen T-7
Stress [MPa]
Strain
E 11=68.7 MPa

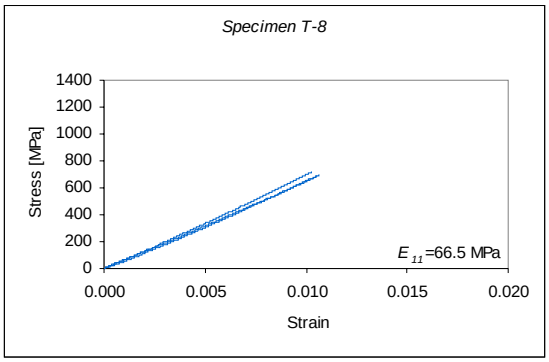
Specimen T-8
Stress [MPa]
Strain
E 11=66.5 MPa

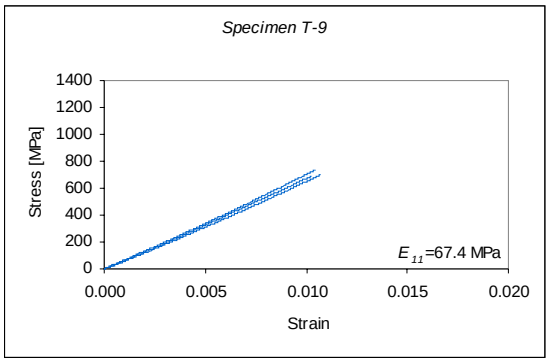
Specimen T-9
Stress [MPa]
Strain
E 11=67.4 MPa

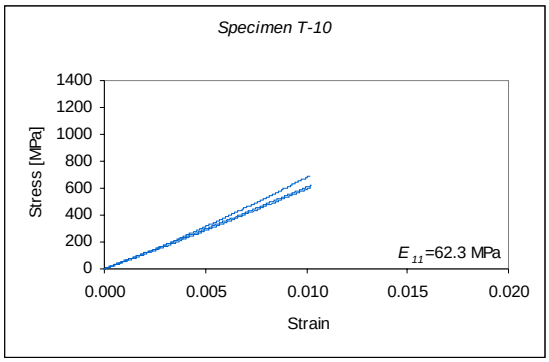
Specimen T-10
Stress [MPa]
Strain
E 11=62.3 MPa

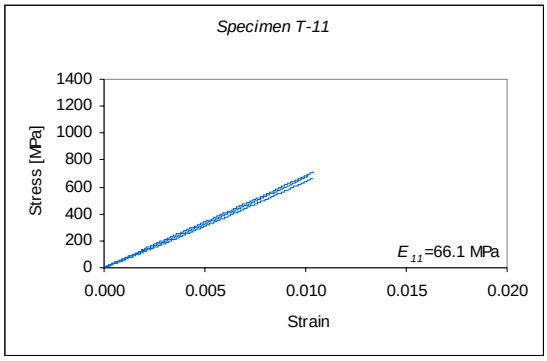
Specimen T-11
Stress [MPa]
Strain
E 11=66.1 MPa

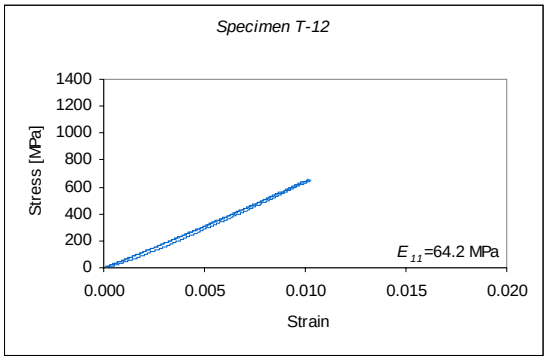
Specimen T-12
Stress [MPa]
Strain
E 11=64.2 MPa

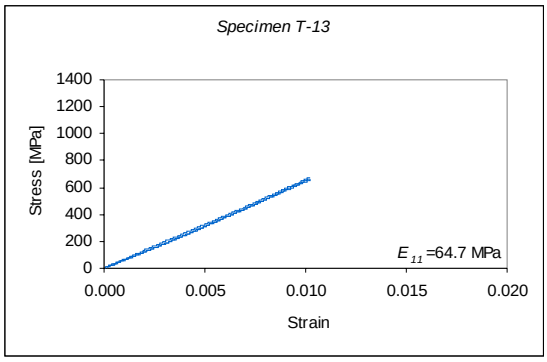
Specimen T-13
Stress [MPa]
Strain
E 11=64.7 MPa

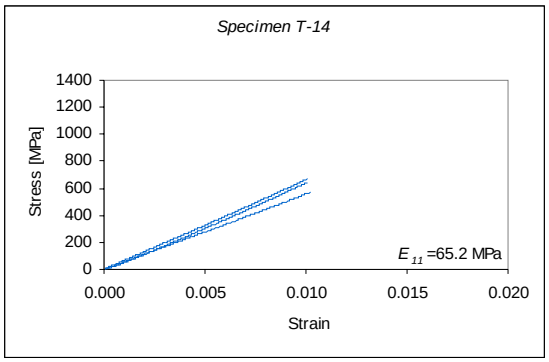
Specimen T-14
Stress [MPa]
Strain
E 11=65.2 MPa

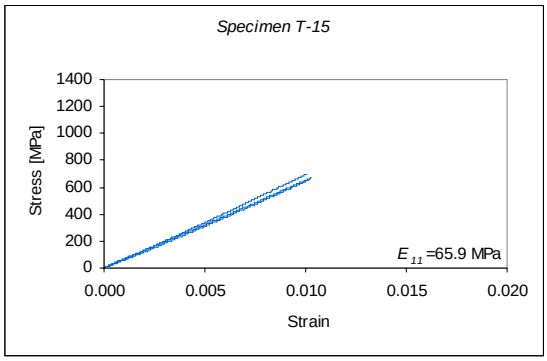
Specimen T-15
Stress [MPa]
Strain
E 11 =65.9 MPa

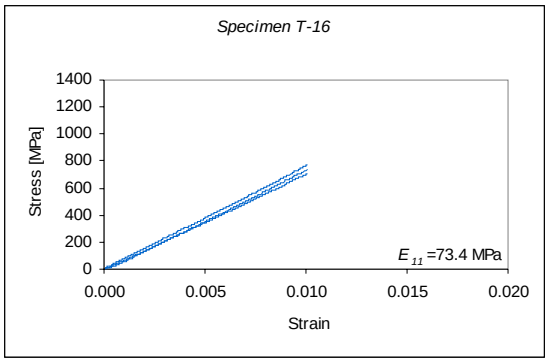
Specimen T-16
Stress [MPa]
Strain
E 11 =73.4 MPa

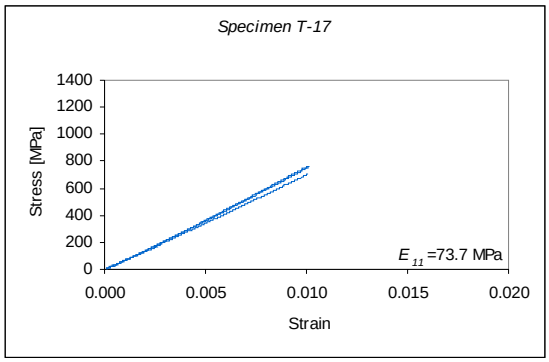
Specimen T-17
Stress [MPa]
Strain
E 11 =73.7 MPa

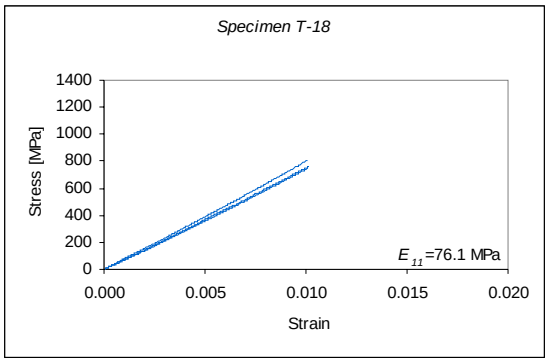
Specimen T-18
Stress [MPa]
Strain
E 11 =76.1 MPa

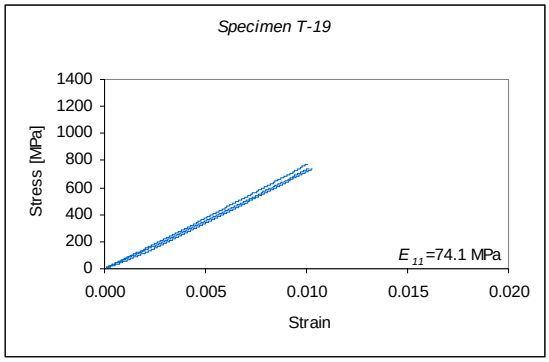
Specimen T-19
Stress [MPa]
Strain
E 11 =74.1 MPa

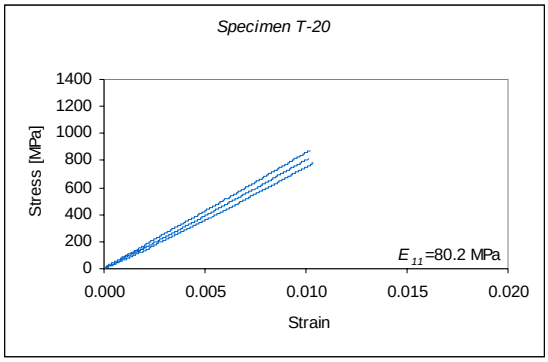
Specimen T-20
Stress [MPa]
Strain
E 11 =80.2 MPa

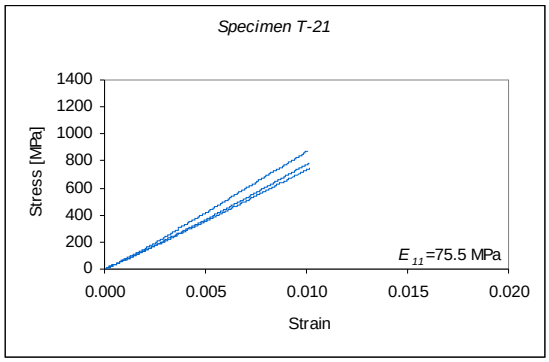
Specimen T-21
Stress [MPa]
Strain
E 11 =75.5 MPa

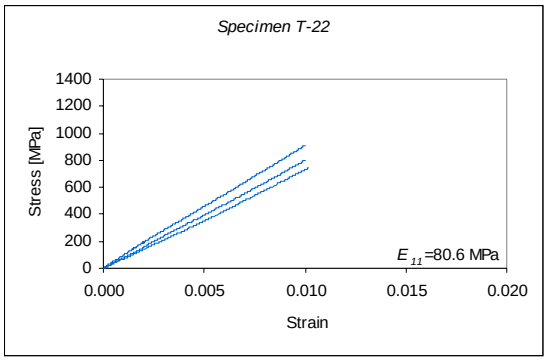
Specimen T-22
Stress [MPa]
Strain
E 11 =80.6 MPa

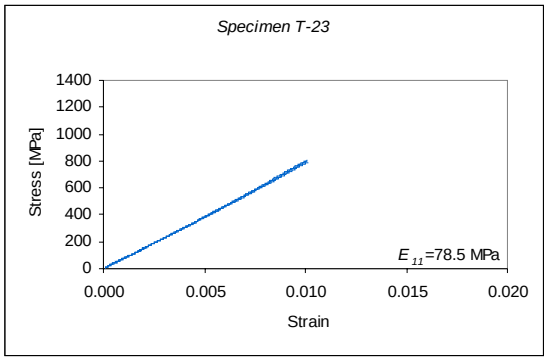
Specimen T-23
Stress [MPa]
1400
1200
1000
800
600
400
200
0
0.000
0.005
0.010
0.015
0.020
Strain
E 11=78.5 MPa

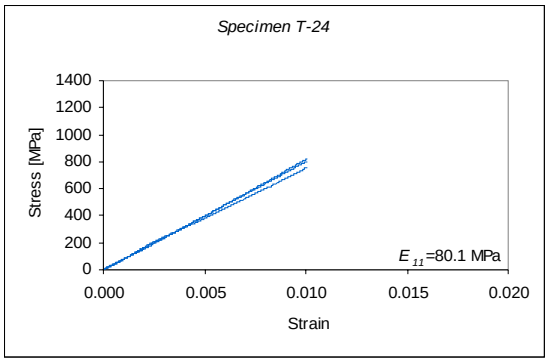
Specimen T-24
Stress [MPa]
1400
1200
1000
800
600
400
200
0
0.000
0.005
0.010
0.015
0.020
Strain
E 11=80.1 MPa

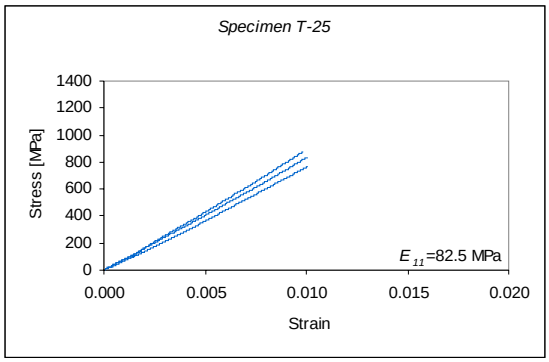
Specimen T-25
Stress [MPa]
1400
1200
1000
800
600
400
200
0
0.000
0.005
0.010
0.015
0.020
Strain
E 11=82.5 MPa

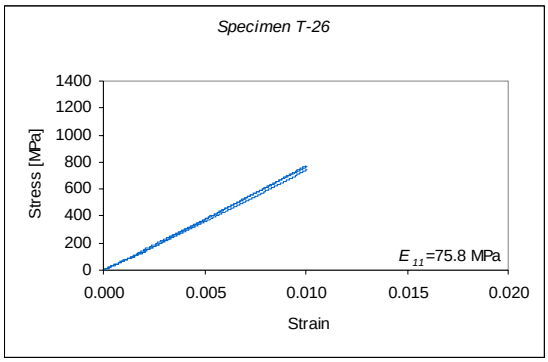
Specimen T-26
Stress [MPa]
1400
1200
1000
800
600
400
200
0
0.000
0.005
0.010
0.015
0.020
Strain
E 11=75.8 MPa

APPENDIX D - SPECIMEN MORPHOLOGY

To assess the effect of variations in surface morphology on fracture toughness, digital images of the concrete surface were taken at four equally spaced locations along the treated specimen surface, prior to priming. These images are presented in Figures D-1 to D-4. As may be noted, morphology varies significantly among specimens. While certain regions display a high degree of aggregate, others have retained most of the weak cement paste. Although these regions had sufficient strength to withstand abrasion, they must be assumed substantially lower in terms of fracture resistance when compared to regions of high aggregate exposure.

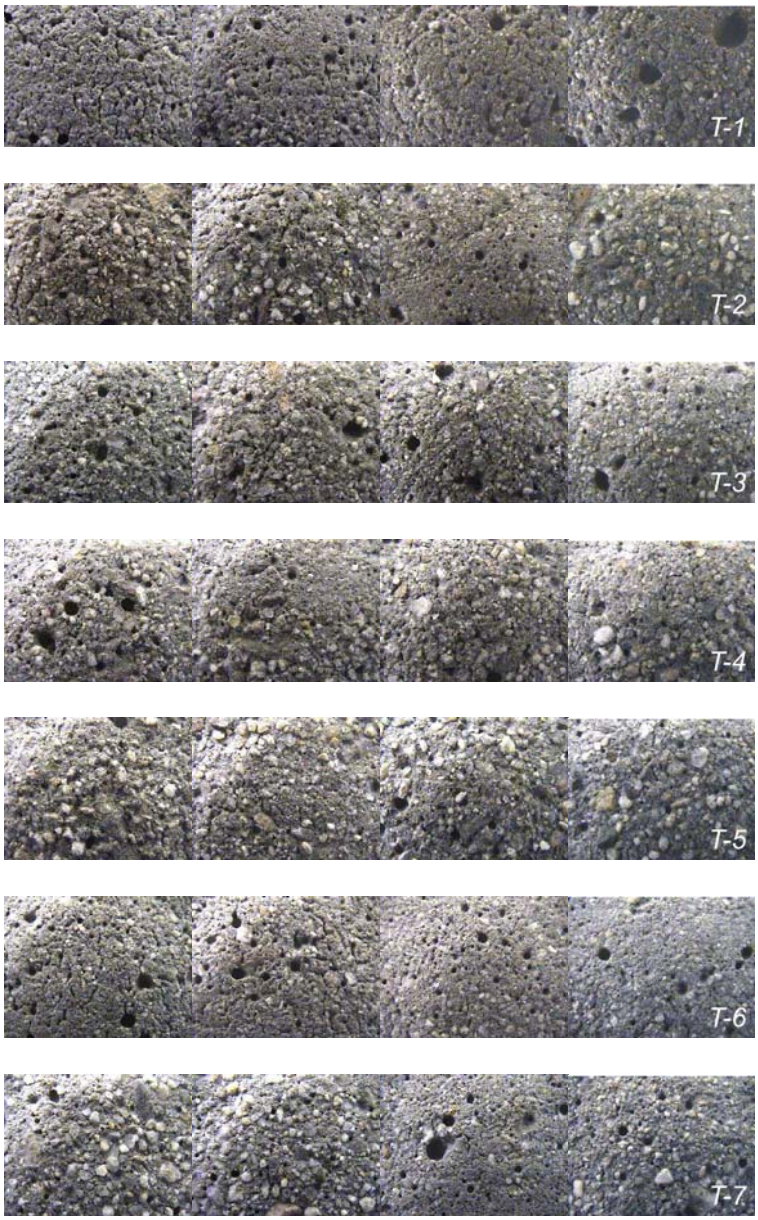

Figure D-1: Surface Morphology of Specimens T-1 to T-7

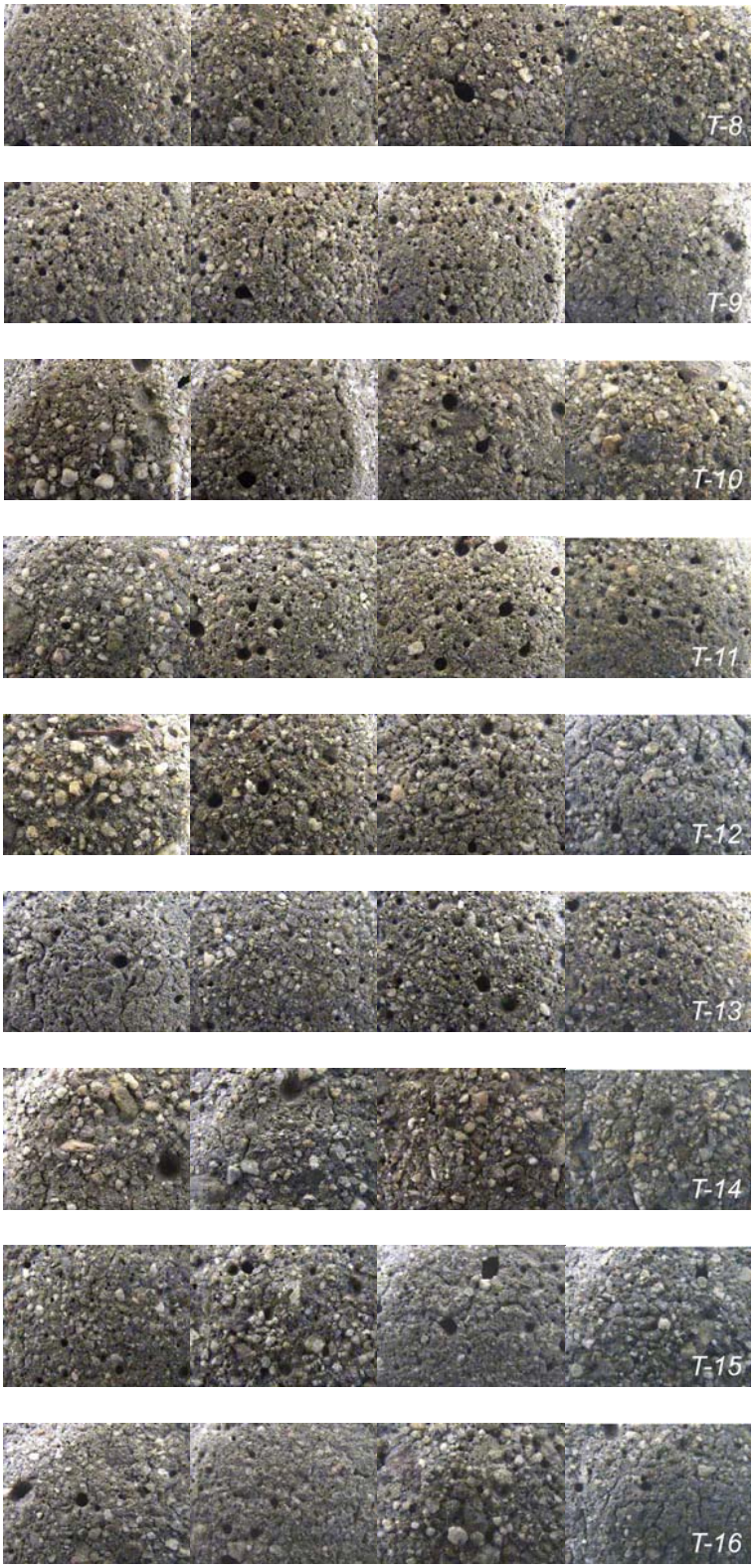

Figure D-2: Surface Morphology of Specimens T-8 to T-16

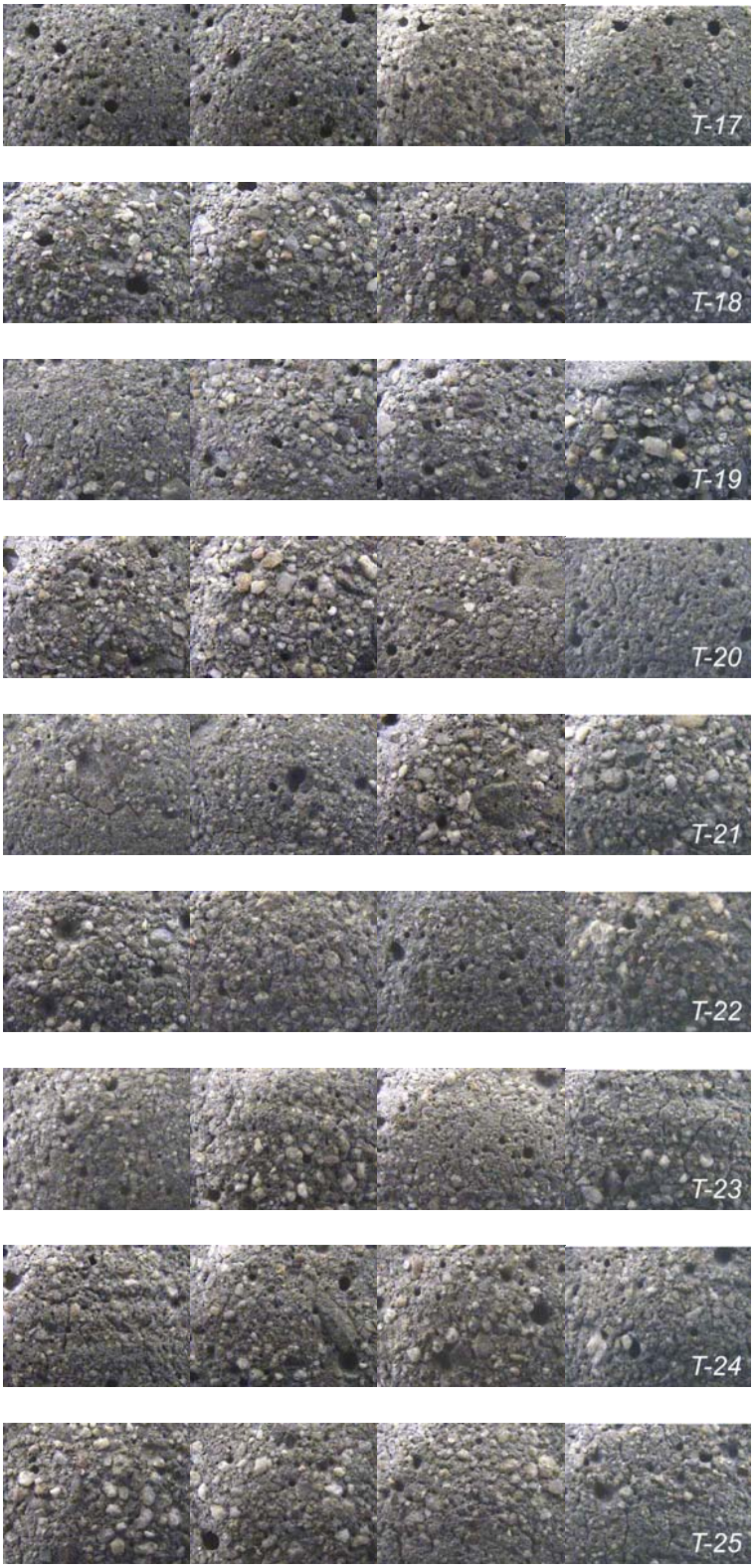

Figure D-3: Surface Morphology of Specimens T-17 to T-25

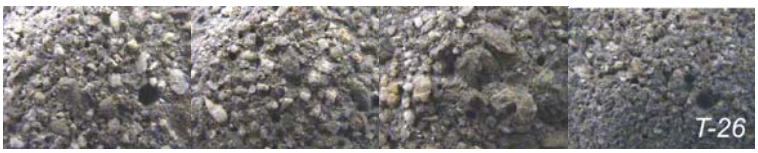

Figure D-4: Surface Morphology of Specimen T-26

APPENDIX E - FERR PLOTS

In the following, plots of fracture energy release rate versus total crack extension for specimens *T-1* to *T-26* are presented. Herein, the defect category of each specimen is given in the graph. Similar to Chapter 8, each data point represents a change in potential energy of the CFRP membrane with respect to an individual crack extension at that specific instance. Finally, it is noteworthy that the scale on plots *T-8* to *T-13* differs from that of the remaining graphs, due to a significant decrease in fracture toughness for these specimens.

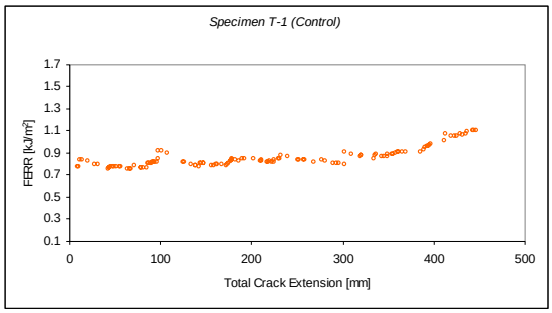

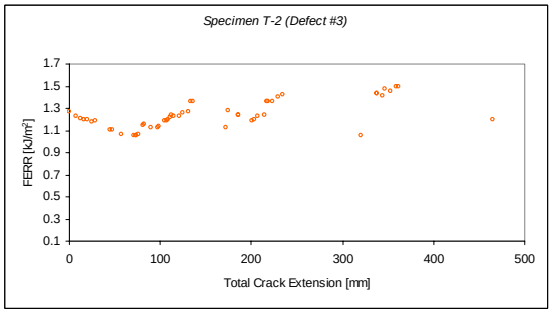

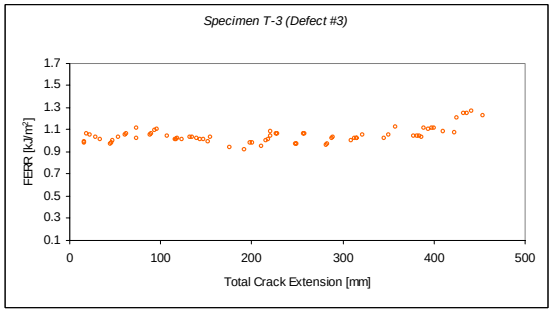

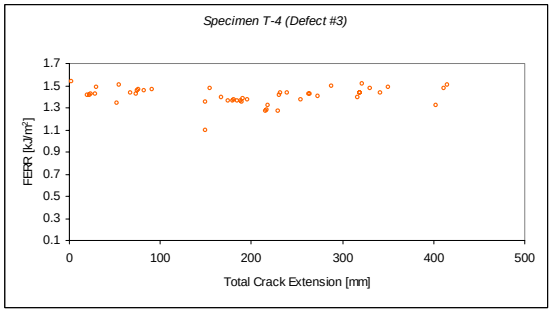

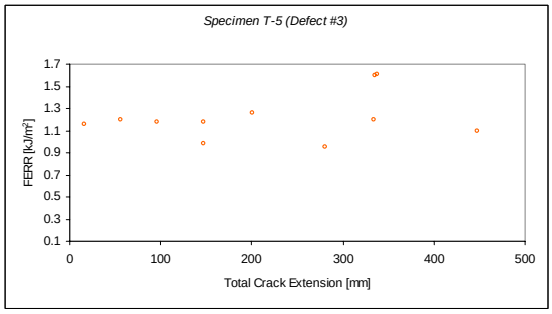

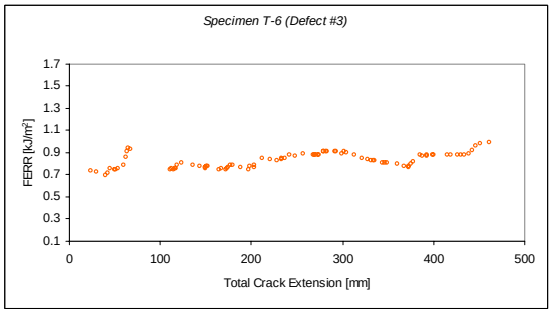

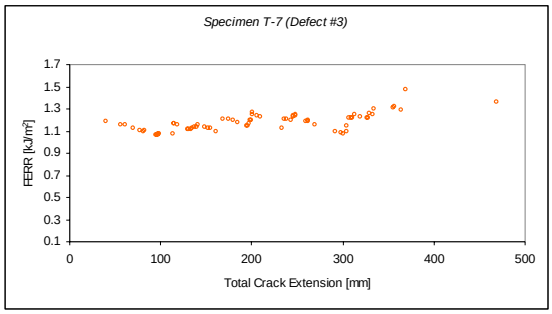
Specimen T-7 (Defect #3)
FERR [kJ/m²]
Total Crack Extension [mm]

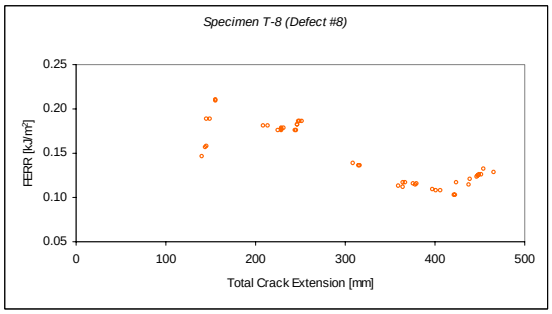
Specimen T-8 (Defect #8)
FERR [kJ/m²]
Total Crack Extension [mm]

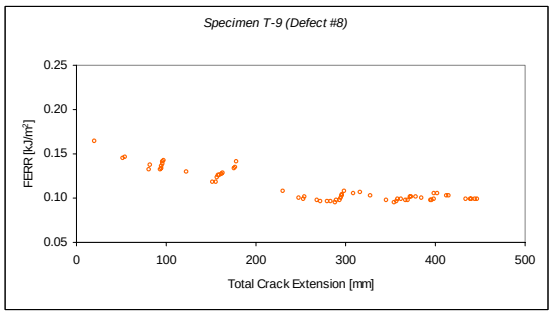
Specimen T-9 (Defect #8)
FERR [kJ/m²]
Total Crack Extension [mm]

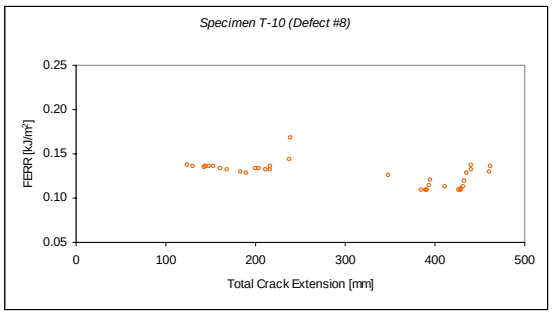
Specimen T-10 (Defect #8)
FERR [kJ/m²]
Total Crack Extension [mm]

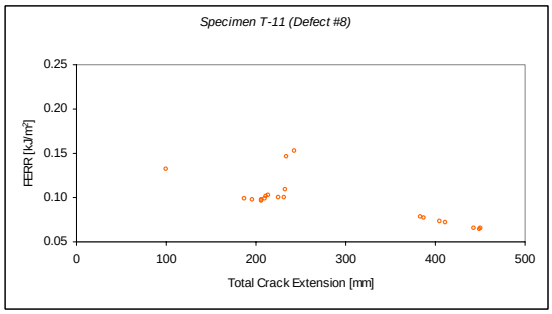
Specimen T-11 (Defect #8)
FERR [kJ/m²]
Total Crack Extension [mm]

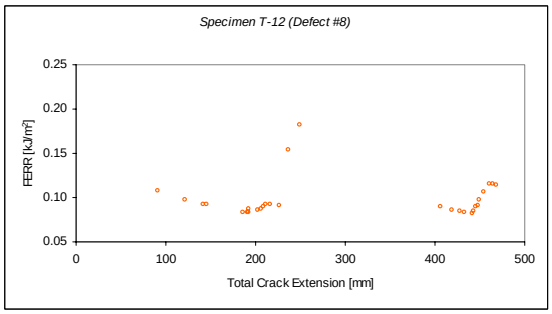
Specimen T-12 (Defect #8)
FERR [kJ/m²]
Total Crack Extension [mm]

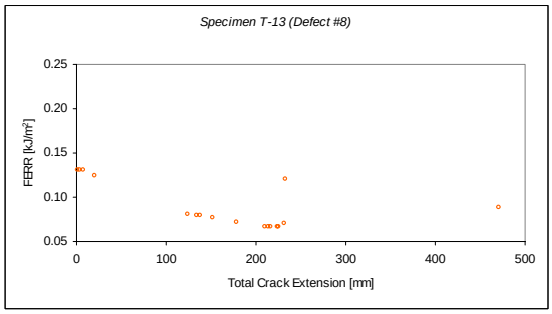
Specimen T-13 (Defect #8)
FERR [kJ/m²]
Total Crack Extension [mm]

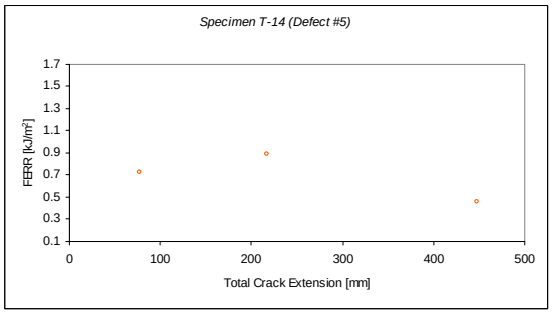
Specimen T-14 (Defect #5)
FERR [kJ/m²]
Total Crack Extension [mm]

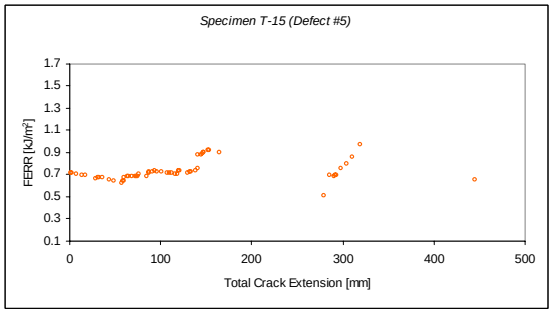
Specimen T-15 (Defect #5)
FERR [kJ/m²]
Total Crack Extension [mm]

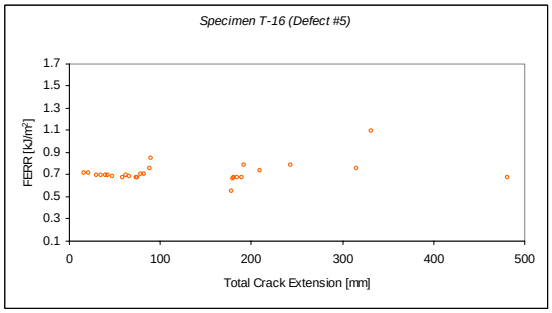
Specimen T-16 (Defect #5)
FERR [kJ/m²]
Total Crack Extension [mm]

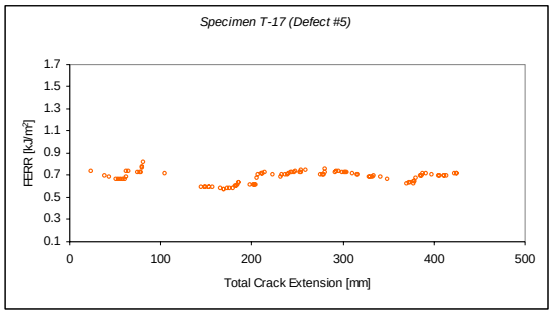
Specimen T-17 (Defect #5)
FERR [kJ/m²]
Total Crack Extension [mm]

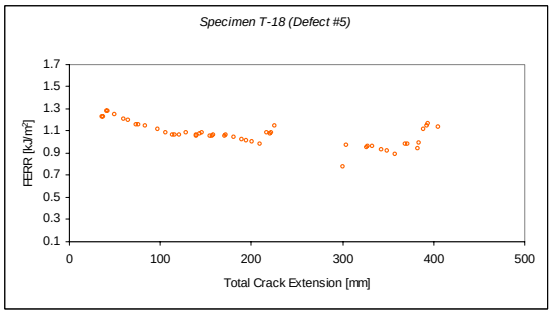
Specimen T-18 (Defect #5)
FERR [kJ/m²]
Total Crack Extension [mm]

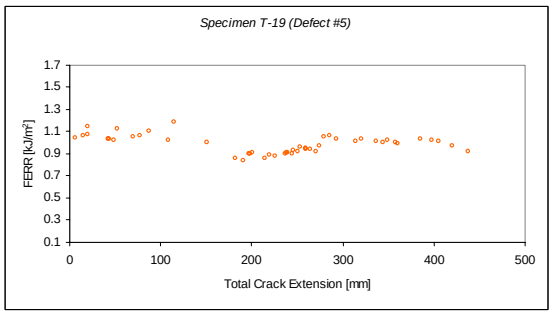
Specimen T-19 (Defect #5)
FERR [kJ/m²]
Total Crack Extension [mm]

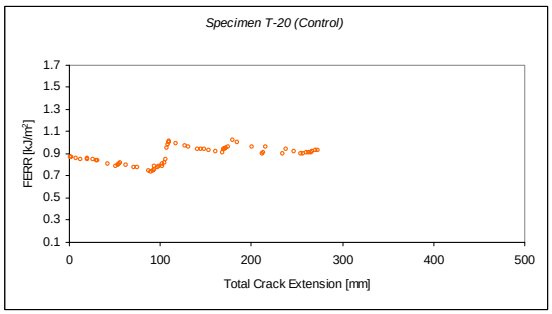
Specimen T-20 (Control)
FERR [kJ/m²]
Total Crack Extension [mm]

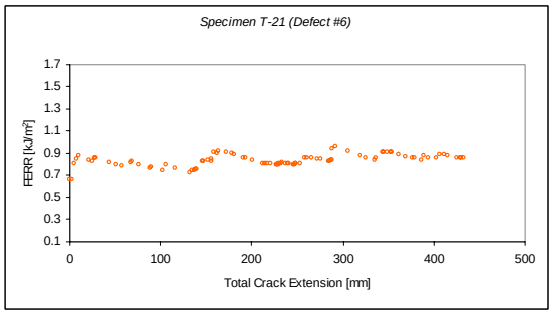
Specimen T-21 (Defect #6)
FERR [kJ/m²]
Total Crack Extension [mm]

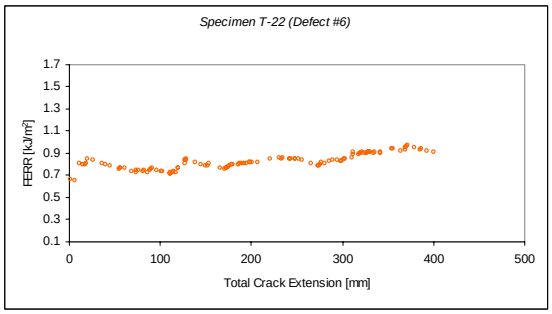
Specimen T-22 (Defect #6)
FERR [kJ/m²]
Total Crack Extension [mm]

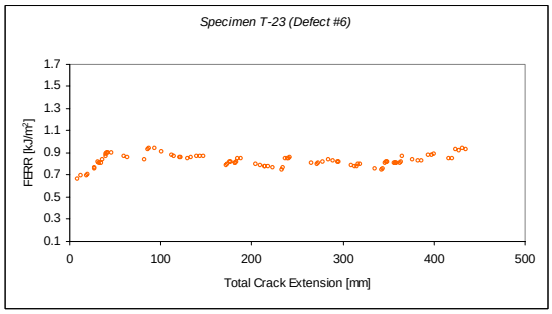
Specimen T-23 (Defect #6)
FERR [kJ/m²]
Total Crack Extension [mm]

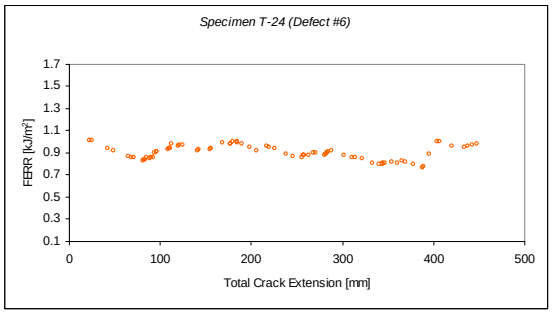
Specimen T-24 (Defect #6)
FERR [kJ/m²]
Total Crack Extension [mm]

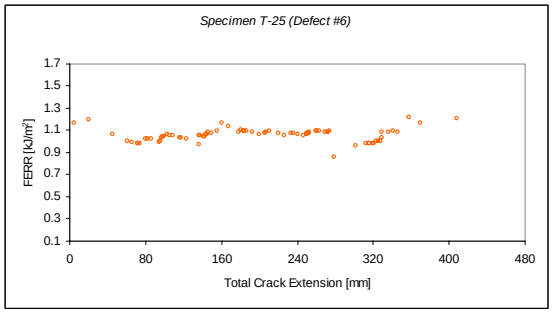
Specimen T-25 (Defect #6)
FERR [kJ/m²]
Total Crack Extension [mm]

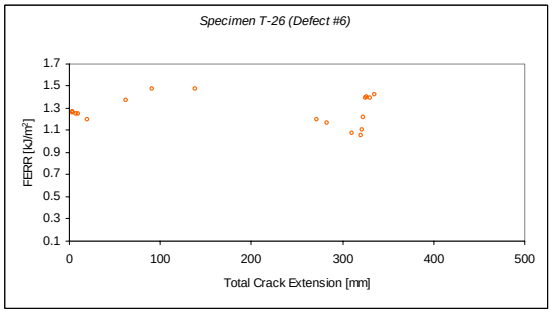
Specimen T-26 (Defect #6)
FERR [kJ/m²]
Total Crack Extension [mm]

GLOSSARY

A-scan	Ultrasonic data representation using instantaneous data that is displayed on a horizontal baseline (distance or time of flight) versus a vertical deflection (amplitude).
Adherent	A body that is held to another body usually by an adhesive.
Adhesive	Substance capable of holding two materials together by surface attachment. Can be a film, paste of liquid.
Adhesive Failure	Progression of crack front within the adhesive.
Attenuation	Factor representing a decrease in signal intensity with distance. Expressed in decibels (dB) per unit distance.
Autoclave	Automated post-cure assembly to attain higher degrees of resin cure.
Black light	Electromagnetic radiation in the range of 315 to 400-nm.
Bond strength	The amount of adhesion between two surfaces.
Bondable Surface	Surface containing a partially cured primer coat.
Boroscope	Industrial scope that transmits images from inaccessible regions for visual inspection. They can be flexible or rigid in nature.
B-scan	Ultrasonic data representations along a line scan that represent one particular cross-section of a part. Interior features can be displayed in their approximate length.
BVID	Barely visible impact damage.
Capillary action	Movement of liquids within the spaces of a porous material due to forces of adhesion, cohesion, and surface tension.
Catalyst	A substance that changes the rate of chemical reaction without itself undergoing permanent change in composition.
CCD	Charge coupled device, used to obtain electronic signals in modern video cameras.
CFRP	Carbon Fiber Reinforced Polymer
Coherence	Multiple events, i.e. emission of light rays that occur at an identical time instant (temporal coherence) while originating from the same location in space (spatial coherence).
Cohesive Failure	Progression of crack front within bulk material (adherent).

Cold bond	Separation within a material or at the interface between two adjacent materials which are in intimate contact but possess no capability of stress transfer.
Collimated light	Plane wave front comprised of coherent light.
Compliance	Amount of deflection of a body given an external loading (inverse of stiffness).
Compression wave	A wave in which the direction of particle motion coincides with direction of wave propagation.
Conduction	Heat transfer through interaction of atoms and molecules, mostly encountered in solids.
Convection	Heat transfer in fluids by mixing of molecules.
Cryogenics	Chemicals used to obtain extremely low temperatures at around -180°C, i.e. liquid nitrogen.
CSC	Curved-surface-correction feature applied in ultrasonic test units for sound path correction when inspecting around the circumference of a curved surface.
C-scan	Ultrasonic data representation that provides a plan view of material constitution, including internal discontinuities.
DAC	Distance amplitude correction in ultrasonic units that automatically adjusts amplitude in regions of varying signal intensity.
Debond	An initially unbonded or nonadhered region between two adherents. Also used to describe a separation at the fiber-matrix interface. In the construction industry, debond and delamination are sometimes used interchangeably when referring to separations at the concrete-composite interface.
Decibel (dB)	Logarithmic scale expressing relative amplitude or intensity of ultrasonic signals.
Degradation	Deleterious change in physical properties or appearance.
Delamination	Separation of the layers of material in a laminate, either local or covering a wide area.
Delay line	Column of material such as Plexiglas that behaves similar to a water path and allows a shift of the initial ultrasonic pulse.
Disbond	An area within an initially bonded interface between two adherents in which adhesion failure or separation has occurred.
Displacement Control	Loading of a body using controlled variation in displacement.

DMTA	Dynamic mechanical thermal analysis. Provides information on presence of solvents, changes in structure and chemical reactions.
DSC	Differential scanning calorimetry. Detects loss of solvents and other volatiles.
Dye penetrant	Visible or fluorescent solution that seeps into porous surfaces.
Electrical conductivity	Readability of a material to allow flow of electric current.
Emissivity	Ability to radiate energy relative to a perfect radiator (blackbody) with values ranging from zero to one.
Emulsifier	Liquid that interacts with an oily substance to make it water-soluble.
ERSG	Electrical Resistance Strain Gauge
FERR	Fracture energy release rate.
FPS	Frames per second.
Framegrabber	Computer-controlled acquisition device used to digitize single or multiple video images.
FRP	Fiber Reinforced Polymer
Ferromagnetic	Materials that are strongly attracted to a magnet and can become magnetized, such as iron.
Fiberscope	Device that delivers light through a fiberoptic bundle to a CCD unit that converts it into an electric signal.
Fracture Toughness	See *FERR*
Galvanic corrosion	Galvanic reaction between metals and conductive carbon fibers, resulting in degradation of matrix and metal.
Half-life	Measure of the average lifetime of a radioactive substance, where one half-life represents the time required for one half of any given quantity of the substance to decay.
Heat mirror	A perfect light reflector with extremely low emissivity.
Hydrolysis	Process of degradation that generically includes the splitting of chemical bonds and the addition of water.
Hybrid	The combination of two materials of different origin or composition.
Inclusion	Mechanical discontinuity occurring within a material, consisting of a solid, encapsulated material.

Interface	Boundary between two different, physically distinguishable media.
Kissing bond	See *cold bond*
Lamb wave	Surface waves that travel between two parallel surfaces by means of elliptical particle motion, such as inside a plate.
Laminate	A product made by stacking of multiple layers of unidirectional fibers or oriented fiber configurations embedded in a resin matrix.
Load Control	Loading of a body using controlled variation in external force.
Longitudinal wave	See *compression wave*
LVDT	Linear variable differential transformer
Membrane	Thin component with significantly higher longitudinal stiffness compared to its flexural stiffness.
MEK	Methyl Ethyl Peroxide
MEKP	Methyl Ethyl Ketone Peroxide
Mode conversion	Phenomenon where wave modes are altered due to refraction at material boundaries.
Morphology	Appearance and texture of a surface
NDE	Non-destructive evaluation. Methodology encompassing the use of non-destructive testing (NDT) techniques with subsequent assessment on severity in view of performance or integrity of an entire structure or components thereof.
NDI	Non-destructive inspection, often synonymous to *NDT*.
NDT	Non-destructive testing. A process that does not result in any damage or change to the material or part under examination and through which the presence of conditions or discontinuities can be detected.
Peel-off	Experimental process resulting in separation of two initially bonded materials.
Photons	Particles composing light and other forms of electromagnetic radiation, possessing no mass or charge.
Piezoelectric crystal	Material that transforms electrical energy into mechanical energy and vice versa.
Pitch	Distance between adjacent lines of a grating.
Plate wave	See *lamb wave*

Porosity	Trapped pockets of air, gas or vacuum within a solid material, typically less than 10-μm in diameter.
Pot life	Time a thermosetting resin retains a viscosity low enough to be used in processing.
Prefabricated material	Composite material manufactured and cured under controlled factory conditions with a generally high material uniformity and used in cured state in the field.
Prepreg	Ready-to-mold material in sheet form impregnated with resin and stored for use. The resin is partially cured at a B-stage.
Pre-crack	Initially unbonded region used to control crack initiation in fracture testing.
Probe	See *transducer*
P-wave	See *compression wave*
Quasi-isotropic	Laminate, whose extensional stiffness properties behave like those of an isotropic material.
Radiation	Transfer of heat energy in form of electromagnetic waves.
Rayleigh wave	Surface waves that travel predominantly in media with only a single surface.
Reproducibility	Ability to obtain identical test results under repeated testing.
Rheology	The study of flow of materials, particularly plastic flow of solids.
R-Curve	Graphical representation of fracture resistance.
Saponification	Specific form of hydrolysis involving alkalis.
Sensitivity	Measure of the smallest feature inside a material that produces a discernible signal.
Shear wave	A wave in which the direction of particle motion is perpendicular to the direction of wave propagation.
Shelf life	Length of time a material can be stored under specific environmental conditions and continue to meet all applicable specification requirements.
Stoichiometry	quantitative relationship between constitutions in a chemical system.
S-wave	See *shear wave*
Thermal conductivity	Rate at which heat flows through a body.

Transducer	Device used to produce mechanical stress waves.
Transverse wave	See *shear wave*
T_g	Temperature at which increased molecular mobility results in significant changes in the properties of a cured resin system.
TVG	Time-varied-gain feature in ultrasonic test units that corrects for distance/amplitude variations due to attenuation or beam spreading.
Undercure	A condition resulting from the allowance of too little time and/or temperature for adequate hardening.
Vitrification	Process of conversion into a glassy phase.
Voids	air or gas that has been cured into a laminate or an interface between two adherents. Porosity is an aggregation of microvoids.
Volatiles	Materials, such as water or alcohol, in a resin formulation that are capable of being driven off a vapor at room temperature or at a slightly elevated temperature.
Wetability	The ability of a liquid to adhere to a surface.

REFERENCES

1. Kaiser, H. and V.M. Karbhari, *Quality and Monitoring of Structural Rehabilitation Measures - Part 1: Description of Potential Defects*. 2001, University of California, San Diego: LA Jolla, CA. p. 60.
2. Kaiser, H. and V.M. Karbhari, *Quality and Monitoring of Structural Rehabilitation Measures - Part 3.1: Selection of Potentially Critical Defects*. 2002, University of California, San Diego: La Jolla, CA. p. 31.
3. Kaiser, H. and V.M. Karbhari, *Quality and Monitoring of Structural Rehabilitation Measures - Part 2: Review and Assessment of Non-destructive Testing (NDT) Methods*. 2002, University of California, San Diego: La Jolla, CA. p. 138.
4. Chajes, M.J., et al., *Bond and Force Transfer of Composite Material Plates Bonded to Concrete.* ACI Structural Journal, 1996. **93**(2): p. 208-217.
5. Anderson, T.L., *Fracture Mechanics - Fundamentals and Applications*. 2nd ed. 1995, Boca Raton, FL: CRC Press.
6. Garden, H.N. and L.C. Hollaway, *An Experimental Study of the Influence of Plate End Anchorage of Carbon Fibre Composite Plates used to Strengthen Reinforced Concrete Beams.* Composite Structures, 1998. **42**(2): p. 175-188.
7. Kaliakin, V.N., M.J. Chajes, and T.F. Januszka, *Analysis of Concrete Beams Reinforced with Externally Bonded Woven Composite Fabrics.* Composites: Part B, 1996. **27**(3-4): p. 235-244.
8. Schuman, P.M., *Investigation on Mechanical Anchorage for Shear Rehabilitation of Continuous Reinforced Concrete T-beams with CFRP Externally Bonded Stirrups*, in *Department of Structural Engineering*. 2002, University of California, San Diego: La Jolla, CA. p. 415.
9. Lau, K.T., et al., *Mechanics of Bonds in an FRP Bonded Concrete Beam.* Composites: Part B, 2001. **32**: p. 491-502.
10. Friedrich, K., ed. *Application of Fracture Mechanics to Composite Materials*. Vol. 6. 1989, Elsevier: New York, NY. 671.
11. Yamaguchi, K., et al. *Proposal of Peeling Test Method of FRP Sheets Bonded on Concrete*. in *5th Japan International SAMPE Symposium & Exhibition*. 1997. Tokyo.
12. Xie, M. and V.M. Karbhari, *Peel Test for Characterization of Polymer Composite/Concrete Interface.* Journal of Composite Materials, 1998. **32**(21): p. 1894-1913.
13. Ye, L., et al., *Surface Treatments and Adhesion Bonding Between Concrete and a CFRP Composite.* Advanced Composite Materials, 1998. **7**(1): p. 47-61.
14. Liechti, K.M., *Fracture Testing and Failure Analysis in Adhesives and Sealants*, in *Engineered Materials Handbook*, T.J. Reinhart, H.F. Brinson, and S.J. Schneider, Editors. 1991, ASM International: Metals Park, OH. p. 335-348.
15. Giurgiutiu, V., et al., *Fracture Mechanics Testing of the Bond Between Composite Overlays and a Concrete Substrate.* Journal of Adhesion Science and Technology, 2001. **15**(11): p. 1351-1371.

16. Irwin, G.R. *Onset of Fast Crack Propagation in High Strength Steel and Aluminum Alloys*. in *Sagamore Research Conference Proceedings*. 1956.
17. Kimpara, I., et al., *Characterization of Debonding Energy Release Rate of FRP Sheets Bonded on Mortar and Concrete.* Advanced Composite Materials, 1999. **8**(2): p. 177-187.
18. ASTM D3433-93, *American Society for Testing and Materials*. 1993.
19. ASTM D5528-94a, *American Society for Testing and Materials*. 1994.
20. Yamaguchi, K., I. Kimpara, and K. Kageyama. *Evaluation of Debonding Energy Release Rate of Externally Bonded FRP Sheets for Rehabilitation of Infrastructures*. in *ICCM-12*. 1999. Paris, France.
21. Blackman, B. and A. Kinloch, *Fracture Tests on Structural Adhesive Joints*, in *Fracture Mechanics Testing Methods for Polymers Adhesives and Composites*, D.R. Moore, A. Pavan, and J.G. Williams, Editors. 2001, Elsevier Science Ltd.: Oxford, UK. p. 375.